UNIVERSITY OF CALIFORNIA

Los Angeles

Measurement of the branching ratio for eta-meson decay into a neutral pion and two photons

A dissertation submitted in partial satisfaction of the

requirements for the degree Doctor of Philosophy

in Physics

by

Jason William Brudvik

2007

The dissertation of Jason William Brudvik is approved.

Zvi Bern

David Gieseker

David Saltzberg

Bernard M. K. Nefkens, Committee Chair

University of California, Los Angeles

2007

Contents

List of Figures

List of Tables

ACKNOWLEDGMENTS

This dissertation is the result of an experiment from the Crystal Ball collaboration. I would like to thank all of the members of the many institutions for their contributions to the success of the experiment.

I am grateful to my adviser Prof. B.M.K. Nefkens for his support during my research work and the completion of this dissertation. I am especially thankful to Dr. S. Prakhov for his invaluable help with analysis and Dr. A. Starostin for his work on the experiment and with analysis. I would also like to thank Dr. R. Beck in Mainz for his support during my time in Mainz and for his guidance of the experiment.

I would like to thank the U.S. Department of Energy for the funding of the CB experiment and my research assistantship, and the National Science Foundation for travel funds, without which this research would not have been possible. I would also like to thank the STINT Fellowship Program for Academic Collaboration between Uppsala University and UCLA in pure and applied physics, for the time that I spent in Uppsala.

VITA

September 28, 1976	Born, Seattle, Washington
2000	B. S., Physics Harvey Mudd College Claremont, California
2000-2002	Teaching Assistant Department of Physics and Astronomy Los Angeles, California
2001	M. S., Physics University of California, Los Angeles Los Angeles, California
2002-2007	Research Assistant Department of Physics and Astronomy Los Angeles, California

ABSTRACT OF THE DISSERTATION

Measurement of the branching ratio

for eta-meson decay into a neutral pion and two photons

by

Jason William Brudvik

Doctor of Philosophy in Physics

University of California, Los Angeles, 2007

Professor Bernard M. K. Nefkens, Chair

This dissertation presents the results of a measurement of the branching ratio for the rare decay $\eta \to \pi^0\gamma\gamma$. The experiment was carried out in the A2 hall of the Mainz Microtron facility at the Institut für Kernphysik, on the campus of Johannes Gutenberg Universität Mainz, in Mainz, Germany. The experiment used the Glasgow-Mainz Tagger, which is a recoil-electron spectrometer, to determine the energy of the incident photons. The principal detector is the Crystal Ball, a highly segmented multiphoton spectrometer covering nearly 4π steradians surrounding the

experimental target. There is also a forward detector, TAPS, which is a multiphoton spectrometer arranged as a downstream wall of detectors. Furthermore, our setup includes an instrument used to differentiate between charged and neutral particles called the Particle Identification Detector, and a liquid hydrogen target. The kinematic-fit technique was used to select the $\eta \to \pi^0\gamma\gamma$ events. The major backgrounds, namely $\eta \to 3\pi^0$ and $\eta \to \gamma\gamma$ decay and $2\pi^0$ production were measured simultaneously. The result for the branching ratio is $\mathrm{BR}(\eta \to \pi^0\gamma\gamma) = (2.0 \pm 0.7) \times 10^{-4}$. This corresponds to a partial width of $\Gamma(\eta \to \pi^0\gamma\gamma) = 0.26 \pm 0.10$ eV. This result is somewhat smaller than the result of recent experiments, it is consistent with theoretical calculations based on Chiral Perturbation Theory.

Chapter 1

Introduction

Quantum Chromodynamics (QCD), one of the components of the Standard Model, is the accepted and very successful theory for hadron interactions of the strong force. Mathematically, QCD is a non-abelian $SU(3)_c$ gauge theory, where the c denotes color, the strong force analog of the electric charge in Quantum Electrodynamics (QED). Unlike QED which has one charge type that is either positive or negative, QCD has 3 colors and 3 anticolors. The theory contains 6 fermions and 6 antifermions, known as quarks and anti-quarks, and the interactions between them are mediated by 8 massless bosons called gluons, which form combinations of color and anticolor. Hadrons are confined color singlet combinations of quarks, antiquarks, and gluons.

An interesting aspect of QCD is asymptotic freedom. This refers to the property that at high energies, quarks behave as relatively loosely bound particles, because the QCD coupling parameter, g_s, becomes small at high energies, which allows QCD calculations to be made by a perturbative expansion. Unfortunately at low energies, g_s is large and the perturbative expansions in terms of the coupling parameter does

not converge. One approach to deal with this problem is to use an effective field theory such as Chiral Perturbation Theory (χPT).

The Lagrangian of QCD which describes quark and gluon interactions is

$$\mathcal{L}_{QCD} = -\frac{1}{4} F^{(a)}_{\mu\nu} F^{(a)\mu\nu} + i\Sigma_q \overline{\psi}^i_q \gamma^\mu \left(D_\mu\right)_{ij} \psi^j_q - \Sigma_q m_q \overline{\psi}^i_q \psi^j_q \tag{1.1}$$

where $F^{(a)}_{\mu\nu}$ denotes the gluon field tensor,

$$F^{(a)}_{\mu\nu} = \partial_\mu A^a_\nu - \partial_\nu A^a_\nu - g_s f_{abc} A^b_\mu A^c_\nu \tag{1.2}$$

D_μ is the covariant derivative,

$$\left(D_\mu\right)_{ij} = \delta_{ij}\partial_\mu - i g_s \Sigma_a \frac{\lambda^a_{i,,j}}{2} A^a_\mu. \tag{1.3}$$

f_{abc} are the structure constants of the SU(3) algebra, A^a_μ are the eight Yang-Mills gluon fields, ψ^i_q are the 4-component Dirac spinors associated with each quark field of color i and flavor q, m_q is the mass associated with each quark flavor, and λ_i are the Gell-Mann matrices.

If the masses and electric charges of the three lightest quarks, u, d, and s, were zero, the quarks would be indistinguishable and make the QCD Lagrangian invariant under SU(3) transformations of left and right handed quark fields, meaning it would be chirally symmetric. The three quark flavors have different masses, but the difference from zero is small compared to the characteristic hadronic scale of 1 GeV, which makes the SU(3) flavor symmetry an approximate symmetry that is a good approximation

for the two lightest quarks, u and d; it is known as isospin symmetry.

In χPT, the QCD Lagrangian is replaced by an effective chiral Lagrangian, which is an expansion in small momenta, p. Typically, this effective Chiral Lagrangian is written in the form

$$\mathcal{L}_{\chi PT} = \mathcal{L}_2(p^2) + \mathcal{L}_4(p^4) + \mathcal{L}_6(p^6) + \cdots \tag{1.4}$$

An exceptionally useful reaction for the study of χPT is the decay

$$\eta \rightarrow \pi^0\gamma\gamma. \tag{1.5}$$

The $\mathcal{L}_2$ term in expansion equation (1.4) is zero for this reaction, and for all neutral pseudoscalars [1]. The second term, $\mathcal{L}_4$, is much suppressed as couplings of photons to neutral mesons is a higher order phenomenon, resulting in the main contributions coming from charged pion and charged kaon loops. The charged pion loops involve G-parity-violating transitions and are therefore suppressed. The kaon loops are small due to the large mass of the kaons. The sum of the pion and kaon loops comprise the $\mathcal{L}_4$ contribution of only 3.89×10^{-3} eV to the decay width [1]. The third-order and higher terms are expected to be the main contributions to the overall decay rate. A representative theoretical value of the decay rate is 0.42 ± 0.20 eV (see Table 1.1 for other predictions). Because the first two terms are negligibly small compared to the third and higher terms, the study of the reaction $\eta \rightarrow \pi^0\gamma\gamma$ provides a unique case in which these higher order terms of the Chiral Lagrangian can be studied free from the customary dominance of the lower order terms. This thesis describes studies of

the $\eta \to \pi^0\gamma\gamma$ decay rate.

1.1 Survey of predictions and experiments

Theoretical predictions of and experimental searches for $\eta \to \pi^0\gamma\gamma$ have quite an interesting history, which has been summarized by the SND group [2]. Some of the highlights are touched upon here. The reaction $\eta \to \pi^0\gamma\gamma$ was initially proposed as an important and large decay channel of the η meson, as other mechanisms seemingly could not account for the observed decay rate by a group [3] at CERN in 1966. Subsequent experimental searches for this particular decay, starting with a group at Brookhaven [4], also in 1966, could not verify the magnitude of the decay rate as proposed by the group at CERN. As discussed in the SND paper, the experimental searches for $\eta \to \pi^0\gamma\gamma$ produced no compelling evidence of its detection until the GAMS experiment at Serpukhov in 1981 [5], which, after a reanalysis of the data two years later [6], gave a branching ratio of $(7.1 \pm 1.4) \times 10^{-4}$ based on 40 events, corresponding to a decay rate of 0.84 ± 0.19 eV.

Early theoretical predictions of the magnitude of the $\eta \to \pi^0\gamma\gamma$ decay rate started in 1963 with Okubo and Sakita's estimate that the decay rate was within an order of magnitude of 8 eV [7]. In 1967 Oppo and Oneda [8] predicted the decay rate to be between 0.3 and 0.6 eV, using Vector Meson Dominance (VMD). In 1970, Gounaris estimated the rate to be 1.0 ± 0.2 eV using chiral symmetry [9]. Table 1.1 has the modern theoretical predictions for the $\eta \to \pi^0\gamma\gamma$ decay rate. The first three entries in this table come from Ametller et al. [1], who used χPT and VMD. The contributions of the first two orders, $\mathcal{O}(\mathrm{p}^2)$ and $\mathcal{O}(\mathrm{p}^4)$, are small, as previously mentioned, due to

Theory	$\Gamma(\eta \to \pi^0\gamma\gamma)$(eV)	Reference
χPT, $\mathcal{O}(\mathrm{p}^2)$	0	Ametller, 1992 [1]
χPT, $\mathcal{O}(\mathrm{p}^4)$	0.00389	Ametller, 1992[1]
χPT, $\cdots+\mathcal{O}(\mathrm{p}^6)+\cdots$	0.42±0.20	Ametller, 1992[1]
χPT, $\cdots+\mathcal{O}(\mathrm{p}^6)+\cdots$	0.47	Ko, 1993 [10]
χPT, ENJL, χPT, $\cdots+\mathcal{O}(\mathrm{p}^6)$	0.58±0.08	Belluci, 1995 [11]
χPT, ENJL, χPT, $\cdots+\mathcal{O}(\mathrm{p}^6)$	$0.27\pm^{0.18}_{0.07}$	Bijnens, 1996 [12]
VMD	$0.30\pm^{0.16}_{0.13}$	Ng, 1992 [13]
quark-box	0.70	Ng, 1993 [14]
VMD	0.44±0.09	Jeter, 1996 [15]
χPT	0.77±0.16	Jeter, 1996 [15]
χPT, unitarized	0.47±0.10	Oset, 2002 [16]

Table 1.1: Theoretical Predictions for the $\eta \to \pi^0\gamma\gamma$ decay rate.

Group	$\Gamma(\eta \to \pi^0\gamma\gamma)$(eV)	events
GAMS-2000, 1984 [6]	0.84±0.19	40
SND (VEPP-2M), 2001 [2]	< 0.84	$7\ ^{+13}_{-7}$
CB @ AGS, 2005 [17]	0.42±0.12	1600

Table 1.2: Recent experimental results for the $\eta \to \pi^0\gamma\gamma$ decay rate.

the absence of the $\mathcal{O}(\mathrm{p}^2)$ term for neutral pseudoscalar mesons, and G-parity violation and the large kaon mass in the $\mathcal{O}(\mathrm{p}^4)$ case. The magnitude of the branching ratio is due to a combination of effects, including an "all order" VMD amplitude estimate for the $\mathcal{O}(\mathrm{p}^6)$ and higher terms, and one loop contributions to $\mathcal{O}(\mathrm{p}^8)$ which are of the same order of magnitude as the $\mathcal{O}(\mathrm{p}^4)$ terms, which are also included in the results.

The next evaluation in Table 1.1 by Ko [10] uses the same terms as [1], but also includes the contributions of C-odd axial-vector resonances to arrive at a slightly larger value. Using the Extended Nambu-Jona-Lasino model (ENJL) of χPT through the $\mathcal{O}(\mathrm{p}^6)$ terms, Belluci and Bruno [11] obtained the value 0.58 ± 0.30 eV, while Bijnens et al. [12] estimated the rate to be $0.27\pm^{0.18}_{0.07}$ eV. Ng and Peters [13] presented

a result for the decay rate of $0.30\pm^{0.16}_{0.13}$ eV using a VMD model, which is almost the same as the determination by [1] of the "all order" VMD contribution of 0.31 eV to their total rate. Using the quark-box mechanism for the $\eta \to \pi^0\gamma\gamma$ process, Ng and Peters [14] estimated the decay rate to be 0.70 eV. The first estimate in the table by Jetter [15] utilizes contributions similar to those employed by [1], to arrive at a higher result of 0.77 ± 0.16 eV, and uses a VMD model to arrive at the value of 0.44 ± 0.09 eV. Oset et al. [16] used a chiral-unitary approach to reduce some sources of error in the estimate by [1], and end up with a slightly higher, though more precise, estimate of 0.47 ± 0.10 eV.

The most recent experimental result for the $\eta \to \pi^0\gamma\gamma$ decay rate are listed in Table 1.2. The aforementioned result by the GAMS-2000 group [6] listed first in the table, was obtained using the hodoscope Cerenkov spectrometer GAMS-2000, with a 30 GeV/c π^- beam at the IHEP 70 GeV accelerator for the production of η's by the reaction

$$\pi^- p \to \eta n \tag{1.6}$$

The quoted decay rate of $BR(\eta \to \pi^0\gamma\gamma)$ =0.84 ± 0.19 suffers from low statistics and may be overestimated due to the great difficulty in taking into account the background contributions, specifically those due to the large $\eta \to 3\pi^0$ decay rate. The majority of the theoretical predictions are well below the GAMS-2000 result, and as such constitutes a rare disagreement with χPT.

The next rate given in the table is by the SND group [2]. It also suffers from low statistics; they too found that most of their background was from the $\eta \to 3\pi^0$ process. Due to the large errors, only an upper limit for the branching ratio was given.

The experiments by this group were performed with the SND calorimeter, covering 90% of 4π steradians, at the VEPP-2M e^+e^- collider, where η's were produced via

$$e^+e^- \rightarrow \phi \rightarrow \eta\gamma \tag{1.7}$$

using center-of-mass energies between 980 and 1860 MeV.

The last rate given in Table 1.2 comes from an experiment done with the Crystal Ball multiphoton spectrometer (CB) at the AGS [17], producing η's by the process (1.6). The incident momentum was 716 ± 12 MeV/c. Their result is much more in tune with the majority of current theoretical predictions, and is the only experiment used in the compilation of the $\eta \rightarrow \pi^0\gamma\gamma$ branching ratio by the Particle Data Group (PDG) [18]. They use their own fit of available results in [17] to come to a branching ratio of $(4.4 \pm 1.6) \times 10^{-4}$, which corresponds to a decay rate of 0.57 ± 0.21 eV, using the current PDG value for the full decay rate of the η meson of 1.30 ± 0.07 keV. This result removed the discrepancy between theory and experiment which had long existed, including the previous PDG value which was based on the GAMS-2000 result. A drawback of the [17] experiment was the inability to examine the spectrum of the $\eta \rightarrow \pi^0\gamma\gamma$ decay due to insufficient empty target data taken, which also had the effect of greatly increasing the statistical uncertainties in the final value.

Chapter 2

Experimental Facilities

2.1 Overview of the Experimental setup

The experiment described in this thesis took place at the Mainz Microtron facility (MAMI) in Mainz, Germany. The laboratory has an electron accelerator, which produces a beam of maximally 883 MeV. This beam is incident on a thin radiator to produce photons by the Bremsstrahlung process. The photon beam, after passing through a trimming collimator 3 mm in diameter and a halo collimator 2 cm in diameter, was incident on the 5 cm long liquid hydrogen target located in the center of the Crystal Ball multiphoton detector (CB). The electrons were magnetically analyzed, those involved in Bremsstrahlung were detected by a set of 352 small scintillator counters, they enabled one to calculate the energy of the tagged photons. The interaction products of the photons with the hydrogen target were detected by the CB, an end cap, a Particle Identification detector (PID), and Multiwire Proportional Chambers (MPC). The device immediately surrounding the hydrogen target was the PID, to

distinguish the charged from the neutral particles that were being detected by the CB as well as differentiate charged particles of different mass. Directly outside of the PID were the MPC that are intended for tracking charged particles in the future but were not used for this experiment. The MPC were located inside of the CB, which is spherical in shape and covered almost 4π steradians. The hydrogen target was located in the center of the CB. In front of the CB was the reconfiguration of the Two Arm Photon Spectrometer (TAPS) as an end cap wall of detectors, that was used to measure forward traveling photons and, with a veto wall in front of it, ostensibly to differentiate between charged and neutral particles. The information from this veto wall was not used due to its low efficiency. The solid angle acceptance of the full detector is 97%, of which 94% is provided by the CB.

2.2 Mainz Microtron facility (MAMI)

The Mainz Microtron facility (MAMI) is located in the Institut für Kernphysik, on the campus of the Johannes Gutenberg Universität Mainz, in Mainz, Germany. It is a four stage electron accelerator, consisting of a 3.5 MeV injector linac followed by 3 racetrack microtrons (RTM, see figure 2.1). The last RTM increases the electron beam energy from 180 MeV to 883 MeV in 15 MeV steps. The variations in energy of the beam are quite small, the energy is known within $\pm 0.01\%$.

Figure 2.2 shows the layout of the A2 experimental hall, in which the experiment described in this thesis took place, various components involved in the experiment will be described in the following sections. One device present but not used was the Multiwire Proportional Chambers charged particle tracker. It was not used during

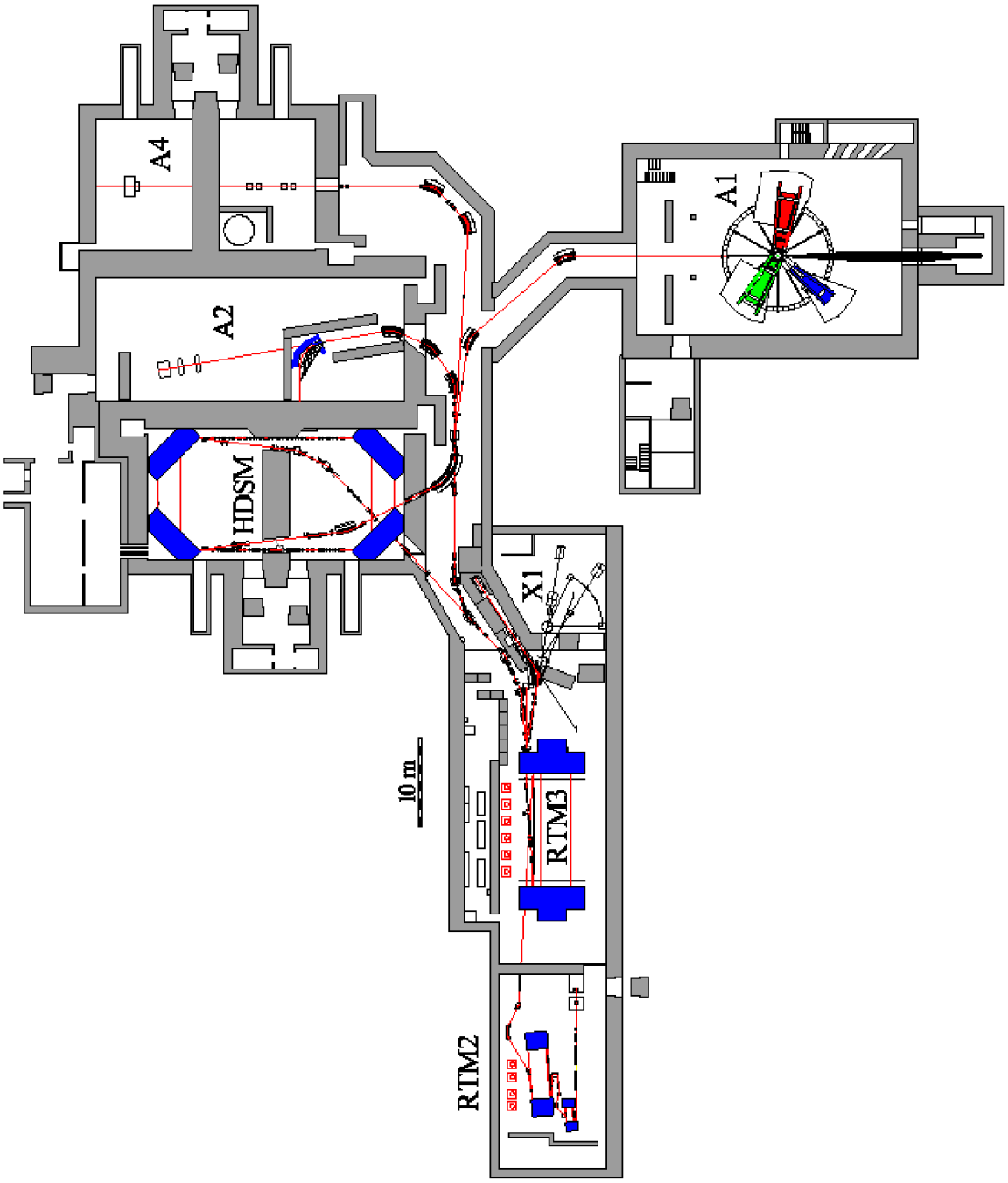

Figure 2.1: Floor plan of the MAMI facility showing the three racetrack microtrons (RTM's) and the fourth stage of the accelerator, the Harmonic Double Sided Microtron (HDSM). Also shown are the experimental halls A1, A2, A4, and X1.

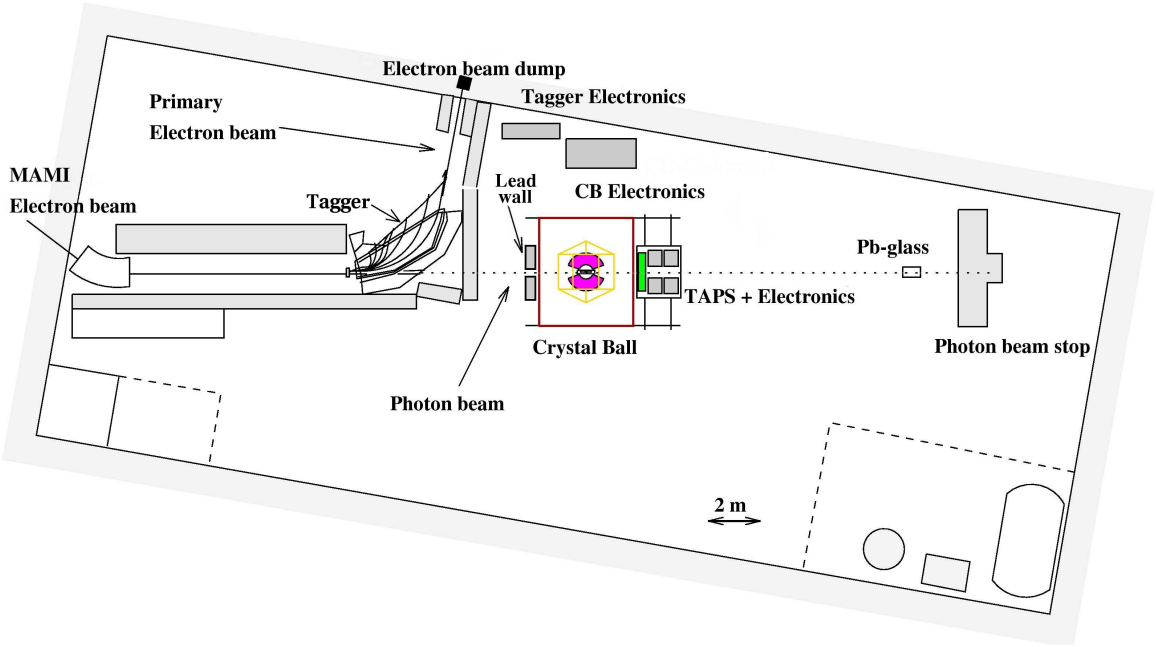

Figure 2.2: Floor plan of the A2 experimental hall.

the experiment as it could handle only a limited particle rate. Its components are given in Appendix F. Some of these components, connectors, resistors and so forth, were located in the exit tunnel of the CB, causing loss of some photons by conversion and some protons by interactions.

2.3 Glasgow-Mainz Tagger

The Tagger is an electron spectrometer built by the University of Glasgow, it was used to measure the trajectory and thereby the energy of the post-Bremsstrahlung electrons. The Tagger consists of a large bending magnet for magnetically analyzing the momentum of the electrons, and the Tagger Ladder which is a 352 scintillator

element detector located along the curved focal plane of the Tagger magnet. See Figures 2.4 and 2.20. The system tags photons in the energy range 40 to 820 MeV with a resolution of about 2 MeV. It operates at a maximal flux of approximately 10^8 electrons per second, at which point doubles in the counter become a problem. The material of the scintillator counters is NE 111/Pilot U. The thickness is 2 mm, the width varies from 8.8 mm to 32.3 mm. The widths of the scintillator elements were chosen so as to achieve slightly more than half-overlap of neighboring elements. The signals created in the detector elements were read out with 13 mm long, 9 mm diameter Hamamatsu Photonics R1635 photomultiplier tubes.

For the experiment described here, the low energy section which was not used, it was turned off so that that the energies of the tagged photons were between 680 MeV, which is a little below the η threshold of 707 MeV, and 820 MeV. The Bremsstrahlung spectrum is a continuous one with $N_\gamma \sim 1/E_\gamma$, so the high energy photons which we needed were accompanied by low energy recoil electrons, while the more numerous low energy photons were accompanied by high energy electrons. The low energy photon energy section was turned off so that the electron beam intensity could be increased and still keep the doubles limited.

After the electrons entered the experimental hall, from the left in figure 2.2, they passed through the 5μm thick, aligned diamond radiator, used for the production of linearly polarized photons in other experiments. The thickness of this radiator corresponds to 4×10^{-5} radiation-lengths. The 883 MeV electron beam produced a spot size on the radiator of less than 1 mm in diameter, and for most purposes may be regarded as a point source. Figure 2.3 shows the distribution of Tagger ladder

element hits, which are converted to electron energy, and photon energy. Since the initial electron energy, E_0, is known well, and the radiator has a relatively high mass so that its very small recoil momentum during the Bremsstrahlung process can be ignored, the resulting photon energy, E_γ, is easily found once the post Bremsstrahlung electron's energy, E_{e^-}, has been determined:

$$E_\gamma = E_0 - E_{e^-} \tag{2.1}$$

The photons continued through a 3 mm diameter collimator, located 2.5 m after the radiator. After another 4.5 m, the beam passed through a 2 cm diameter collimator to cut down on the halo. The photons then passed through a hole in a lead wall placed just upstream from the CB. This wall fit around beam pipe, it was used to block spurious electrons and neutrons produced by the beam in the Tagger and beam stop. The photons reached the target, which was 10 m from the radiator. The rate of electrons entering the hall for this experiment was typically 35 nA, which corresponded to a rate of photons being sent to the target of about 10^8 s^{-1}. Electrons whose energy was outside the detector range were directed to the beam dump. The resulting photon beam spot size at the target was 12 mm, well within the 4.0 cm target diameter.

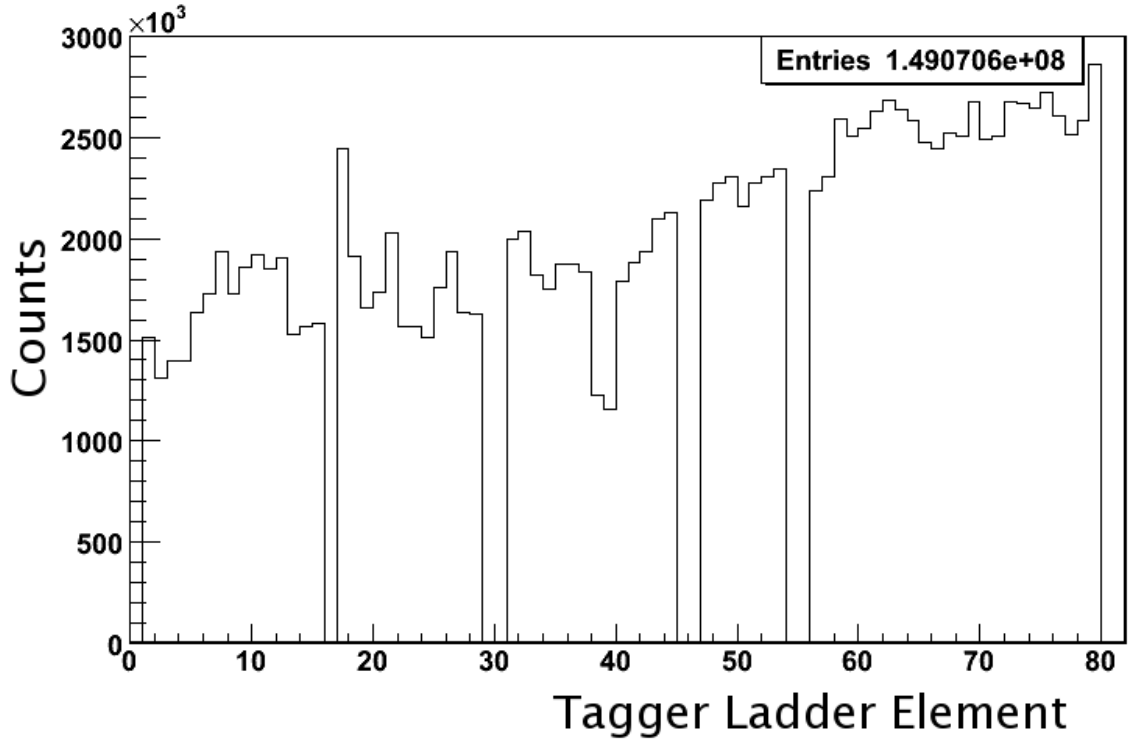

Figure 2.3: The distribution of counts in Tagger elements active in the experiment. The Bremsstrahlung cross section has a $1/E_\gamma$ dependence on the photon energy, E_γ. This manifests itself as a $1/E_\gamma$ dependence of the recoil electron spectrum. The lower energy photons correspond to the higher numbered ladder elements. Gaps in the distribution are due to non-functioning channels. The deep dips are due to deteriorated scintillation counters, which were over 15 years old, they will be replaced prior to the next round of experiments in 2007.

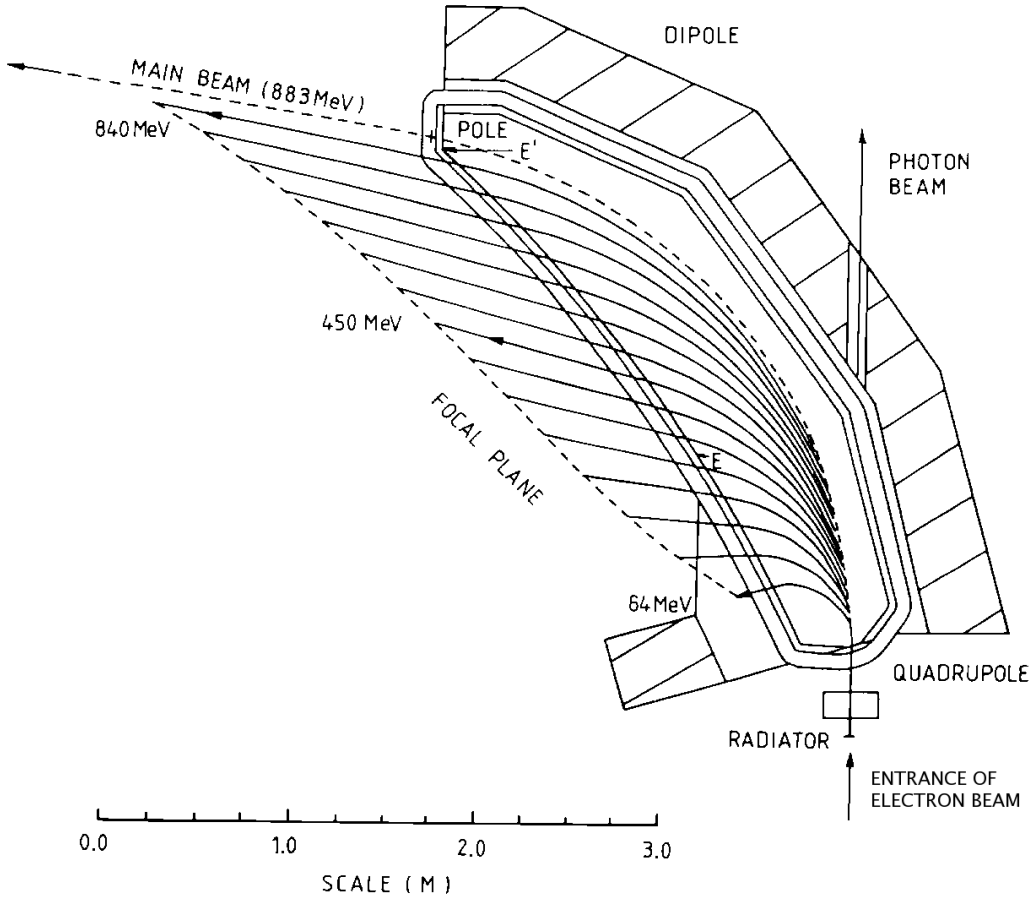

Figure 2.4: The electron beam passes through the radiator where photons are created by the Bremsstrahlung process. The photons go straight to the hydrogen target, while the electrons are bent by the Tagger dipole magnet. Those electrons which do not lose energy while passing through the radiator end up in the beam dump located behind the Tagger magnet. The dipole magnet is of the "C" type. It is approximately 370 cm long. The weight is near 65 metric tons. The gap between the two faces of the dipole was 50 mm, the strength of the magnetic field used was 1.049 T.

The Tagger detector elements were operated with a limit around 5×10^5 MeV/s in order to limit the long term wear on the PMT's and radiation damage to the scintillators. Unused sections of the Tagger were turned off because the PMT's attached

to these elements could not handle a high rate of recoil electrons. Also, by turning off the sections of the Tagger that yielded $E_\gamma < 680$ MeV, the volume of unnecessary data could be reduced.

The energy calibration of the Tagger counter was performed by Richard Codling [21], using electron beams of precisely known energies, directed at the counters with no radiator present, so that the electron energies were associated with the scintillators of the Tagger.

During the running of this experiment, the so called "tagging efficiency" was measured using the Pb-glass detector depicted in Figure 2.2 behind TAPS. This detector is based on the Cerenkov light generated by the secondary electron beam, produced by the photon interactions in the Pb-glass. This is a measurement of the efficiency of the photon transmission through the experimental setup. The transmission was mainly limited by the photon collimator, not the inefficiencies of the tagging counters as the name incorrectly implies. The measurement of the tagging efficiency is important as it is a sizable factor in measurements of reaction cross sections. It is not of direct concern for the experiment of this thesis.

The 883 MeV electron beam had horizontal and vertical emittances of $1.3 \times 10^{-5} \pi \cdot m \cdot rad$ and $8.4 \times 10^{-7} \pi \cdot m \cdot rad$, respectively. The emittance is a measure of the beam quality in a two dimensional phase space defined by the spatial and momentum coordinates, which for this experiment is quite low, meaning a very high quality beam and that for most purposes may be regarded as a point source. Nearly half of the Bremsstrahlung photons are emitted in a narrow cone defined by the characteristic

half-angle

$$\theta_c \approx \frac{m_e}{E_e} \tag{2.2}$$

It is about 0.6 mrad for the beam used, approximately the same size as the 0.6 mrad angle defined by the collimator radius and its distance from the radiator.

At the location of the Pb-glass detector, 15 m from the radiator, the spot size was 18 mm, which was much smaller than the detector's $20 \times 20 \times 20$ cm size.

The efficiency was measured for each channel, defined as

$$\varepsilon(i) = \frac{N_{coin}(i)}{N_e(i)} \tag{2.3}$$

where $N_{coin}(i)$ is the number of coincidences between the Pb-glass detector and the i^{th} detector element, and $N_e(i)$ is the number of electrons recorded by the i^{th} element [19]. Figure 2.5 shows the results of a typical tagging efficiency measurement taken during this experimental period, where the efficiency was between 34 and 39%. Tagging efficiency measurements were taken once or twice daily as well as after adjustments of the electron beam, as a change in the alignment between the electron beam and the collimator axis would effect the tagging efficiency. During normal running of the beam, the image of the beam could be viewed with a scintillator/CCD camera located beyond the experimental detectors, the distortion or drift in the beam indicates the need for an adjustment of the electron beam direction. The beam intensity was greatly reduced during tagging efficiency measurements, as the photomultiplier units of the Pb-glass detector were limited to less than 10^5 s^{-1}, while typical experimental conditions had intensities of $\sim 10^8$ s^{-1}.

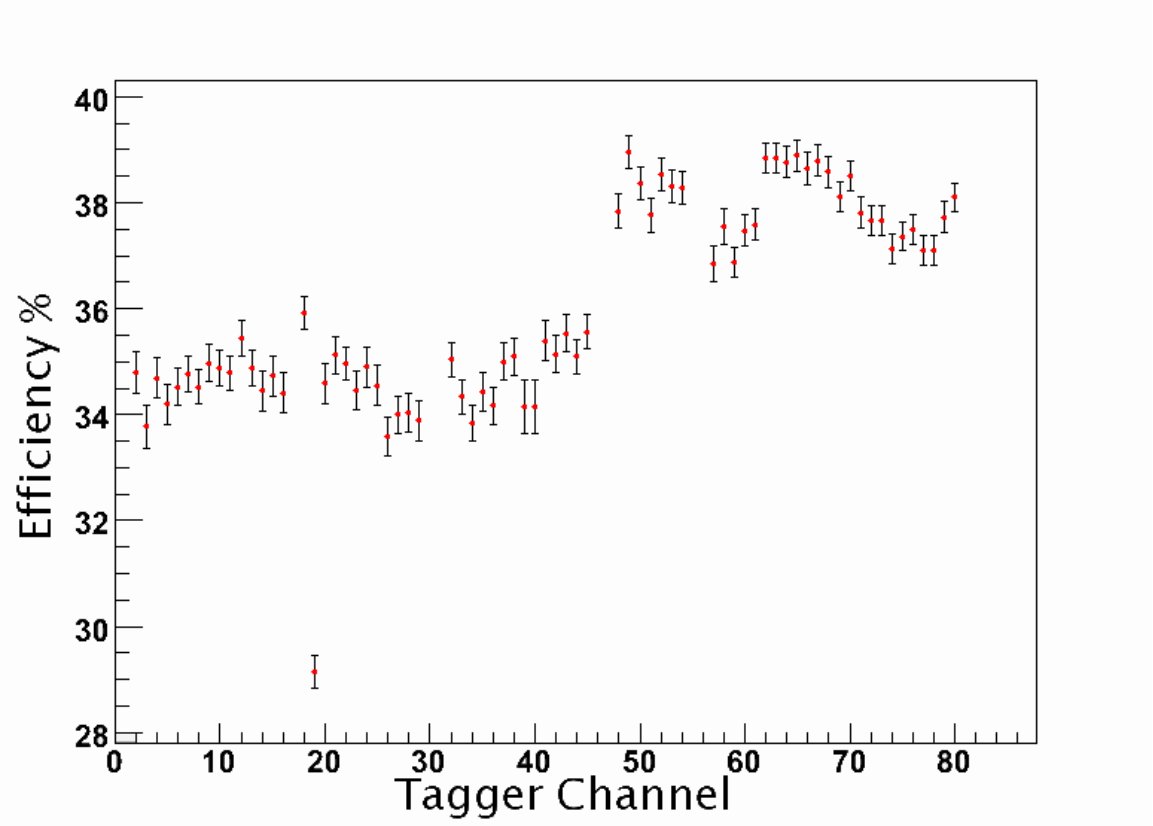

Figure 2.5: A typical tagging efficiency measurement taken during the experiment. The gaps present are due to dead channels. Channel to channel variations are due to the slight mismatch of the Tagger counters.

2.4 Crystal Ball multiphoton spectrometer (CB)

The Crystal Ball (CB) is a highly segmented, total energy, electromagnetic calorimeter and spectrometer that covers 93% of 4π steradians. The construction of the CB was started in 1975 by a group of physicists from Caltech, Harvard, Stanford, SLAC[1], and Princeton, completed in 1978. It was used at SPEAR[2] from 1978 to 1981, where some of the main investigations concerned J/Ψ spectroscopy, radiative Ψ decays, τ decays, and D decays. Then it went for five years to DORIS[3] at DESY[4] where, among other things, it was used for Υ spectroscopy, especially decays. The CB was then placed in storage in a controlled dry environment at SLAC from 1987 until it was moved to the AGS[5] facility at BNL[6] in 1995. While at BNL, the CB was successfully used for nucleon and hyperon spectroscopy. The experiments provided information on K^- and π^- induced reactions, as well as several upper limits on rare η decays. The CB was then moved to MAMI in 2002.

[1]SLAC: Stanford Linear Accelerator Center.
[2]SPEAR: Stanford Positron Electron Accelerating Ring.
[3]DORIS: Double Ring Storage, electron-positron storage ring.
[4]DESY: Deutsches Elektronen Synchrotron.
[5]AGS: Alternating Gradient Synchrotron.
[6]BNL: Brookhaven National Laboratory.

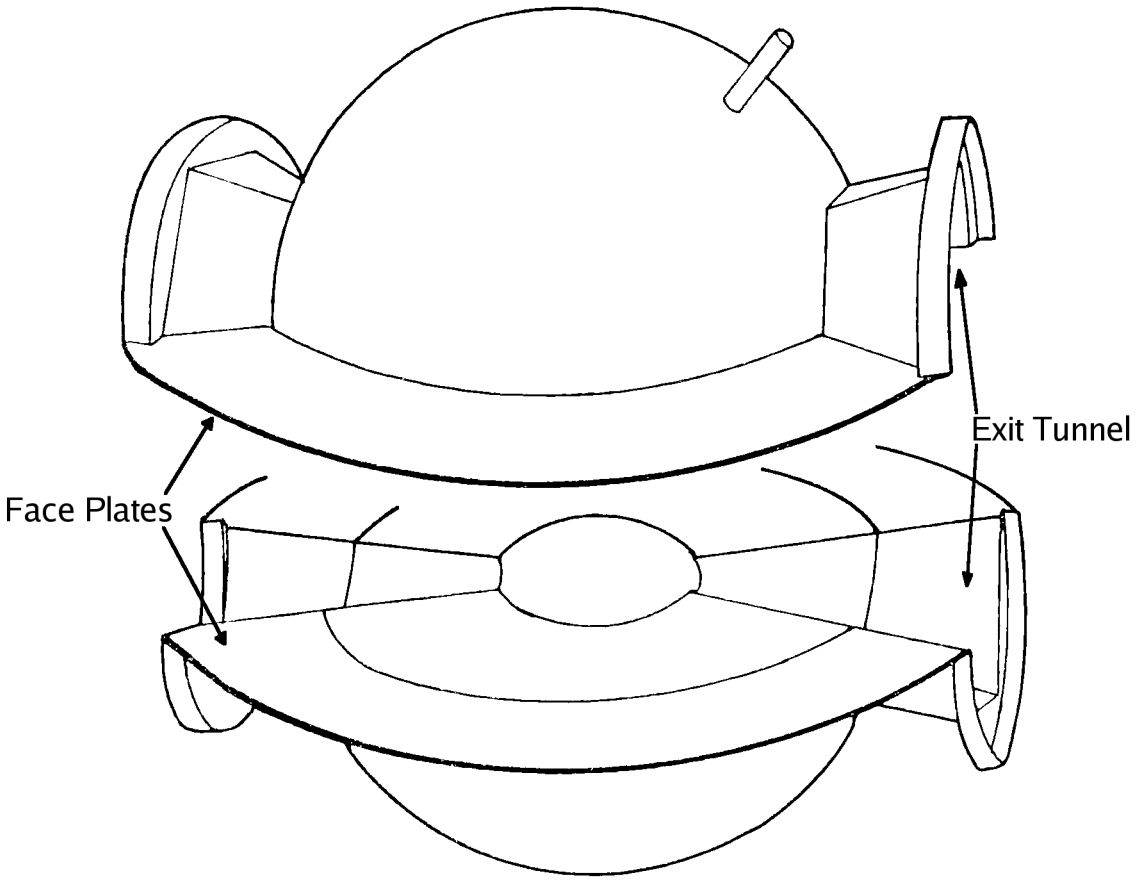

Figure 2.6: The two stainless steel hemispheric containers which hold the NaI crystals, that comprises the CB.

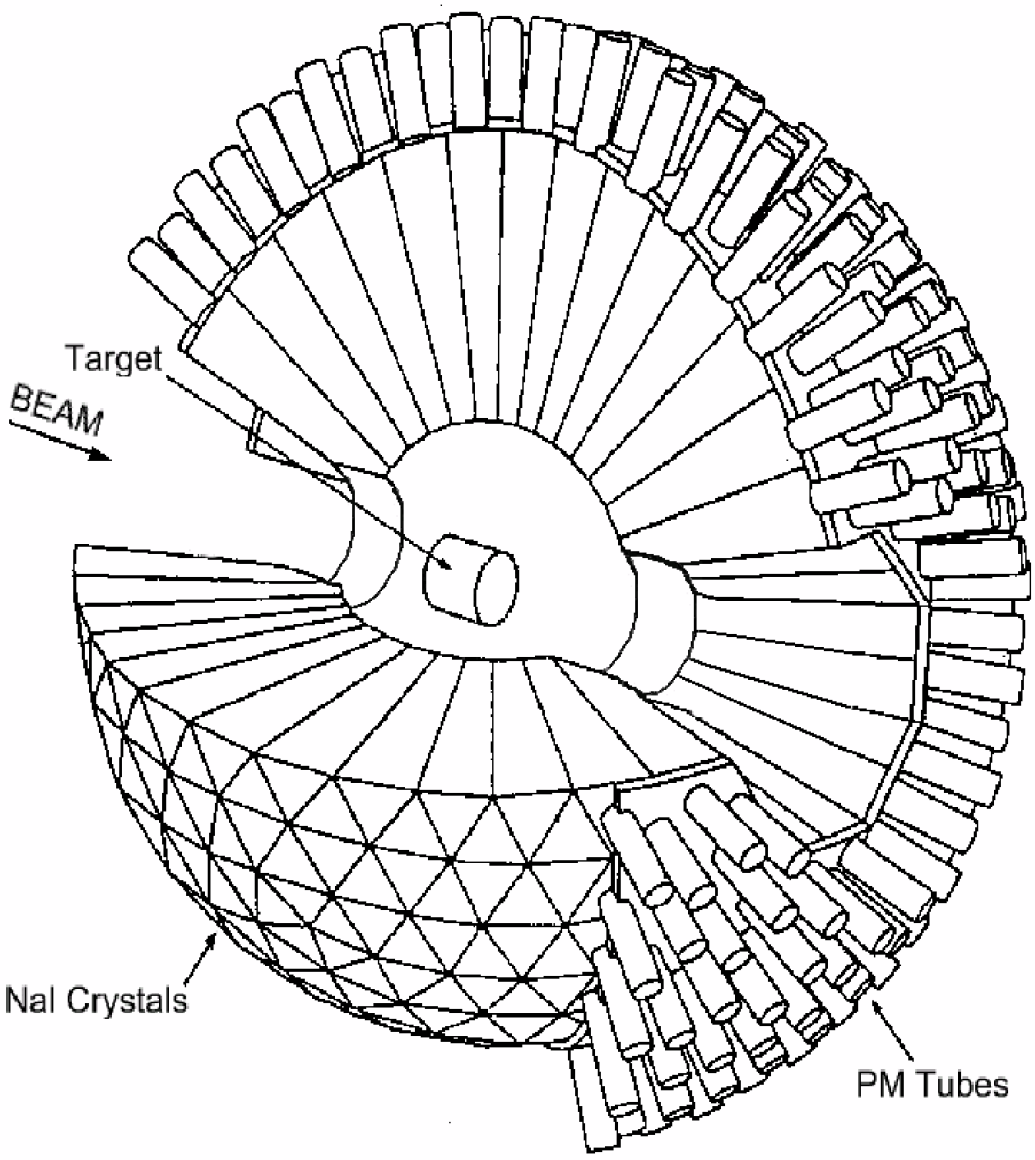

Figure 2.7: Cut-away view of the Crystal Ball Detector

The CB consists of 672 NaI(Tl) crystals that are optically isolated from one another, as they are wrapped in reflecting paper and aluminized mylar. Each crystal is shaped like a truncated pyramid, 40.6 cm in length, with one end having sides of

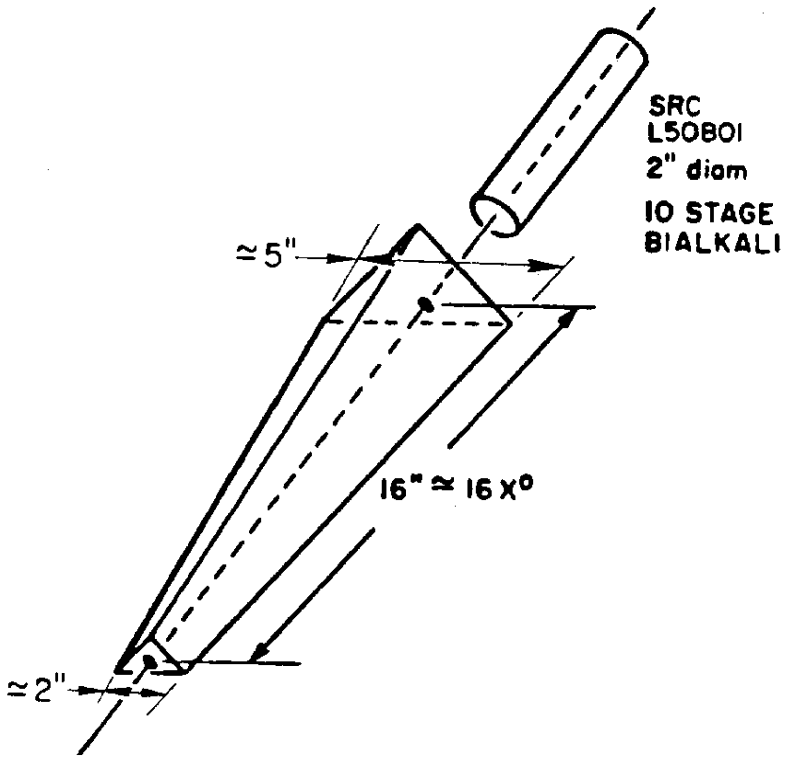

Figure 2.8: A CB crystal.

about 5.1 cm, the other having sides of about 12.7 cm (see figure 2.8). The crystals are aligned such that they point radially outward from the center of the CB, with the wider end of the crystals being along the outside of the ball. The light produced in the NaI(Tl) passes through 1.25 cm of evacuated space and 2.5 cm of plastic, it is detected by a 5.1 cm diameter, 21 cm long photomultiplier tube (PMT) type SRC L50B01; they were selected for their linearity over a wide range.

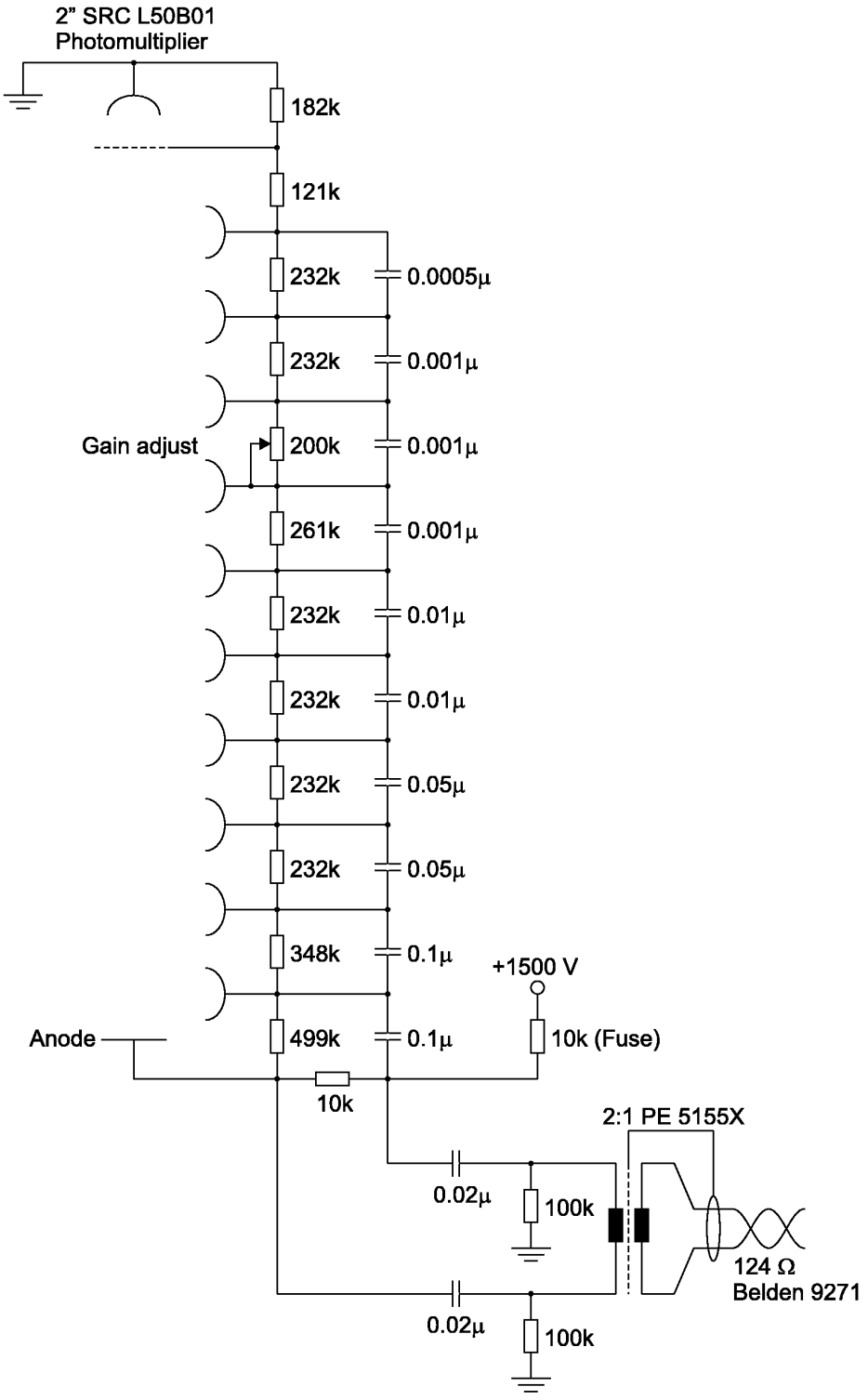

Figure 2.9: The circuit basis for the CB photomultiplier SRC L50B01.

The overall geometry of the CB is that of an icosahedron, which has 20 triangular faces that we refer to as "major triangles." Each of these 20 faces are divided into 4 "minor triangles," which each consists of 9 crystals. In such an arrangement, there would nominally be 720 crystals. Because of the entry and exit tunnels for the beam, 48 crystals are absent, thus the CB has a total of 672 crystals. The crystals are situated in this arrangement such that there is a spherical cavity in the center of the CB with a radius of 25.3 cm. The radius of the outer shell is 66.0 cm. The PMTs with base and connectors are about 26 cm long, making the total CB radius 92 cm.

The CB is divided into an upper and a lower hemisphere, each weighing around 3 tons. The hemispheres are separated by approximately 0.8 cm, due to 2x1.6 mm of stainless steel face plate and 4.8 mm of air. This inactive space between the hemispheres amounts to 1.6% of 4π steradians. Along the inner spherical cavity, each hemisphere has a shell of 1.5 mm thick stainless steel. The hemispheres are hermetically sealed in order to protect the crystals, and the temperature and humidity are controlled, the temperature being 23$\pm$2 °C and the humidity being low, usually around 30%.

The photon-energy measurement with the CB was quite precise, as approximately 98% of the energy deposited from a photon is contained in the counters. For electromagnetic showers, the energy resolution is $\sigma_E/E = 2.05\%/E(\mathrm{GeV})^{0.36}$. Also, due to the high degree of segmentation in the CB, position resolution is quite good, with the resolution in θ, the polar angle with respect to the beam axis, being σ_θ= 2 - 3° for energies in the range of 50 to 500 MeV, and for the azimuthal angle ϕ, the resolution is σ_ϕ= (2 - 3°)/sin θ, in the same energy range. The thickness of the crystals corre-

sponds to about one quarter of a hadronic interaction length. The length of a crystal corresponds to a stopping range of 233 MeV for $\mu^{\pm}$, 240 MeV for $\pi^{\pm}$, 341 MeV for $K^{\pm}$, and 425 MeV for protons. The neutron detection efficiency ranges from 10% for 50 MeV neutrons to 40% for 250 MeV neutrons.

The energy calibration of the CB is described in Appendix B of this thesis.

Azimuthal angular acceptance	$0^\circ \leq \phi \leq 360^\circ$
Polar angular acceptance	$20^\circ \leq \theta \leq 160^\circ$
Polar angular resolution	σ_ϕ= 2 - 3°
Azimuthal angular resolution	σ_ϕ= (2 - 3°)/sin θ
NaI(Tl)-crystal depth	15.7 RL
Energy resolution	$\sigma_E/E = 2.05\%/E(\mathrm{GeV})^{0.36}$
Time resolution	1 ns FWHM, after rise time compensation

Table 2.1: Some general CB properties

2.5 TAPS (Two Arm Photon Spectrometer)

The end cap of the CB consists of the reconfigured TAPS detector, made up of 510 BaF_2 detectors, designed to measure hard photons from neutral mesons. TAPS stands for "Two Arm Photon Spectrometer." The acronym dates from the early days of the detector. For this particular experiment, TAPS was set up as a forward wall, 180 cm from the exit of the CB (see figure 2.12). The energy resolution of TAPS for photons is $\sigma_E/E = 0.79\%/\sqrt{E_\gamma} + 1.8\%$. The neutron detection efficiency is approximately 25% for energies of 100 MeV.

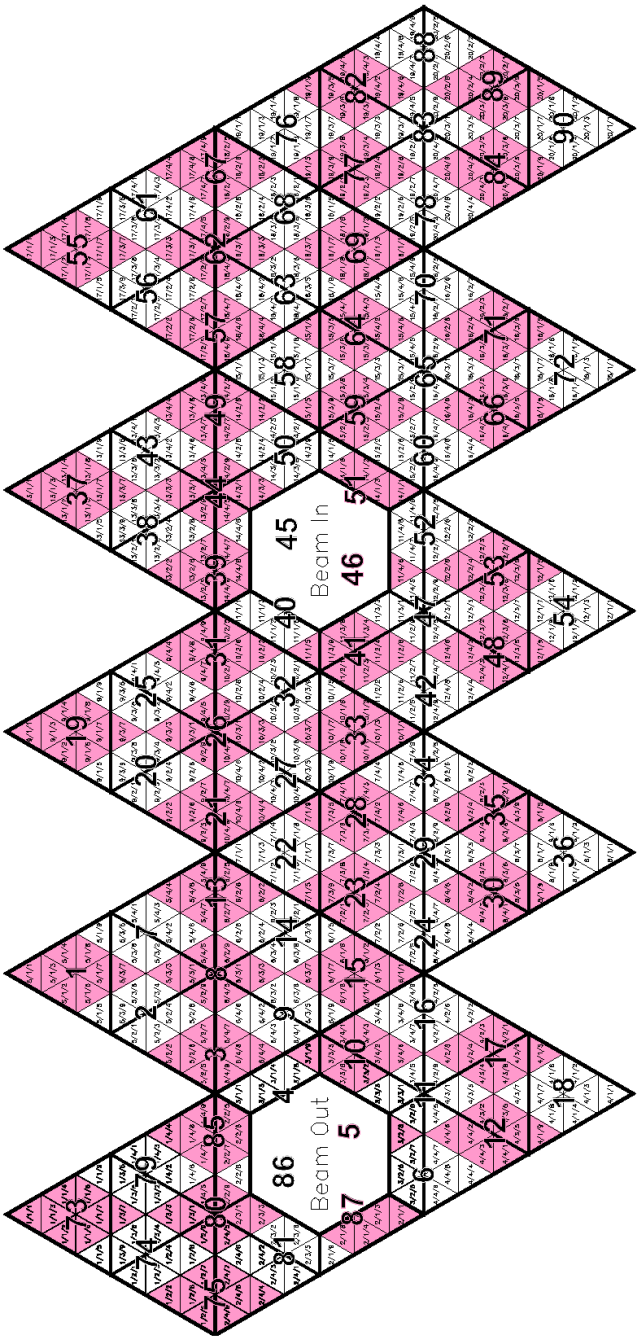

Figure 2.10: Two dimensional Mercator-like projection of the CB crystals. A combination of 16 channels (an adjacent shaded and unshaded group in the figure, such as groups 1 and 2) formed a block, used in the experimental trigger, discussed in section 2.8.3.

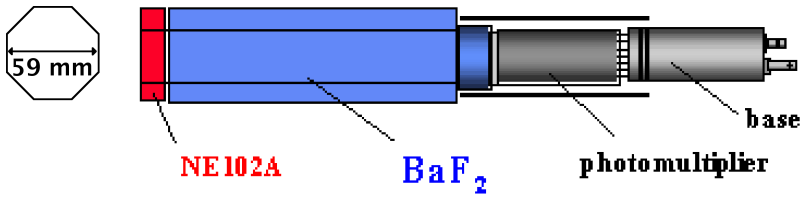

Figure 2.11: A standard TAPS element.

Each of the BaF_2 detectors is a block 250 mm long with hexagonal front and back shapes, with an inner diameter of 59 mm (see figure 2.11). They are wrapped in PTFE[7] and a thin aluminum foil is used as a UV-reflector. Each crystal is optically coupled to the quartz window of a Hamamatsu R2059-01 photomultiplier tube. The length of each crystal corresponds to a stopping range of 180 MeV for $\pi^{\pm}$, 280 MeV for $K^{\pm}$, and 360 MeV for protons. Plastic scintillator (EJ-204) veto counters 5 mm thick hexagonally shaped to match each TAPS counter were located in front of TAPS and were intended to differentiate between charged and neutral particles, as previously mentioned. Due to inefficiencies in the veto elements, their output was not used in the analysis. The calibration of TAPS was performed by Benedicte Boillat [20], using the known energy deposition of minimal ionizing cosmic ray muons to determine the gain factor for each crystal.

TAPS covers an angular range of 2 - 20°, thus catching the particles that leave through the exit tunnel of the CB, increasing the detection of particles to 97%. For this experiment the angular range of TAPS was approximately 4 - 20° due to limitations on the particle flux in the crystals close to the beam line, the counters in the smallest two rings were turned off to save the cathodes of the photomultipliers.

[7]PTFE: Polytetraflourethylene

Distance from CB	180 cm
Angular acceptance	$2^\circ \leq \theta \leq 20^\circ$
Angular resolution of 300 MeV photons	0.7° FWHM
BaF_2-crystal depth	12.3 RL
Energy resolution	$\sigma_E/E_\gamma = 0.79\%/\sqrt{E_\gamma} + 1.8\%$
Time resolution	0.5 ns FWHM

Table 2.2: Some general TAPS properties

2.6 Particle Identification Detector (PID)

The Particle Identification Detector (PID) is used to distinguish between neutral and charged particles as well as between different charged particles. It is located inside the CB (see figure 2.13). The PID was constructed at Glasgow University. It consists of 24 plastic scintillators, cylindrically arranged, with an inner diameter of 100 mm. The size of each scintillator is 315x13x2 mm. They are made of EJ204 plastic and are connected to a 10 mm Hamamatsu R1635 PMT, affixed to the end of the scintillators, at the downstream end of the CB exit.

The PID provides a ΔE and a rough value for ϕ of charged particles. Using the ΔE and the energy deposit in the CB, protons can be distinguished from $\pi^{\pm}$mesons. The time resolution of the PID is 1 ns. The calibration of the PID was performed by Richard Codling [21] using particles detected in both the CB and PID, which deposited energies in the CB within the narrow range of 32 to 48 MeV. In doing the calibration, $\gamma p \rightarrow \pi^0 p$ and $\gamma p \rightarrow \pi^+ n$ reactions were selected for. The gains were

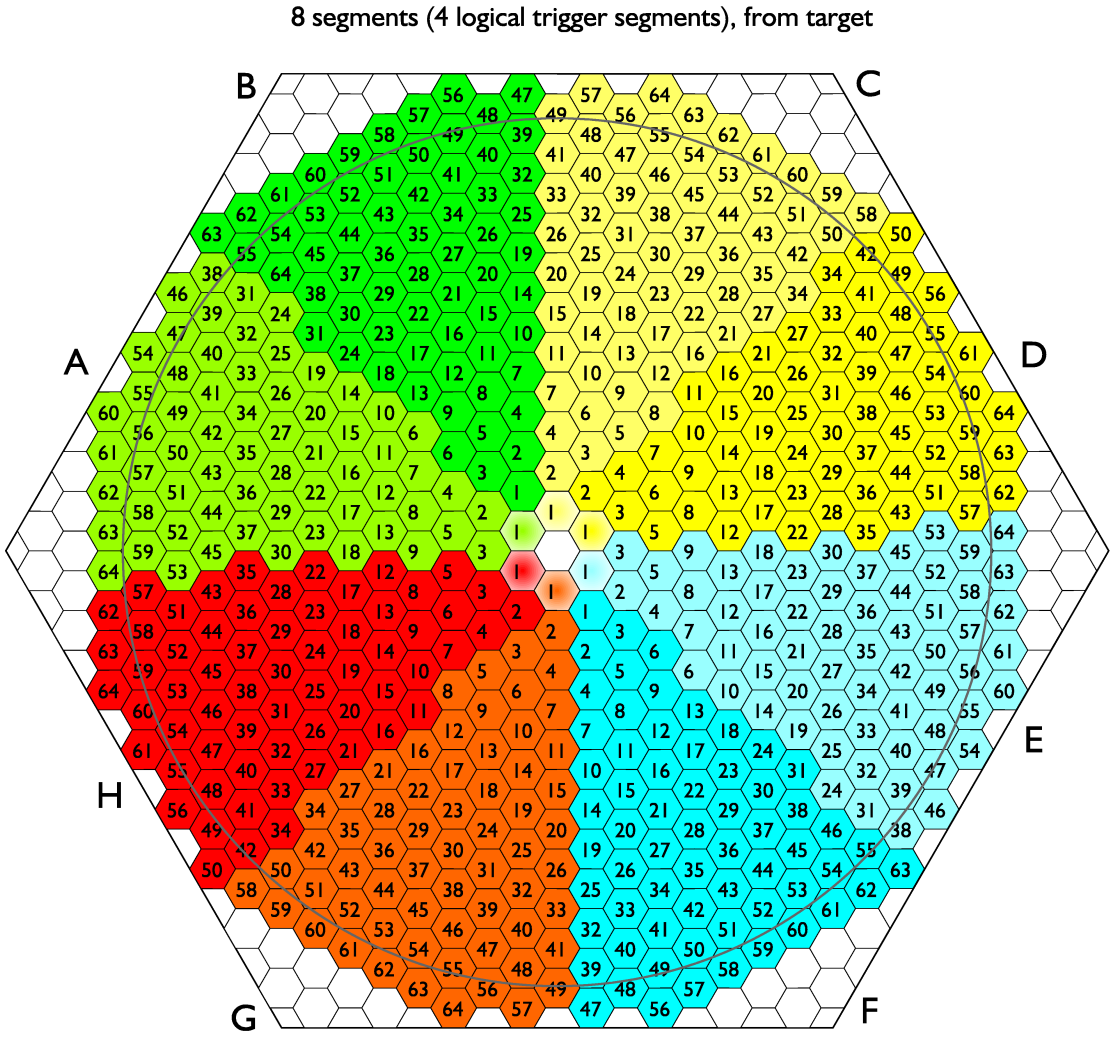

Figure 2.12: TAPS wall. The numbers in the figure are the labels given to each crystal.

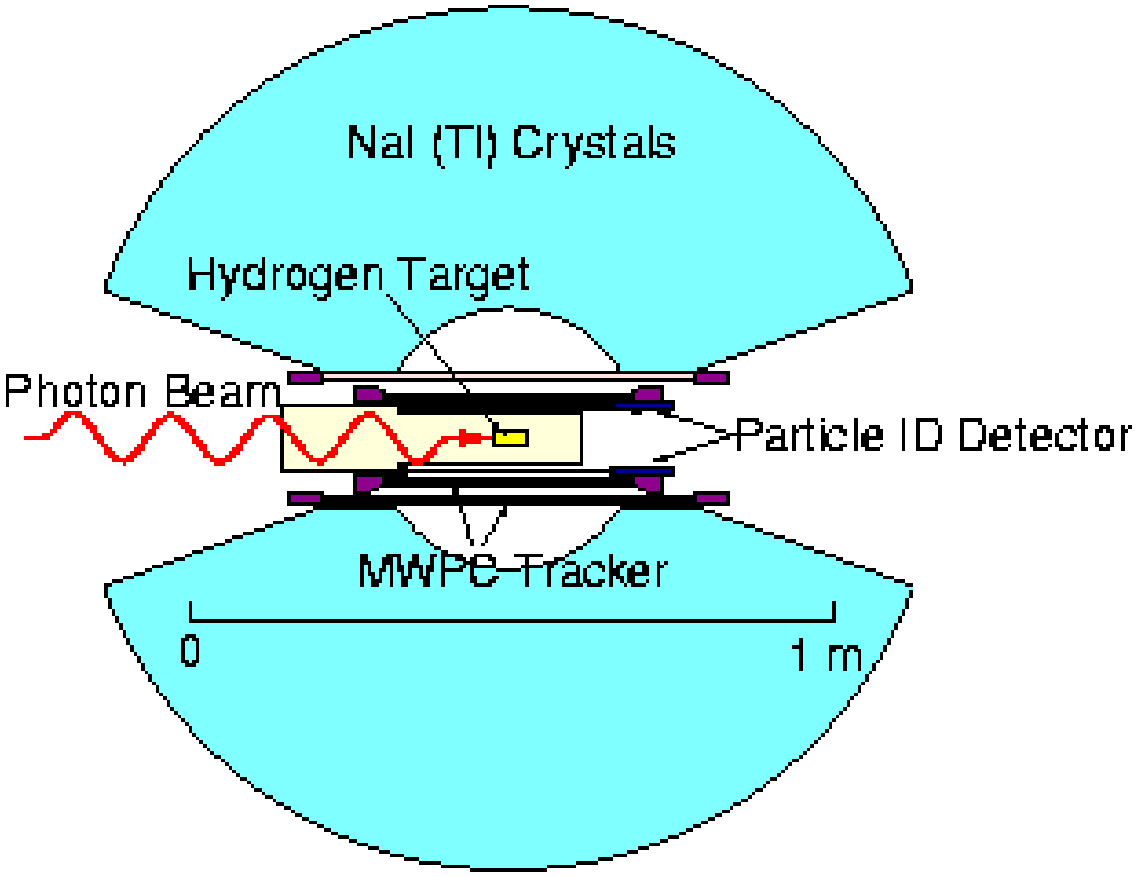

Figure 2.13: CB with the MPC and PID surrounding the hydrogen target.

adjusted so that the difference in the energies deposited in the PID by protons and pions was the same for all 24 elements. Figure 2.14 shows an example of a ΔE /E plot with the regions of protons and pions designated. Early in the experiment described here, while working on the H_2 target two of the 24 elements of the PID were damaged such that they were practically unusable.

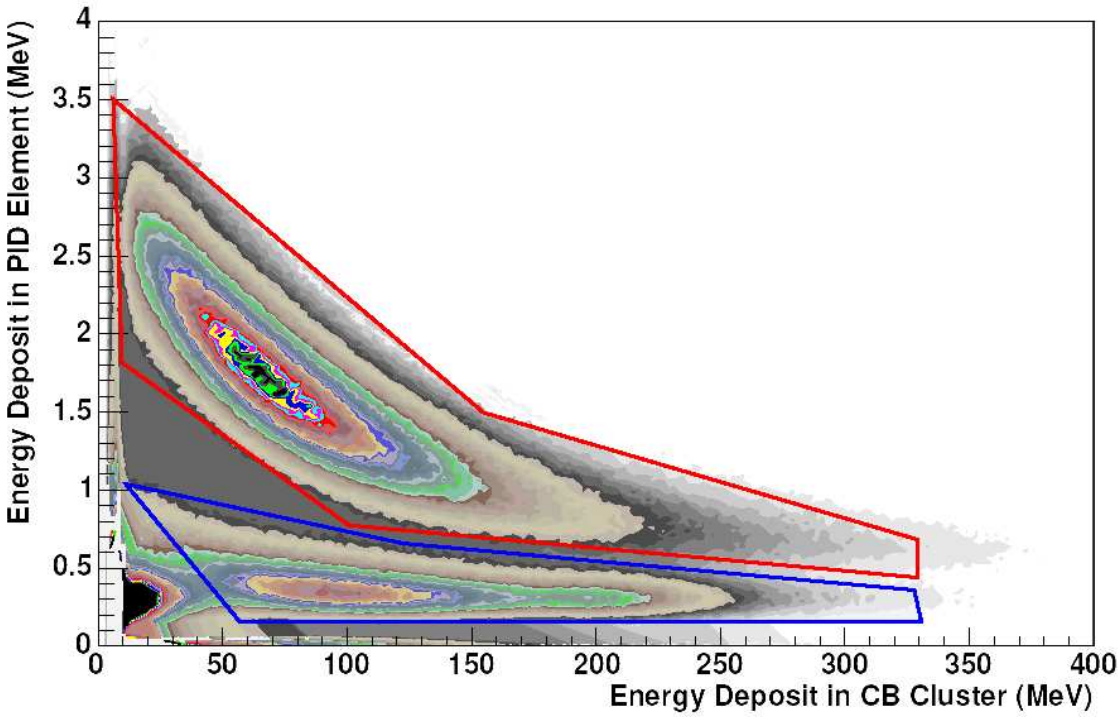

Figure 2.14: ΔE /E plot for all PID elements showing the proton cut (upper section) and pion cut (lower section).

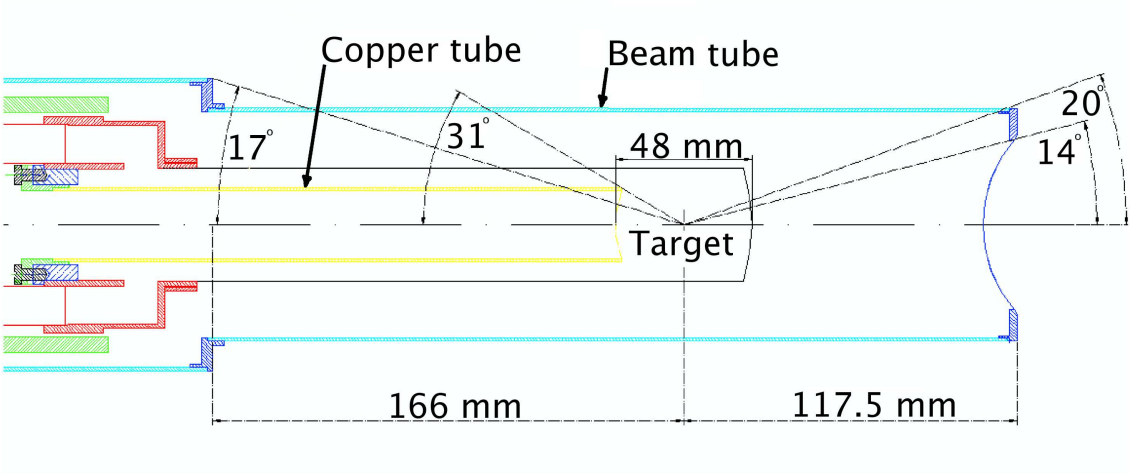

Figure 2.15: Diagram of the Hydrogen-target cell. The target cell is located in the center of the CB. It is 48 mm long, with a diameter of 40 mm. The cell is situated in the beam pipe, a CFK tube with a wall thickness of 1 mm.

2.7 Hydrogen target

The target for this experiment was liquid H_2 which was kept in a cylindrically shaped kapton cell. When cold, the target cell had a length of 4.8 cm, a diameter of 4.0 cm, and a volume of 265 cm^3, which corresponds to a total number of protons in the target of 2.0×10^{23}. A tank with a volume of 1.0 m^3 was used to store the hydrogen for filling the target system. The target cell and supply lines connected to it were located inside the photon beam pipe, which is a carbon fiber vacuum tube type CFK, evacuated to 3×10^{-7} mbar, installed in the CB cavity. The diagram of the target system can be seen in Figure 2.15, and a close up view of the target cell area is given in Figure 2.16.

During operation, about 25% of the hydrogen in the reservoir was liquefied, and

the pressure in the storage tank dropped to 1080 mbar from a typical initial value of 1390 mbar. The H_2 in the target during operation was at a temperature of 21 K.

The material surrounding the target included 125 μm kapton, 8 layers of super insulation foil (8 μm mylar, 2 μm aluminum) used to prevent moisture build up on the target window. Outside these layers was 1 mm of the CFK vacuum tube.

During our experimental runs in September of 2004, it was found that ice formed on the exit window of the vacuum tube, approximately 10 cm downstream from the target cell. We found that spurious events were generated in increasing number over time at the location of the exit window, implying that ice was growing on the window. The location of the vertex was determined by using the MPC. Visual inspection of the window confirmed the existence of ice. Figure 2.17 shows the z-vertex of events of an empty target run. The two peaks on the left are the windows of the target cell, 48 mm apart, and the far right peak is the exit window.

By measuring the yield of π^0's produced over time at the exit window, the amount of ice could be monitored [22], as shown in Figure 2.18. The first attempt to combat the ice problem in late September of 2004 was to place additional 125 μm of polyethylene naphthalat (PEN) foil around the target cell in order to avoid water permeation. This was found to reduce the rate of ice growth from 2.3 μm per hour to 1.2 μm per hour. The next addition was 20 μm of kapton, which served as a "warm jacket" around the the additional foil already in place, which was implemented in mid October of 2004. This was found to greatly reduce the amount of ice, down to 0.1 μm per hour. The experimental runs used for the work described in this thesis took place during November and December of 2004, at which time the rate of ice growth was

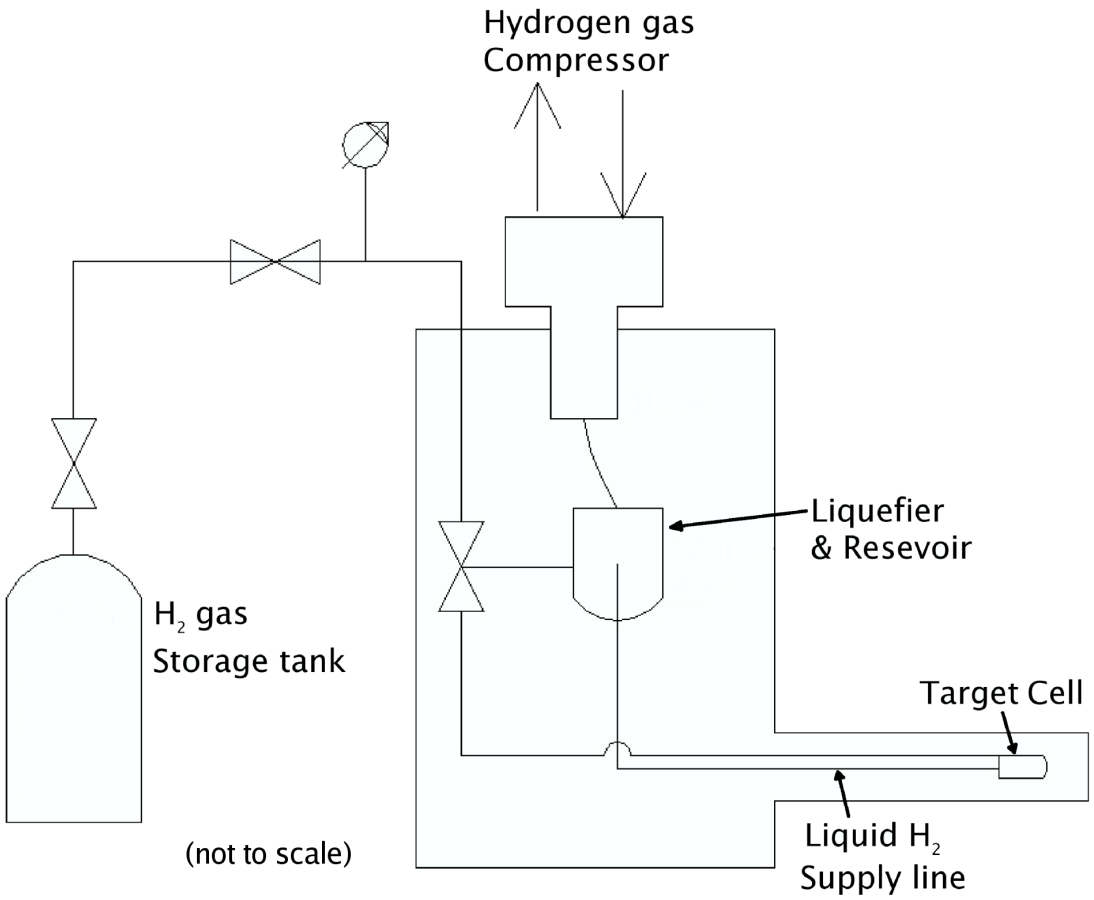

Figure 2.16: Schematic of the complete liquid H_2 target system, which is composed of a 1000 liter gas storage tank, a hydrogen gas compressor, a liquefier within which was located a reservoir for the liquid H_2, the liquid H_2 supply line connecting the reservoir in the liquefier to the target cell which was located in the center of the CB.

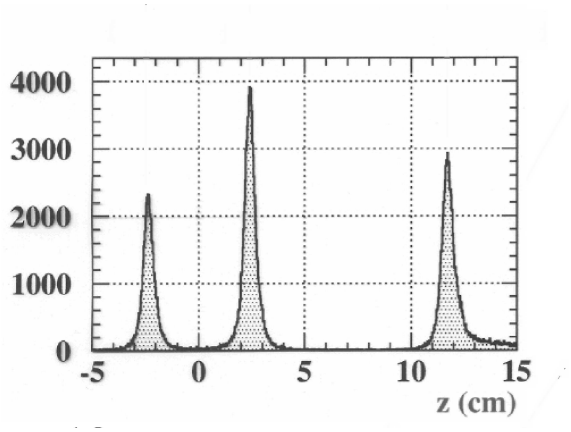

Figure 2.17: Event origin in an empty target. The two peaks on the left are the windows of the target cell, on the right is the exit window of the vacuum tube. This picture was made using the MPC to track the proton of the $\gamma p \rightarrow \pi^0 p$ reaction.

approximately 0.1 μm per hour. The rate of ice growth was not actually measured during this time as the MPC were turned off, but the state of the target was the same as in January of 2005, when the rate was measured.

2.8 Electronics

2.8.1 Overview of Electronics

Figure 2.19 displays the overall data acquisition (DAQ) electronics and how the different electronic modules fit in. Included in the overall data acquisition are the signals from CB, TAPS, Tagger, PID, and MPC, the data were read out by 2 PPC CPUs in 9U VME crates, 3 passive 6U VME crates for the SADCs, 3 fastbus crates for the Tagger, and 2 CAMAC crates for the programmable event trigger system.

The different electronics for each apparatus will be discussed here, along with the high voltage systems and event trigger.

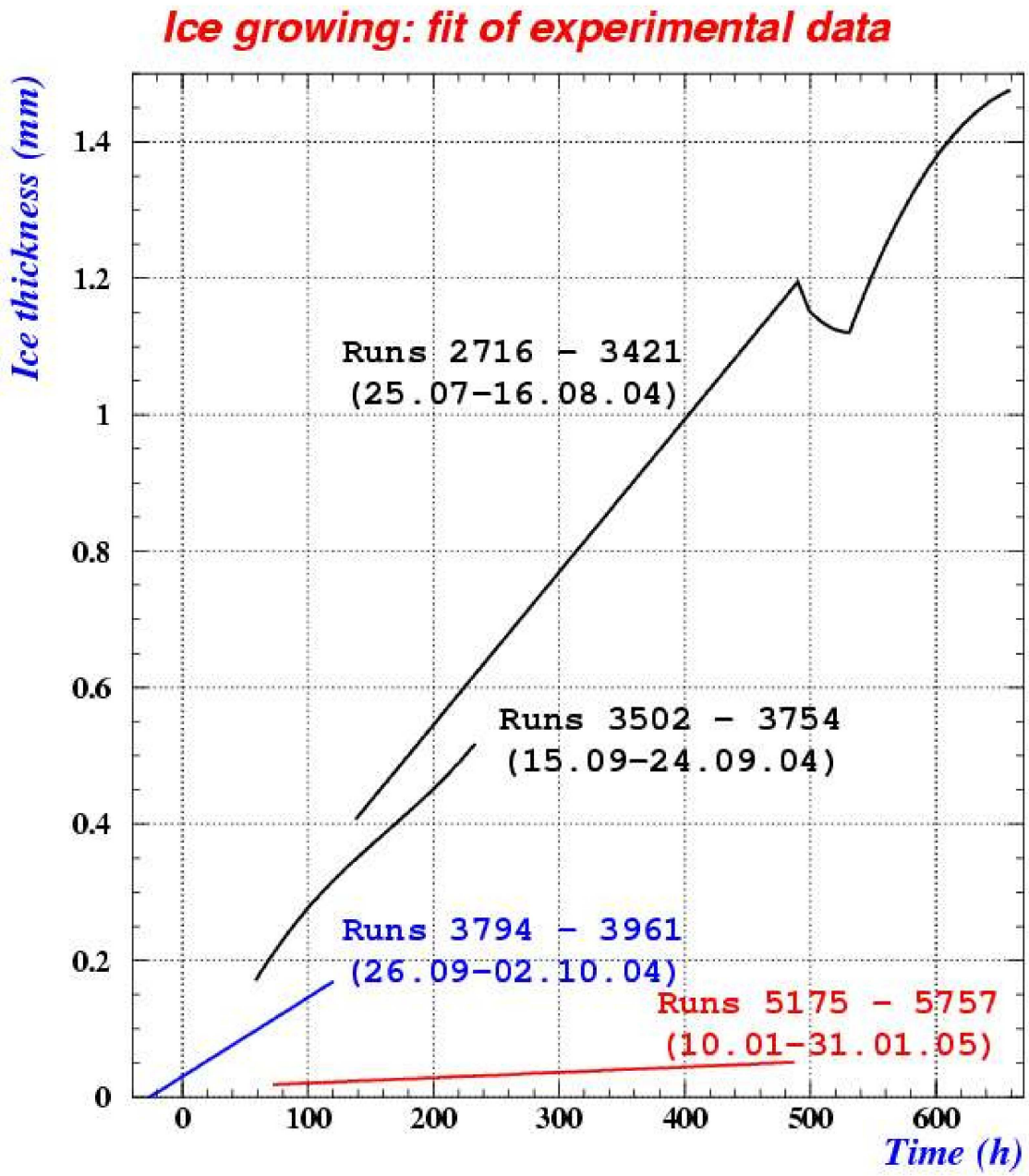

Figure 2.18: Ice thickness on H_2 target as a function of time for different periods. Time zero on the plot corresponds to the completion of the target being filled. The two uppermost lines correspond to runs in July, August, and early September of 2004, before the ice problem was discovered. The next line down is from data taken in late September and early October, at which time the 120 μm of PEN foil had been added. The last line is from January of 2005, which had, in addition to the foil, 20 μm of kapton surrounding the target cell [22].

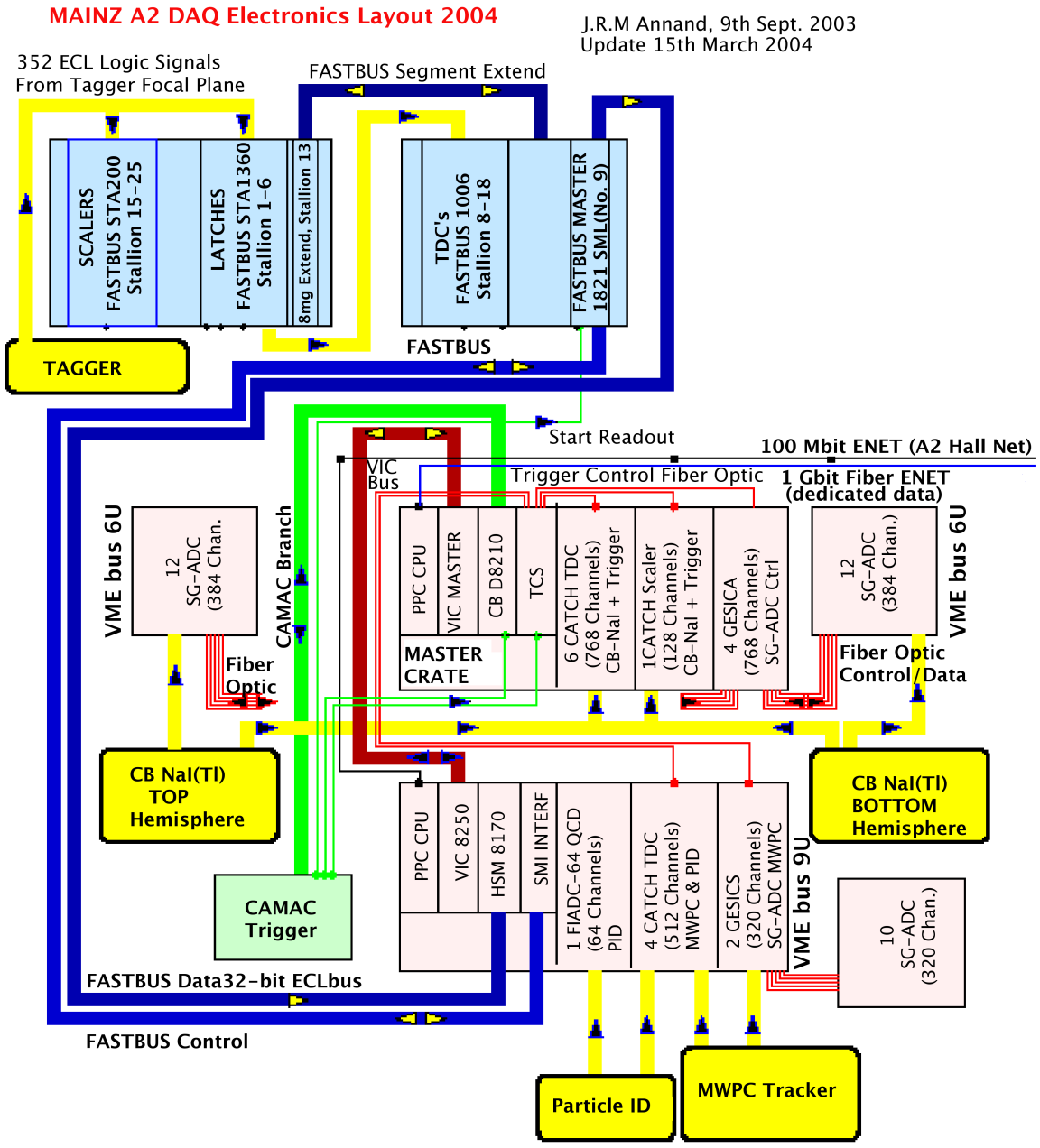

Figure 2.19: The overall data acquisition electronics setup.

2.8.2 Tagger operation

The first task was the determination of the energy of the photon from the recoil electron deflected by the tagging magnet. The energy of the recoil electron was deduced from the deflection using two scintillation counters in coincidence located in the magnet's focal plane. The recoil electron from a Bremsstrahlung reaction goes in the forward direction. Like the photon, nearly half of the electrons are emitted within a cone called the characteristic half angle which is only 0.6 mrad. The momentum is determined from the radius of curvature which in turn is determined from the known position of the Tagger and the Tagger counters in the focal plane of the magnet. Because of the high probability of accidents in the Tagger, it was not used to initiate the event trigger, the CB and TAPS were responsible for this (referred to here as the experimental trigger). The target length corresponded to 0.0055 radiation-lengths, in which on average 0.43% of the incident electrons interacted, producing photons.

The output signals from the PMT's attached to each scintillator went to discriminators of the Plessey SP9687 type and then to coincidence logic units. To reduce accidentals in the Tagger, the tagging counters were aligned in a staggered formation as shown in Figure 2.20. This improves the resolution by a factor of two.

After the coincidence units, the signals needed to be delayed by approximately 500 ns in order to be synchronized with the experimental triggers. The signals were carried over 3M type 3655 cables, which gave 250 ns delay, and were reshaped and delayed by an additional 250 ns (see Figure 2.21). A VME computer read a continuously sampling scaler which was the number of tagging electron hits for each channel. A multi-channel latch with one bit for each channel was used, the pattern of bits shows

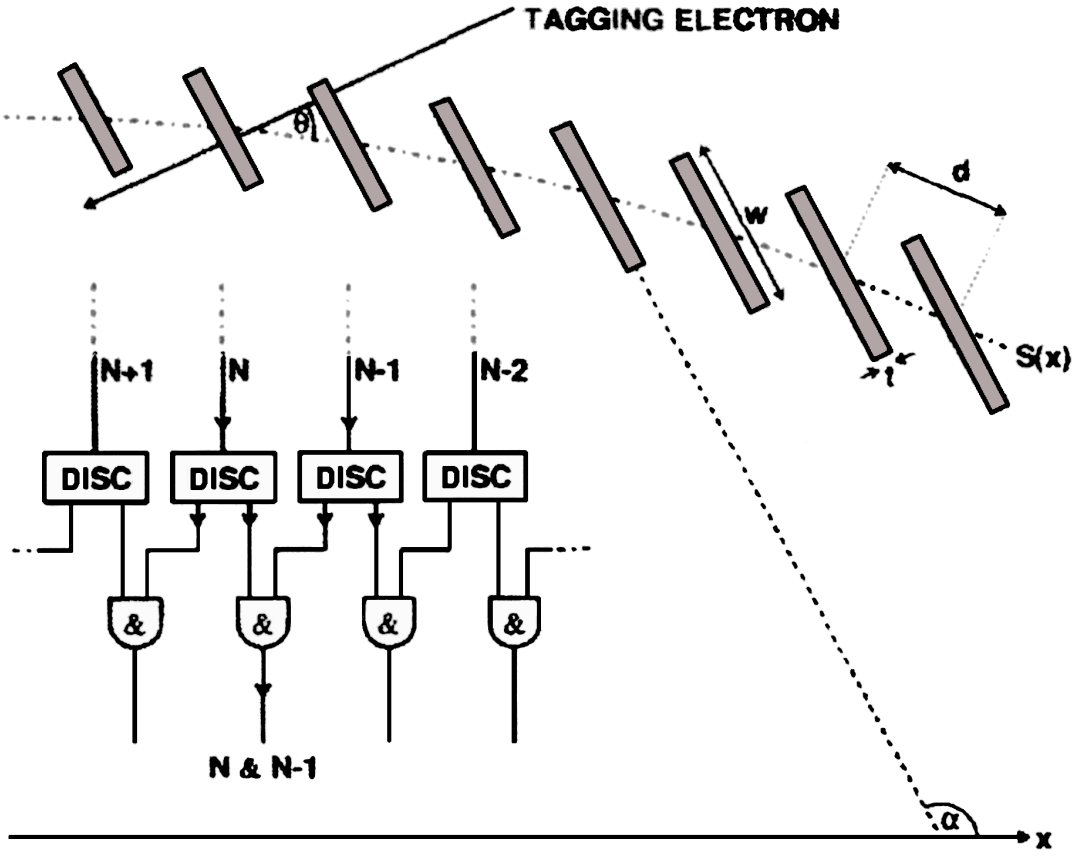

Figure 2.20: Schematic of the scintillator position along the curved focal surface, S(x), showing how they are set normal to the path of the tagging electrons. Also shown is a representation of the coincidence requirement between adjacent channels [19].

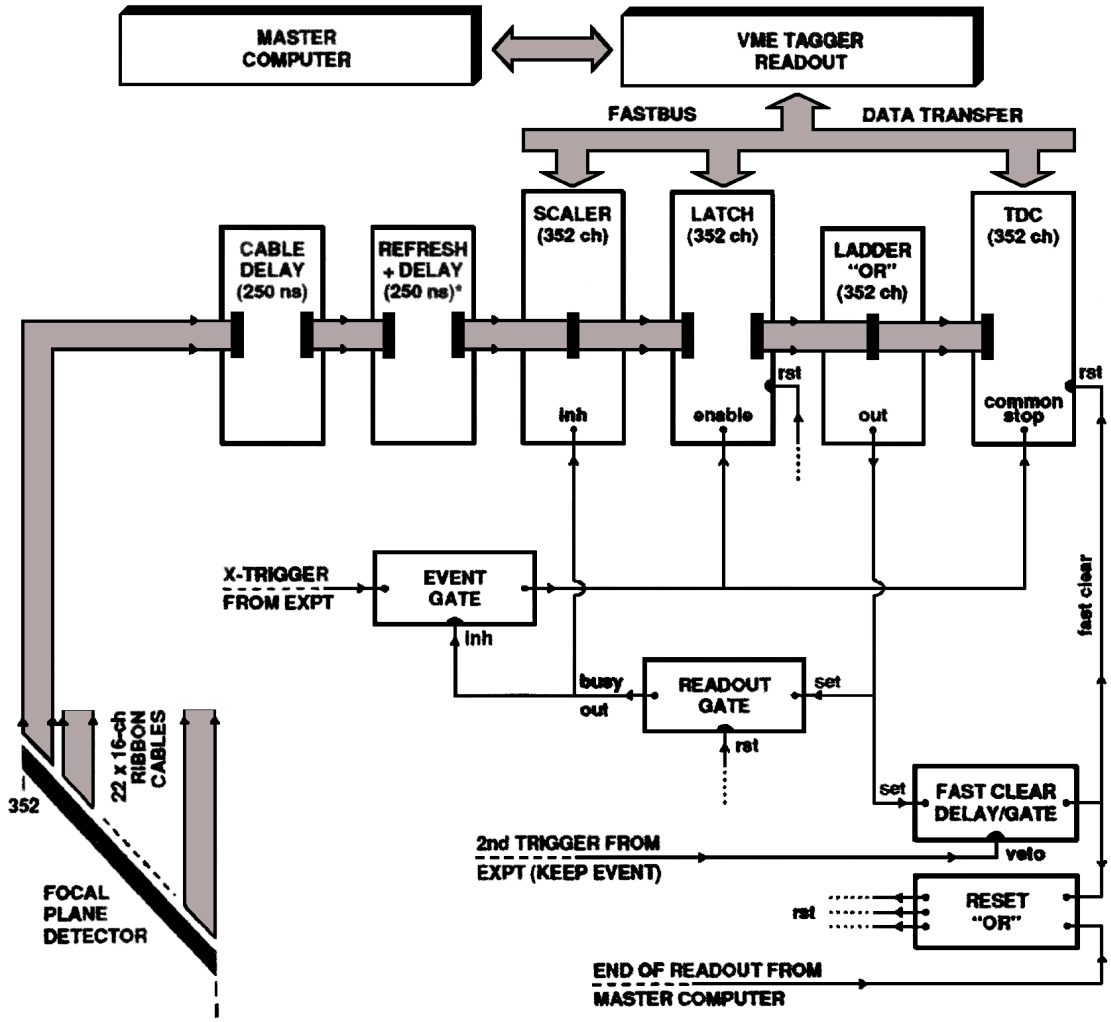

Figure 2.21: Trigger electronics involved in the correlation of Tagger hits and event data [19].

the number and location of elements which fired in an event.

2.8.3 Event triggering

The experimental setup used event triggering from the CB and TAPS, based on energy deposited and number of clusters above a certain energy threshold. Typically particles incident on the CB and TAPS do not deposit all their energy in one crystal, rather in a cluster of adjacent crystals. See section 4.2 for more on cluster definitions.

In our experiment, only the CB was used for triggering. Our trigger required a total energy deposit in the CB of 350 MeV, and a block multiplicity of greater than or equal to 3, where a valid block was defined when the energy of all counters in a block combined to more than 30 MeV. Figure 2.10 displays the block groups. For multiplicity 2 events, only 1 in 40 events were recorded, as they did not contribute to the reaction being studied but were recorded for monitoring purposes. There were a large number of such events due to π^0 production, so not recording all of them reduced unwanted events. Events with more than 3 clusters are possible $\eta \rightarrow \pi^0\gamma\gamma$ candidates. Figure 2.22 shows a schematic of the trigger used.

Since the event triggers for events were initiated by the CB, the coincidence timing window of the Tagger counter elements were wide, approximately 200 ns, in order to accommodate channel-to-channel delay differences in either the Tagger channels or in the different channels of the experimental detectors, as well as accidentals. Figure 2.23 shows the time spectrum for a coincidence between the experimental trigger

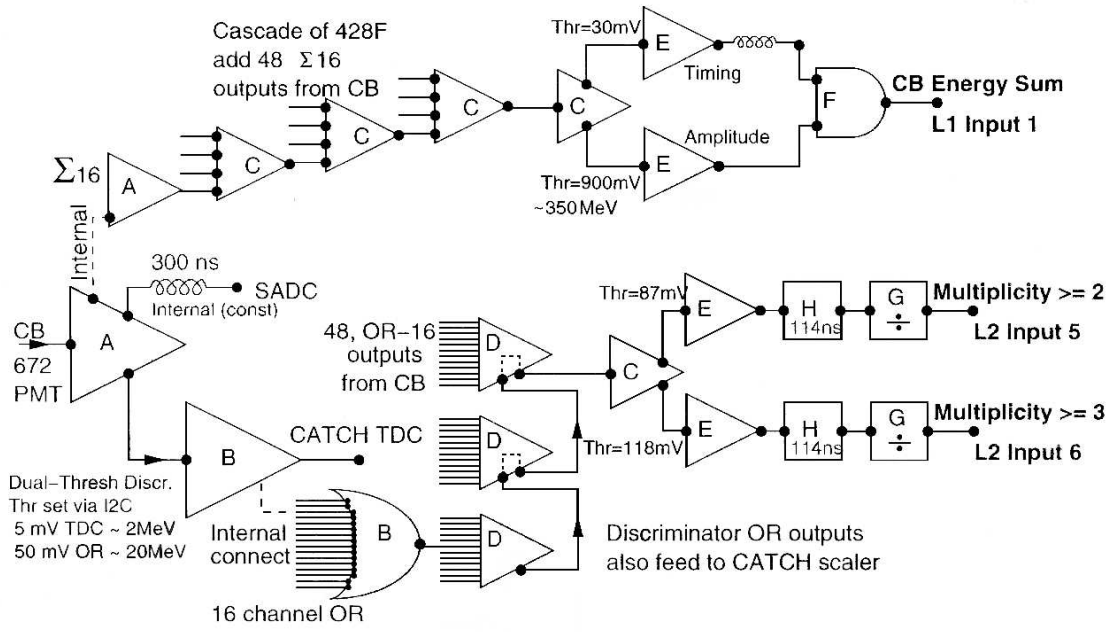

Figure 2.22: Schematic of the trigger used in this experiment.

and the Tagger elements, defined as a coincidence between two adjacent, overlapping counters. The peak, or prompt region, in the spectrum from true coincidences sits on top of a random background covering the entire time gate. In the analysis the random background contribution was corrected for by the subtraction of events in the shaded region of the figure from the prompt region. This was done for every Tagger element hit in an event, which means that each event could potentially contribute multiple times to both the prompt and random selections, however, it was believed that this method properly subtracted the random background.

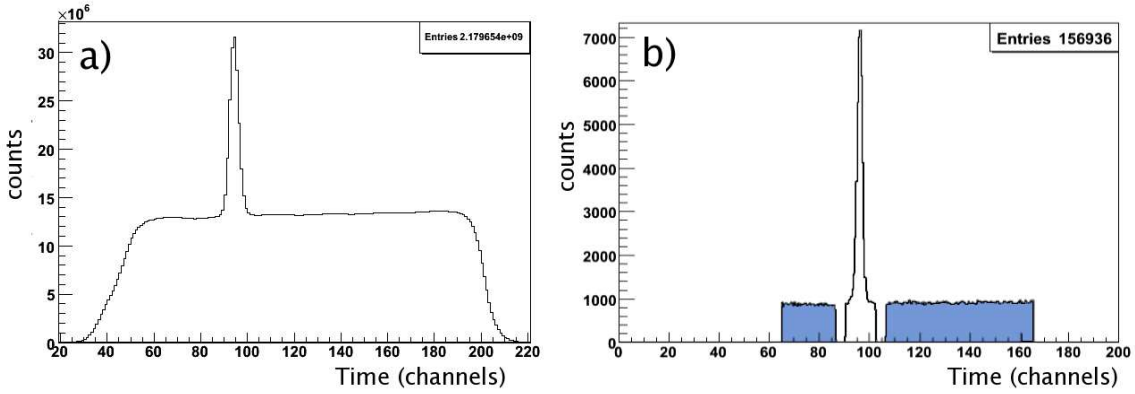

Figure 2.23: a) Coincidence time spectrum between experimental trigger and the Tagger detector elements for all cluster types. b) The same plot for selected $\eta \rightarrow \pi^0\gamma\gamma$ events where the shaded region is the random region that is subtracted from the central prompt region, as described in the text. The ratio of prompt to random events for the selected events is higher than for all events as a whole due to the analysis process, described in chapter 4.

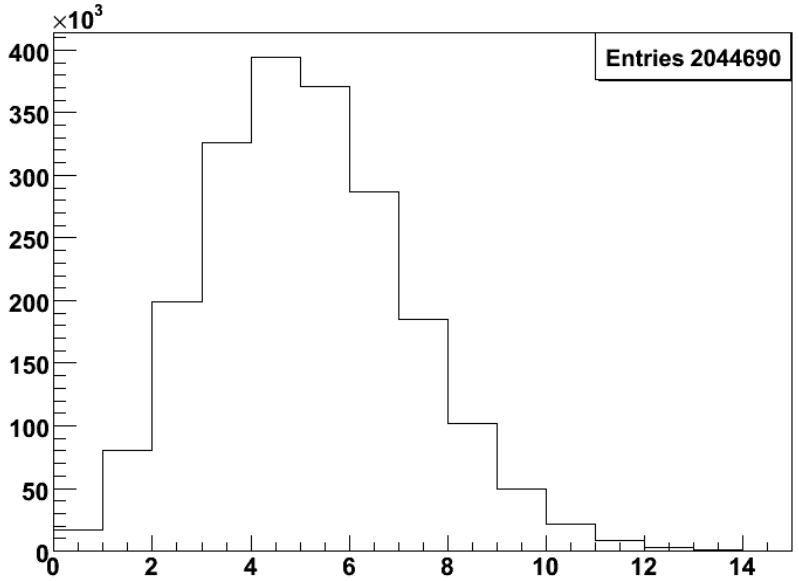

Figure 2.24: A typical distribution of the number of hits in the Tagger detector elements.

2.8.4 CB functioning

An outline of the CB electronics is shown in Figure 2.25. The high voltage power was supplied to the CB by 4 high voltage units, the voltage was set at 1500 V, each PMT was connected in parallel to the others. The current in each counter was 5×10^{-4} amps. The signals from the PMT's were sent in groups of 8 to a split delay module similar in design to those used for the WASA[8] detector at CELSIUS in Uppsala, in which Field Programmable Logic Arrays (FPGA) chips were employed. There were 3 output signal paths from the split delay module, the first of which gave an analog sums of 4 or 16 channels which were used in making trigger decisions, allowing for fast triggering.

The second output signal path went into a PM98 dual threshold discriminator which fed into individual COMPASS CATCH TDC's and scalers used in making trigger decisions. The scalers allowed for fast online diagnostics during the experimental runs, monitoring such things as the trigger rate, event rates in the CB, TAPS and the Tagger, the data acquisition livetime, and electron beam rate. The TDC's were of a continuously sampling, multi-hit design with approximately 100 ps resolution.

The third output from the split delay modules went into a sampling ADC (i-SADC 108032) which sampled the pulses at 40 MHz. Integrals of the signals were made in three sections: pre-, during- and after- the scintillation pulse of a shower. The pre-signal was subtracted inside the module from the signal. This corrected for ambient

[8] WASA: Wide Angle Shower Array

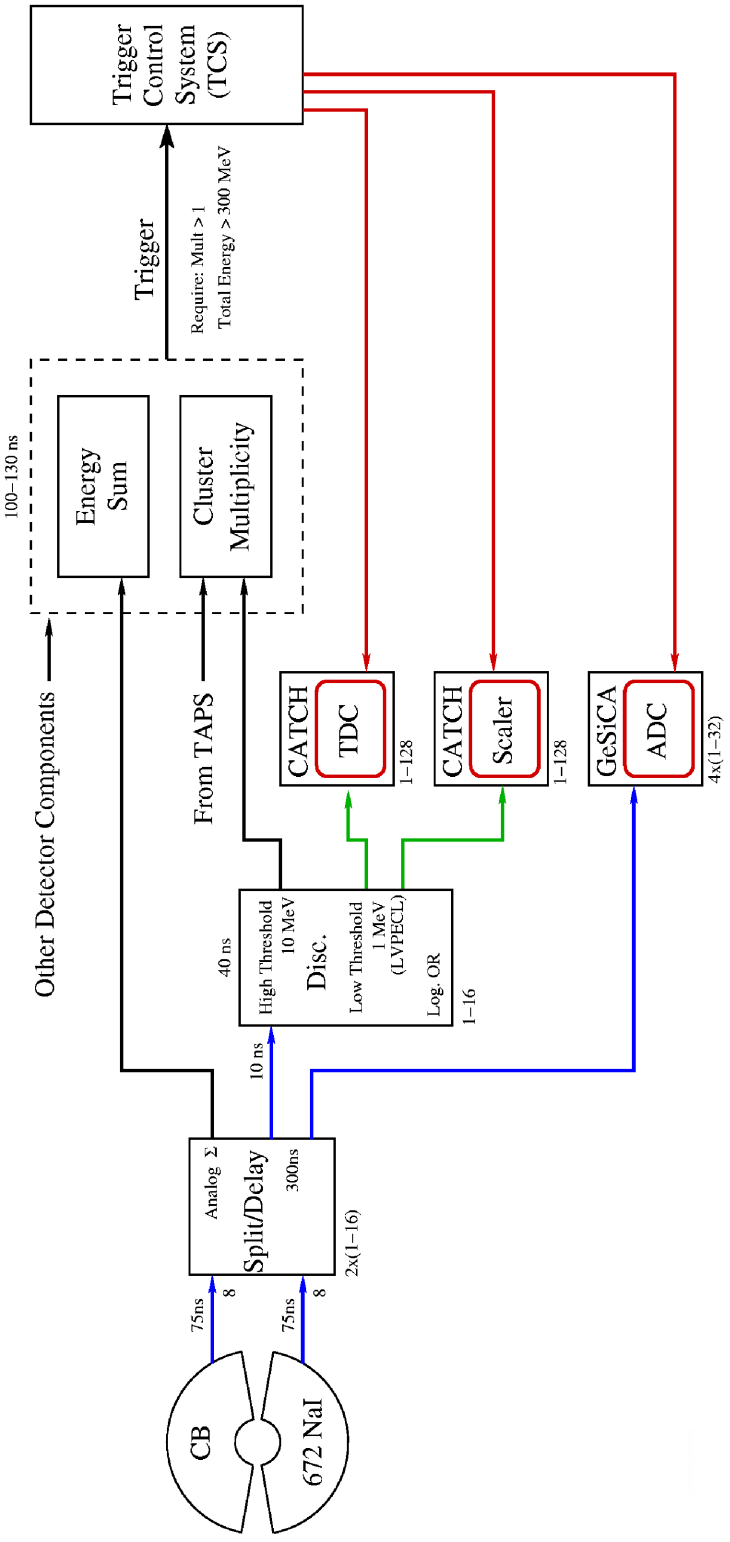

Figure 2.25: Schematic of electronics readout for the CB.

light in the NaI crystals due to previous interactions and the long tail of the NaI pulse. The post-signal is compared inside the module with the signal to determine if there is a second interaction. Integrating the signal also reduced the data volume.

The ADC's, TDC's and scalers used GeSiCA and CATCH electronics which had been developed for the COMPASS experiment at CERN. These devices were read out on VME buses via two power PCs.

2.8.5 TAPS

The electronics for a single channel of TAPS is shown in Figure 2.26. The signals from each BaF_2 crystal were read out by a Hamamatsu R2059-01 photomultiplier, then distributed to a constant fraction discriminator(CFD), two leading edge discriminators (LED), and four charge-to-amplitude converters (QAC).

The LED outputs could be used for event and trigger selection, though that was not done for this experiment. The CFD identifies the response of the detector, making it the start signal for the QACs as well as for the time-to-amplitude converter (TAC) for the timing measurement. The BaF_2 crystals respond differently to photons and nucleons, specifically the signal shape measured over a short time interval (~20 ns) and a long time interval (~2 μs) are different. The QACs measured the slow and fast components of the signal shape, making it possible to differentiate between photons and nucleons, though this capability was not employed in this analysis.

2.8.6 PID

An outline of the PID electronics can be seen in Figure 2.27. The output from the PMT's went to a LeCroy 612 NIM $\times 10$ amplifier, then fan out three ways. The output first was to a 300 ns delay and then into FIADC-64 QDC's for measurements of energy deposited. The second path for the signals was through a CAMAC discriminator, then it went to an ECL-toLVPECL module, into CATCH TDC's for timing measurements. The third was also through a CAMAC discriminator, then through a CFD, a delay of ~190 ns, and into the trigger system, allowing triggering based upon PID information.

2.8.7 Scalers

There were a number of scalers recorded during experimental runs which could be accessed later for use during analysis, many were also displayed on monitors in the experimental counting room during runs. The scalers monitored during runs were: P2 ion chamber, Ladder OR for 16 channels of the Tagger (for monitoring rate), ratio of Ladder OR to P2 ion chamber, Farady Cup (the rate of electrons entering the hall), TAPS trigger rate, event interrupt rate, CB energy sum, 1^{st} level strobe, CB OR rate, CB bottom hemisphere rate, CB top hemisphere rate, TAPS OR LED rate, TAPS OR CFD rate, DAQ livetime, and Pb-glass (used only during tagging efficiency runs). Other scalers recorded, though not displayed during runs, were: Fast clear rate

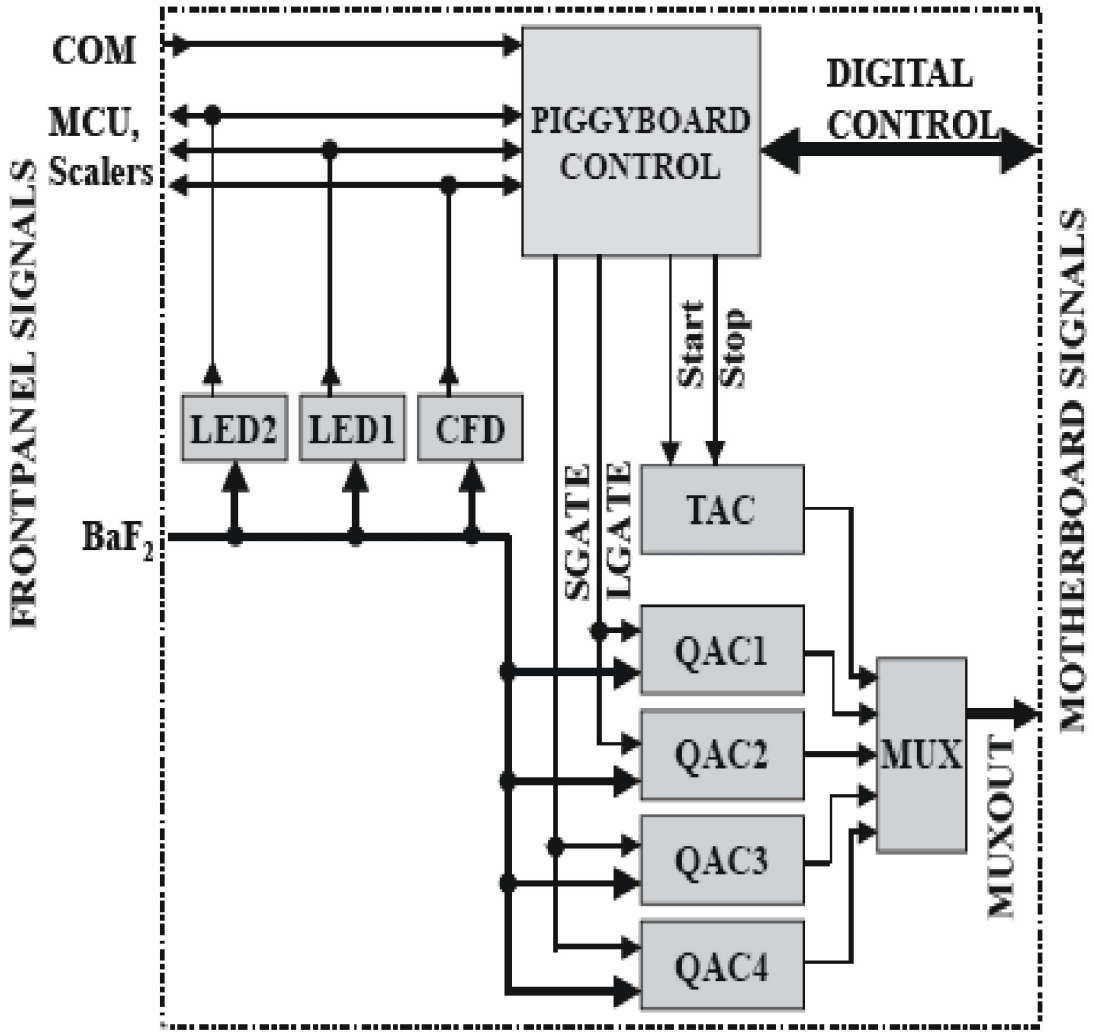

Figure 2.26: TAPS electronics for a single detector channel [23].

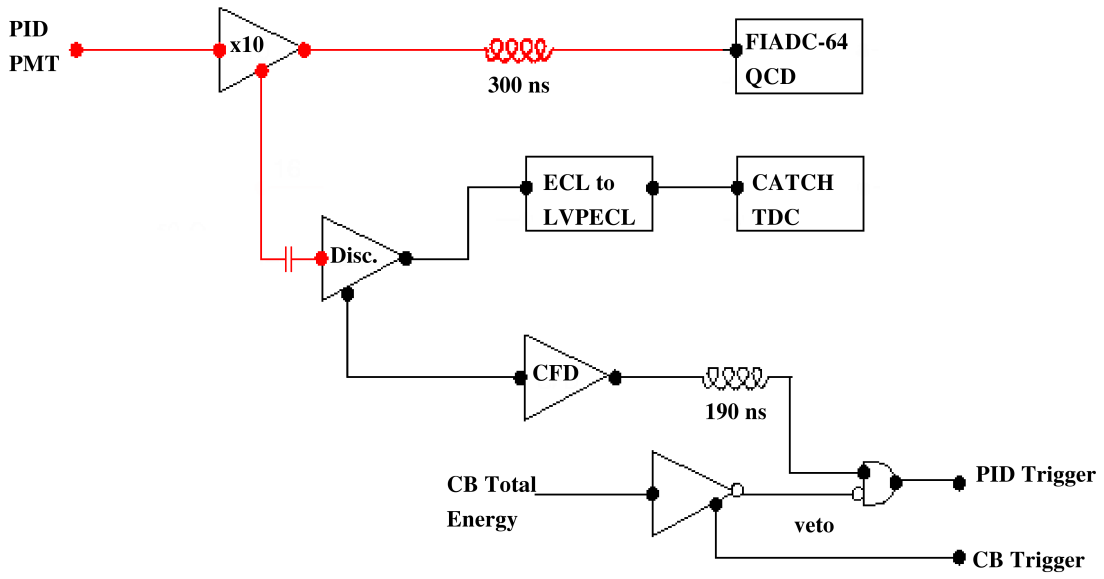

Figure 2.27: PID electronics.

of the Tagger, X-trigger rate, Tagger coincidence rate, 2^{nd} level trigger, S11 pulser, and CATCH TDC rates.

Chapter 3

Data Taking

The data examined in this thesis were taken in two run periods in November and December of 2004. Statistics concerning the two runs are given in Table 3.1. Data taking was typically done 24 hours a day, but at times interrupted for beam optimization and equipment repair as well as tagging efficiency runs, hence the hours of recorded data are less than the total time devoted to the experiments.

In addition to the scalers monitored mentioned in section 2.8.7, various simple spectra were also monitored during runs, including: the number of clusters in the CB and TAPS along with their angles, energies, and time, TAPS veto hits, PID hits, their number, location, and time, Tagger ladder hits, their number, energy, time, and the invariant mass of 2 cluster events, which was often a π^0.

The integrated luminosities quoted in Table 3.1 are approximate values that use an average tagging efficiency of 35%, the average rate of electrons hitting the tagger, the target dimensions mentioned in section 2.7, and a Bremsstrahlung spectrum for the production of photons in the energy range for those Tagger elements which were

	Experimental Run 1	Experimental Run 2
data taken	04/11 to 15/11, 2004	30/11 to 15/12, 2004
beam time	270 hours	290 hours
recorded data	207 hours	245 hours
volume of data recorded	463 GB	542 GB
integrated luminosity	860 nb^{-1}	860 nb^{-1}
number of η's produced	1.0×10^7	1.0×10^7
ratio of full to empty target	~6	~5

Table 3.1: Experimental Run Summaries

turned on at the time, as reported in section 2.3. The number of η's listed in the table comes from assuming an average cross section for eta production of 12 pb. The number of η's produced as estimated from our recorded $\eta \rightarrow 3\pi^0$ events is presented in appendix D.

Chapter 4

Analysis

This chapter describes the various aspects of the data analysis process including event reconstruction, kinematic fitting, Monte Carlo simulations, background suppression and subtraction, selection of $\eta \to \pi^0\gamma\gamma$ events, and the determination of the $\eta \to \pi^0\gamma\gamma$ branching ratio.

4.1 Overview of Analysis

Experimentally one does not detect the actual η nor π^0 particles, rather the photons into which they decay. When particles strike the crystals in the detectors, they produce electromagnetic cascades which spread the energy of the particles amongst a group of adjacent crystals, known as a cluster. Protons and muons typically have clusters comprised of one or two crystals, while photons and electrons spread their energy among many more. The π^0decays into two photons with a branching ratio of $\mathrm{BR}(\pi^0 \to \gamma\gamma) = 98.8\%$, so for our experiment, in which a photon was incident upon

a proton, the final state that was examined consisted of 4 photons plus a proton.

$$\gamma p \rightarrow \eta p \rightarrow \pi^0 \gamma\gamma p \rightarrow \gamma\gamma\gamma\gamma p \tag{4.1}$$

The knowledge of the directions of travel and energies of the final-state of particles in an event, along with information on the direction and energy of the incoming photon beam, allow one to deduce which reactions occurred that give rise to a $4\gamma p$ final state.

The number of $\eta \rightarrow \pi^0\gamma\gamma$ events is determined using the invariant-mass, $\tilde{m}$, spectrum of 5 cluster events. We expect a peak in $\tilde{m}$ at the value of the η-meson mass, m_η. However, there are some serious backgrounds to consider. First there is the decay $\eta \rightarrow 3\pi^0 \rightarrow 4$ clusters, which happens when two sets of two photon showers overlap, producing a total of two clusters. This background is particularly bad because it has an $\tilde{m}$ with a peak at m_η, as the two remaining photons of the original six can combine to have the π^0 mass, m_{π^0}. Another background is $\eta \rightarrow \gamma\gamma$ when there are two split-off showers. It also has a peak in the $\tilde{m}$ spectrum at m_η. This decay is minimized by requiring that two of the photon clusters have $\tilde{m}$ close to m_{π^0}. Finally we have $2\pi^0$ production that, due to poor resolution was not identified as $\gamma p \rightarrow \pi^0\pi^0 p \rightarrow 4\gamma p$, mistakenly results in false $\pi^0\gamma\gamma$ identification. The first background, $\eta \rightarrow 3\pi^0$, is minimized using a cut based on the overlap parameter, or effective radius, R, which will be discussed in section 4.5. The $2\pi^0$ and $\eta \rightarrow \gamma\gamma$ background are suppressed by cuts on $\tilde{m}\,(\pi^0\gamma\gamma)$ versus $\tilde{m}_{max}\,(\pi^0\gamma)$, and will also be discussed in section 4.5. The random background which was subtracted from the prompt region, as mentioned earlier in section 2.8.3, did not contribute to the number of $\eta \rightarrow \pi^0\gamma\gamma$ events, as it produced no peak or depression in the invariant mass spectrum near the location of

m_η. Examples of the random signal subtracted can be seen in section 4.5, Figures 4.7 through 4.9. Empty target contributions were also measured, the weight factor for which was taken from the ratio of the total number of tagged photons in the full target runs as compared to the number in the empty target runs. The statistics for empty target runs was too low to be of use in contributions to 5 cluster events, but was used in the examination of $\eta \to 3\pi^0$ events.

Kinematic fitting was used as the main means in discerning which events were good $\eta \to \pi^0\gamma\gamma$ candidates. The fraction of false events was determined by a detailed Monte Carlo simulation of the major backgrounds. Monte Carlo simulations were also used to determine the detection efficiency of the $\eta \to \pi^0\gamma\gamma$ signal, which combined with a determination of the total number of η's can be used to calculate the branching ratio. The matrix element for $\eta \to \pi^0\gamma\gamma$ decay amplitude is not known, it was assumed to have the phase space distribution. The CERN program GEANT was used in the Monte Carlo simulations in order to track particles in the detector setup.

Due to the substantial noise present in the December 2004 data set, only the November data is reported for this thesis. In the December data, the contribution to events being searched for, $\eta \to \pi^0\gamma\gamma$, was comparable to that found in the November data set, but the instability of the beam and detectors during December caused a deterioration in the resolution. This reduced resolution was sufficient such that the inclusion of the December data did not help in the overall determination of the number of $\eta \to \pi^0\gamma\gamma$ events.

4.2 Clusters

Events in this experiment are the result of an incoming photon interacting with protons contained in the liquid hydrogen target. The final-state particles of an event, that strike the CB or TAPS, produced showers which spread their energy among a cluster of adjacent crystals. For protons, the clusters were typically restricted to one or two crystals, as was found in Monte Carlo simulations and experimentally measured reactions with little background, such as $\eta p \rightarrow 3\pi^0 p$.

A minimum energy deposit in a crystal of 2 MeV was required so that it would be counted as part of a cluster in the CB. A total minimum cluster energy of 15 MeV was required in order to help reduce the chance that a split off cluster was treated as a separate cluster. The total number of crystals was restricted to 13, that is, the central crystal plus the 12 nearest neighboring crystals, see Figure 4.1(a). For clusters in TAPS, the minimum energy deposited in one crystal was 3 MeV and a total cluster energy of 15 MeV was required for clusters to be considered. The total number of crystals included in a cluster was restricted to 7, where the central crystal and its 6 nearest neighbors were candidates for inclusion in a cluster. Appendix G has more information on electromagnetic cascades and their relation to cluster sizes used.

When defining the location of a cluster in the CB or TAPS, a weighted sum of crystal face locations (relative to the center of the CB) and energy deposition in that crystal were used:

$$\vec{P}_\gamma = \frac{\Sigma_i^N \overrightarrow{C_i} \sqrt{E_i}}{\Sigma_i^N \sqrt{E_i}} \tag{4.2}$$

where $\overrightarrow{C_i}$ refers to the coordinates of the crystal's face, E_i is the energy deposited,

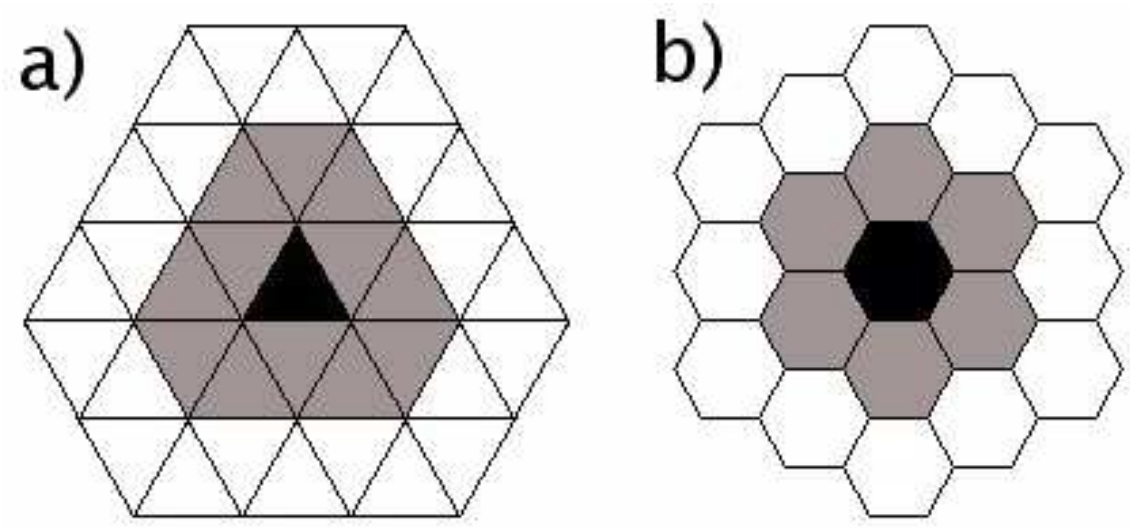

Figure 4.1: Picture of an ideal event in a) the CB and b) TAPS. The central crystals are darkened, they are surrounded by the nearest crystals which potentially could be part of a cluster. Outside this layer of crystals is shown the next adjacent layer.

and N is the number of crystals in the cluster.

With the knowledge of cluster locations, photon directions, and energies deposited for an event, along with the incoming photon beam information from the Tagger, one can determine what particle reactions may have occurred. For instance, in looking for the $\eta \to \pi^0\gamma\gamma$ decay, 5 cluster events are examined with the assumption that one of those cluster is a proton, various quantities can then be constructed, such as the invariant mass of the photons, the associated missing mass, and the total energy and momentum before and after the interaction of the beam photon with the target. By comparing the measured values of these quantities with the expected values, one can then determine the likelihood, or probability, that the event was a $\eta \to \pi^0\gamma\gamma$ case. In order to test events in a rigorous and objective way, kinematic fitting was employed. Many Monte Carlo simulations were investigated.

4.3 Kinematic Fitting

This section describes the kinematic fitting process, which was the primary tool used to determine which events were good $\eta \to \pi^0\gamma\gamma$ candidates. The kinematic fitting which was employed utilizes the method of constrained least squares with Lagrange multipliers. In this process, adjustments of combinations of parameters were tested, which included the energies of clusters, the interaction vertex, directions of the clusters, photon beam momentum, and the identification of clusters as protons or photons. For each hit in the Tagger ladder, all possible combinations of particle assignments to each cluster were tested, such as protons and photons, and which pair of photons was assigned as the decay products of the π^0, the best combination saved for further analysis. For example, when looking for events that might satisfy the hypothesis $\gamma p \to \eta p \to \pi^0\gamma\gamma p \to 4\gamma p$, there are 5 clusters, one of which is a proton, the rest photons, two of which are the decay products of the π^0, giving 30 possible combinations to test.

For this analysis, one of the things that was done was to look for events which kinematically satisfied the hypothesis $\gamma p \to \pi^0\gamma\gamma p \to 4\gamma p$ while failing the hypothesis $\gamma p \to 2\pi^0 p \to 4\gamma p$. In looking for the former, one requires that one pair of the photons combines to form a π^0. Mathematically this can be written for the two photon 4-vectors, P_1 and P_2:

$$(P_1 + P_2)^2 - m_{\pi^0}^2 = 0 \tag{4.3}$$

For kinematic fitting in general, a set of n measured parameters, which can be denoted

by a vector, x:

$$x = \begin{bmatrix} x_1 \\ x_2 \\ \vdots \\ x_n \end{bmatrix} \tag{4.4}$$

would ideally satisfy k constraint equations:

$$f(x) = \begin{bmatrix} f_1(x) \\ f_2(x) \\ \vdots \\ f_k(x) \end{bmatrix} = 0 \tag{4.5}$$

Generally however, a set of measured parameters, x_0, will not satisfy the constraint equations exactly, but corrections, Δx, may be calculated such that $x_0 + \Delta x$ satisfy the equations within some level of desired precision:

$$f(x_0 + \Delta x) = 0 \tag{4.6}$$

In the method of least squares, the corrections must satisfy:

$$\Delta x^T V_x^{-1} \Delta x = minimum \tag{4.7}$$

where $V_x^{-1}$is the inverse of the covariance matrix associated with x:

$$V_x = \begin{bmatrix} \sigma_{11} & \sigma_{12} & \cdots & \sigma_{1n} \\ \sigma_{21} & \sigma_{22} & \cdots & \sigma_{2n} \\ \vdots & \vdots & \ddots & \vdots \\ \sigma_{n1} & \sigma_{n2} & \cdots & \sigma_{nn} \end{bmatrix} \tag{4.8}$$

The next step is the introduction of a Lagrange multiplier, λ, for each constraint equation:

$$\lambda = \begin{bmatrix} \lambda_1 \\ \lambda_2 \\ \vdots \\ \lambda_k \end{bmatrix} \tag{4.9}$$

Then a stationary point of the function $Q(\Delta x, \lambda)$ needs to be found:

$$Q(\Delta x, \lambda) = \Delta x^T V_x^{-1} \Delta x + 2\lambda^T f(x_0 + \Delta x) \tag{4.10}$$

at which point the derivatives of $Q(\Delta x, \lambda)$ with respect to Δx and λ are required to be zero. Minimization routines written by V. Blobel [24] have been used in this analysis. For this experiment, the measured parameters of each particle detected were the energy and azimuthal and polar angles. Also, the z-vertex interaction point was treated as a measured parameter, centered on zero (the center of the CB) with an uncertainty equal to 1/3 the target length. For the incoming photon, its energy was measured by the Tagger, its momenta transverse to the beam direction, z, were

assumed to be negligibly small, at most approximately 6 hundredths of a percent of the forward momentum.

The covariance matrix V_x is related to the resolutions of our detector components. To examine the correctness of the covariance matrix components, the *pull* parameters of the fitting process need to be examined:

$$pull\,(x_i) = \frac{x_i^{meas} - x_i^{fit}}{\sqrt{V_{x,ii}^{meas} - V_{ii}^{fit}}} \tag{4.11}$$

If the components of V_x are estimated correctly, the *pulls* will follow a normal Gaussian distribution with a mean of zero and a variance of one. Improper estimates of the components of V_x lead to variances in the *pull* distributions different from one, with variances greater than one implying an underestimation of the errors, less than one implying the opposite. Improper estimates of the measured quantities lead to shifts in the means away from zero. An example of some pull distributions can be seen in Figure 4.2.

Additionally, when the covariance matrix components are estimated correctly and the measured events are those that are being hypothesized, the quantity $\Delta x^T V_x^{-1} \Delta x$ in equation 4.10 will follow a normal χ^2 distribution.

Another measure of the quality of an event's fit to a certain hypothesis is the probability of obtaining a certain χ^2 greater than a minimum χ^2_{min} given the number of degrees of freedom, *NDF*, present. To say that the probability of an event satisfying a particular hypothesis is greater than some amount, is also referred to as a confidence

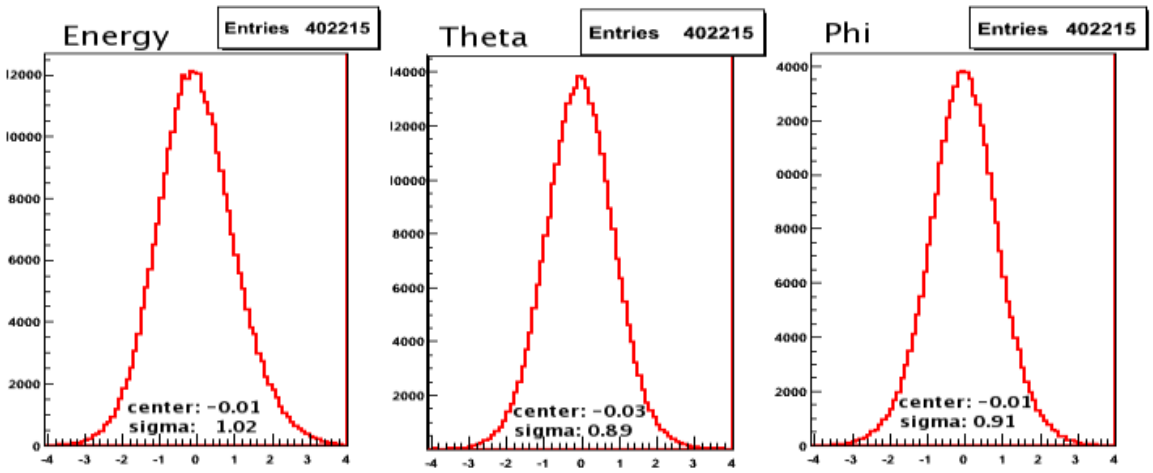

Figure 4.2: An example of the pulls for the energy and angles of one of the photons in a $\eta p \rightarrow 3\pi^0 p \rightarrow 6\gamma p$ kinematic fit test using raw data. As desired, when each distribution is fit with a Gaussian function, the center is close to zero with a σ close to one.

level, CL, of that amount. The NDF in an event is defined as:

$$NDF = (\#.of.constraints) - (\#.of.free.parameters.of.the.fit) \tag{4.12}$$

As an example in the counting of the NDF in an event, take a 5 cluster event in which one of the clusters is assumed to be a proton, the rest photons, and the hypothesis being tested is $\gamma p \rightarrow \pi^0\gamma\gamma \rightarrow 4\gamma p$. In this case there are 4 constraints for the event as a whole from momentum (3 components) and energy conservation, and one for the π^0 mass, for a total of 5 constraints. The unmeasured quantity is the energy of the proton. Since the proton loses its energy in the materials between the target and the NaI and BaF_2 crystals differently for different directions, there is a large uncertainty between its cluster energy and kinetic energy. Therefore it is best to leave this quantity as unmeasured. So this makes the NDF 4. For a 4 cluster event

in which the proton was not detected, the number of unmeasured quantities increases by 2, making the *NDF* 2.

4.4 Monte Carlo Simulations

The main goals of the Monte Carlo simulations studies were to determine the efficiencies of $\eta \to \pi^0\gamma\gamma$ and $\eta \to 3\pi^0$ detection, and investigate the major background processes, namely $2\pi^0$ production and the $\eta \to 3\pi^0$ and $\eta \to \gamma\gamma$ decays.

There were two parts to the Monte Carlo simulations, the event generation and the particle tracking.

As the first step, a program was used to generate the kinematics of events. The input parameters were the target dimensions, mass, and density, also the beam energy, spot size at the target, as well as the beam divergence, for this we used real "beam triggers" recorded in the course of the experiment.

The second step used a program based on the CERN package GEANT, version 3.21, that reads the output of the first program and tracks all particles through volumes of different materials, in a setup that mimics as closely as possible the actual experimental setup. The geometries included were the CB, TAPS, TAPS veto wall, PID, MPC, and the target. The Tagger was not included as it does not directly affect the detection efficiency, although the efficiency of the Tagger was taken into account.

The main parts of the CB geometry were the 672 crystals, the inner steel sphere, the outer aluminum sphere, and the beam entrance and exit tunnels, including the "skirts" on the tunnels.

For TAPS, the geometries of its 510 crystals were included, as well as the veto

wall that was located directly in front of the wall of crystals.

The 24 elements of the PID and the 480 anode wires and 320 cathode strips of the MPC were also included, though the MPC chambers were turned off during the experiment, as they were unable to handle the high rates present in the η running conditions.

The various components of the target assembly were included, consisting of the container, liquid hydrogen, and beam pipe. Also included was the insulation used to combat the ice build up problem discussed in section 2.8.

The energy trigger of 15 MeV for a cluster, mentioned in 4.2, was also included in the Monte Carlo, otherwise the detection efficiencies would have been overestimated.

4.5 Background Suppression and the Selection of $\eta \rightarrow \pi^0\gamma\gamma$ events

To find the $\gamma p \rightarrow \eta p \rightarrow \pi^0\gamma\gamma p \rightarrow 4\gamma p$ events, all 5 cluster events were tested to see if they passed the $\gamma p \rightarrow \pi^0\gamma\gamma p$ kinematic fit test. Additionally, events with clusters in the CB identified as being photons were rejected depending on the energy of the cluster and how many crystals contributed to the cluster. This helped to reduce the background of misidentified photons which were actually protons while only slightly reducing the efficiency of $\eta \rightarrow \pi^0\gamma\gamma$ detection. Similarly, time of flight cuts were made with TAPS to reject misidentified protons and photons.

As mentioned earlier, there were two major background processes which needed to be suppressed in the data. For the first of these, the $2\pi^0$ production reaction does

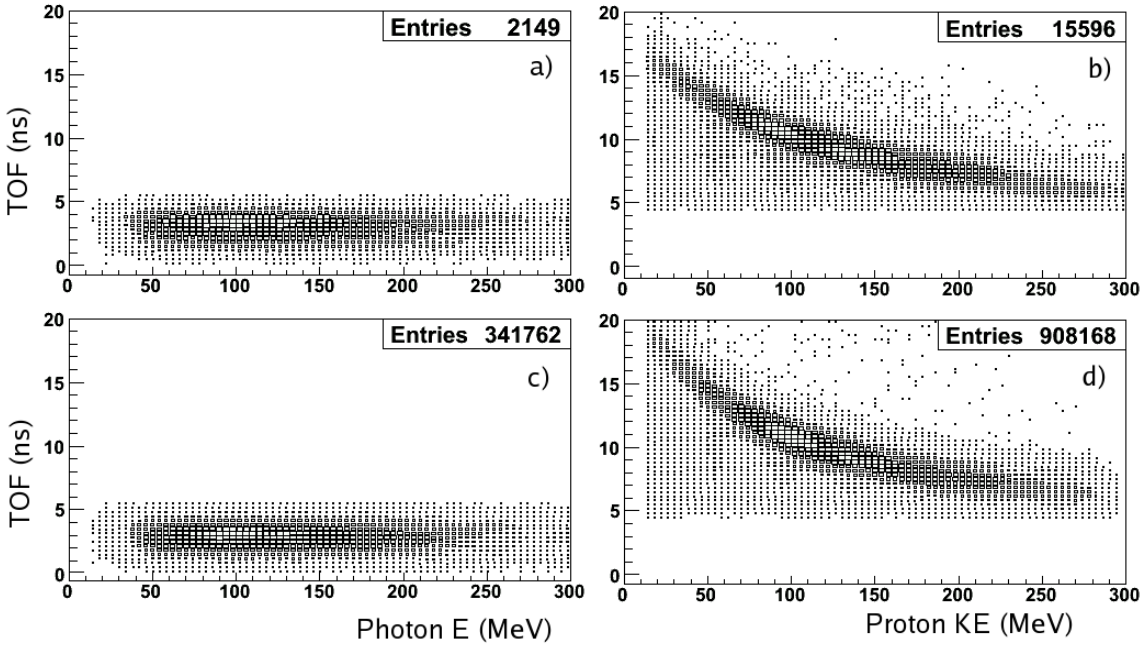

Figure 4.3: Time of flight (TOF) of particles detected by TAPS. Figures a) and c) show particles chosen by kinematic fitting to be photons for data and Monte Carlo, respectively. Plots b) and d) show similar plots for protons detected. Events were rejected below 5.5 ns in the proton TOF plots to exclude photons misidentified as protons, and above 4.5 ns in the photon TOF plots to similarly reject protons misidentified as photons.

not produce a peak in the invariant mass of the four photons at $\tilde{m} = m_\eta$, but it was a very large and broad background which produced many events in the η mass region. The Monte Carlo simulations of the $2\pi^0$ production generally matched the actual data well, but not in all cases, as will be discussed in the next section. Figure 4.4 shows Dalitz plots of both the data and Monte Carlo simulation which passed the kinematic fit test of $\gamma p \rightarrow 2\pi^0 p$ at a confidence level of 2%. There is good enough agreement between data and simulation.

The $2\pi^0$ production is energy dependent, and in the energy range of this experiment, the production of $2\pi^0$ events was on the order of 1000 times that of $\eta \rightarrow \pi^0\gamma\gamma$ events. In selecting $\eta \rightarrow \pi^0\gamma\gamma$ candidates, all events which passed the kinematic fit test of the $\gamma p \rightarrow 2\pi^0 p \rightarrow 4\gamma p$ hypothesis at the 0.001% confidence level were rejected, and the remaining cases which passed the $\gamma p \rightarrow \pi^0\gamma\gamma p \rightarrow 4\gamma p$ hypothesis at the 10% confidence level were chosen as event candidates and used for further analysis.

Even with the rejection of events satisfying the $2\pi^0$ hypothesis, the detection efficiency for misidentifying $2\pi^0$ events as possible $\eta \rightarrow \pi^0\gamma\gamma$ candidates was approximately 0.2%. In order to further suppress this background, cuts on the total photon invariant mass, $m\,(\pi^0\gamma\gamma)$, versus the maximum invariant mass of the selected π^0 and one of the photons, $m_{max}\,(\pi^0\gamma)$, were made, as pioneered by Prakhov [17]. Plots of $m\,(\pi^0\gamma\gamma)$ versus $m_{max}\,(\pi^0\gamma)$ can be seen in figure 4.5, along the cuts tested.

The effects of the $m_{max}\,(\pi^0\gamma)$ cut #2 from Figure 4.5 on the data and Monte Carlo are shown in Figure 4.7 and 4.8. It can be seen that quite a lot of the background below the η mass that is present in Figure 4.7.a where there are no cuts is reduced, leaving a more prominent peak at the location of the η mass in Figure 4.8.a. The

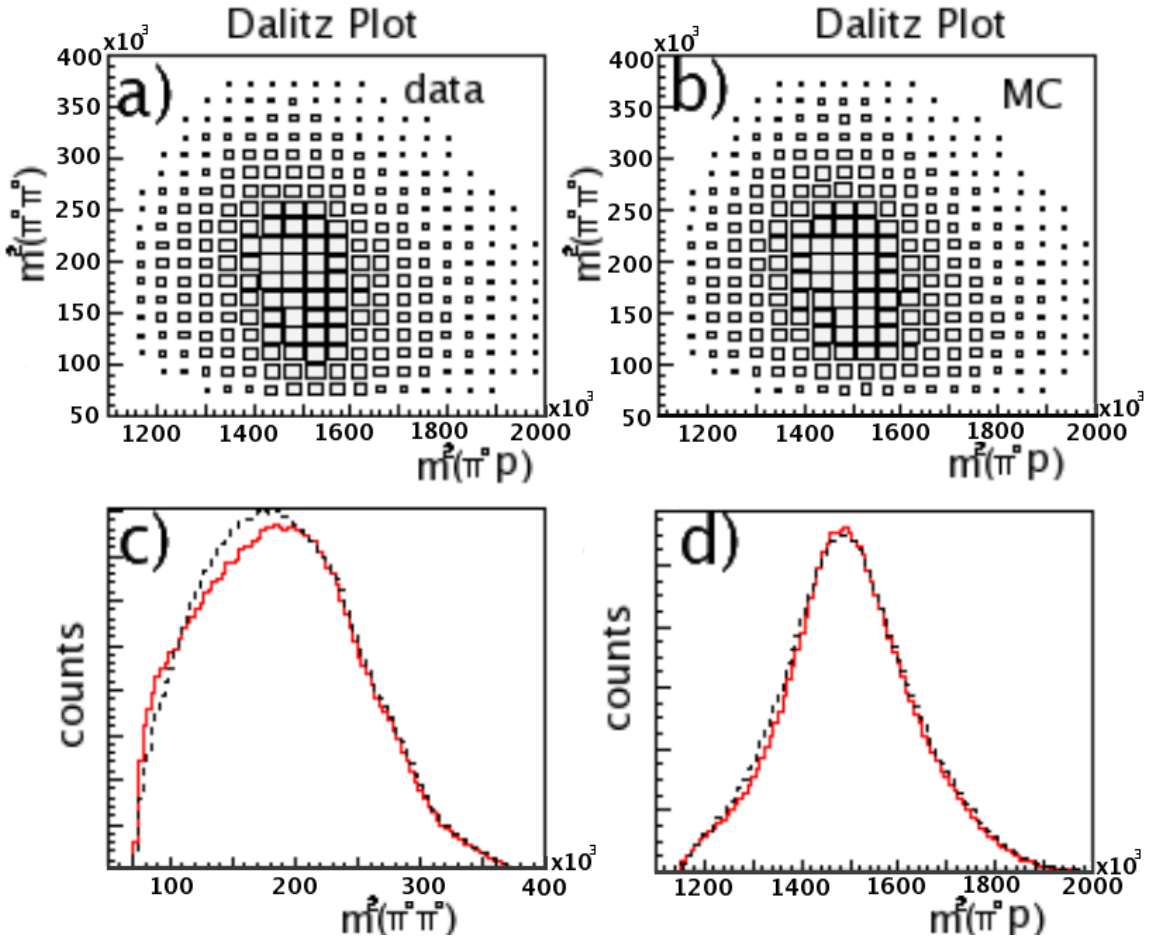

Figure 4.4: Dalitz plots of the square of the invariant mass of the sum of one of the two pions and the proton, $m^2(\pi_i^0 p)$, versus the square of the invariant mass of the the sum of both pions $m^2(2\pi^0)$, for 5 cluster events passing the $\gamma p \to 2\pi^0 p$ kinematic fit test at the 2% confidence level for a) data and b) Monte Carlo simulations. There are two indistinguishable π^0s requiring that each event be plotted twice. Projections of the Dalitz plots on the c) $m^2(\pi_i^0 p)$ and d) $m^2(2\pi^0)$ axes, where the solid line is data and the dashed line is simulation, help to illustrate the good agreement between data and simulation.

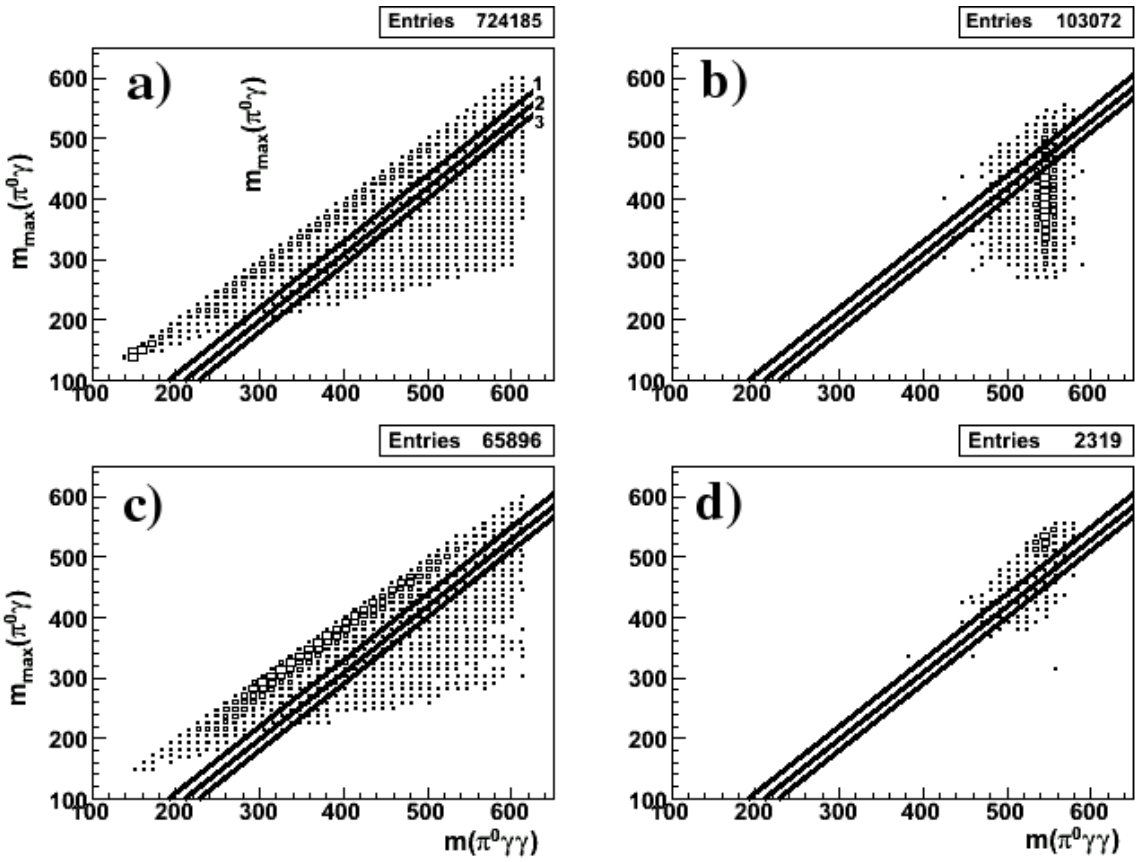

Figure 4.5: Density plots of $m\,(\pi^0\gamma\gamma)$ versus $m_{max}\,(\pi^0\gamma)$ for events already passing the kinematic tests, for a) raw data, and Monte Carlo simulations for b) $\eta \to \pi^0\gamma\gamma$, c) $2\pi^0$ production, and d) $\eta \to 2\gamma$. Also shown are different cuts employed, displayed as straight lines labeled in a) by the numbers 1 through 3. Events above the lines were discarded.

number of $2\pi^0$ events predicted by Monte Carlo simulations is reduced with cut #1 alone by almost a factor of 9, while the number of $\eta \to \pi^0\gamma\gamma$ events is only reduced by just over 10%. Cuts #2 and #3 reduce the number of $2\pi^0$ events as compared with the number of events left after cut #1 by approximately 30% and 60%, respectively.

The $m_{max}\,(\pi^0\gamma)$ cuts also reduced the smaller background from $\eta \to \gamma\gamma$, as do other cuts employed, such as on low energy photons in the CB, as were used in producing Figures 4.7.e and 4.8.e.

The simulation of the $\eta \to 3\pi^0$ process matched that seen in the data, as examined in Appendix D. The $\gamma p \to \eta p \to 3\pi^0 p \to 6\gamma p$ process is the worst background because it can produce a peak that mimics the $\eta \to \pi^0\gamma\gamma$ peak. It does this when two pairs of photons from two of the π^0 decays overlap, which results in 4 photon clusters, two of which add up to make a π^0, and all four sum to the η mass. The branching ratio for $\eta \to 3\pi^0$ is approximately 1000 times greater than for $\eta \to \pi^0\gamma\gamma$. The detection efficiency for misidentifying $\eta \to 3\pi^0$events as possible $\eta \to \pi^0\gamma\gamma$ candidates was found to be slightly greater than 0.1%, while for $\eta \to \pi^0\gamma\gamma$ events it was approximately 15%, with no cuts on the background. This means that for a certain number of η's produced, the number of $\eta \to 3\pi^0$ events misidentified as $\eta \to \pi^0\gamma\gamma$ events would be around a factor of 7 greater than the actual $\eta \to \pi^0\gamma\gamma$ signal.

In order to suppress the $\eta \to 3\pi^0$ background, cuts on the cluster effective radius, R, were employed, as done by Prakhov [17]. The idea behind the effective radius is that clusters which in actuality are two overlapping photons will have a larger part of their energy deposited further from the cluster center as compared with typical,

single photon clusters. The formula used for the calculations of R is given in [17] by

$$R = \sqrt{\frac{\Sigma_i^N E_i (\Delta\theta_i)^2}{\Sigma_i^N E_i}} \tag{4.13}$$

where E_i is the energy deposited in each of the N crystal in a cluster and $\Delta\theta_i$ is the difference in angle between the crystal axis and the cluster direction. Plots of R versus cluster energy for the photons not associated with the π^0, the "bachelor" photons, can be seen in Figure 4.6, along with an example of the cuts on R versus cluster energy that were employed. The cuts were made in such a way that all events above the cut line were rejected. The effects of the R cut #2 depicted in Figure 4.6 on the invariant mass distribution of $\eta \to \pi^0\gamma\gamma$ candidates can be seen in Figures 4.8 and 4.9 for data and Monte Carlo simulations of the background processes and $\eta \to \pi^0\gamma\gamma$. With R cut #1, the ratio of expected $\eta \to 3\pi^0$ background to actual $\eta \to \pi^0\gamma\gamma$ events is reduced from about 7 to about 2.5. Cuts #2 and #3 reduce this ratio further to approximately 2.0 and 1.5, respectively.

4.6 Determination of $\eta \to \pi^0\gamma\gamma$ Branching Ratio

After the suppression of the $2\pi^0$, $\eta \to \gamma\gamma$ and $\eta \to 3\pi^0$ backgrounds, there is still some contribution from these sources in the invariant mass spectra of the 4 photons of event candidates.

The next step was then to subtract the expected $3\pi^0$ contribution that remained, as found in Monte Carlo simulations, from the data. The weight factor for the $3\pi^0$

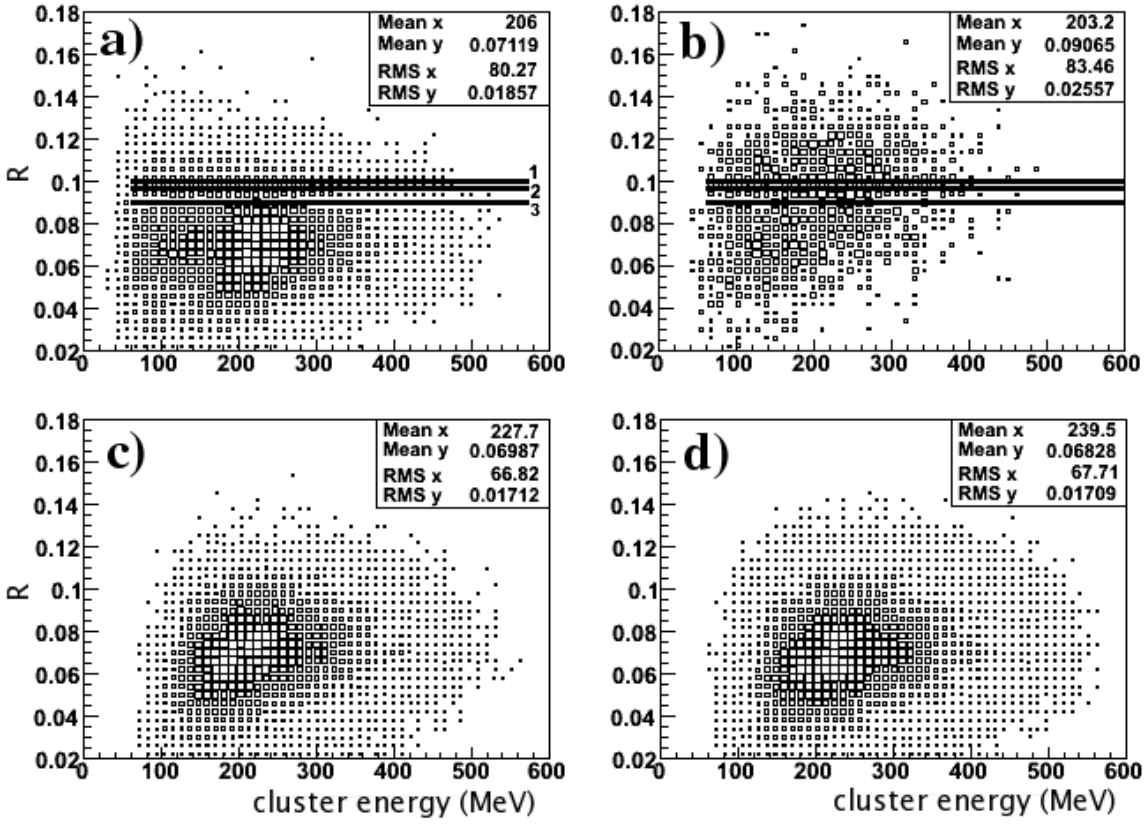

Figure 4.6: Plots of the density distribution of R versus cluster energy for events already passing the kinematic tests from Monte Carlo simulations for a) $\eta \to \pi^0\gamma\gamma$ an b) $\eta \to 3\pi^0$. Different severity's of the cut are labeled in a) as 1, 2, and 3. Figures c) and d) are for photons events selected as $\eta \to 2\pi^0$ for data and Monte Carlo, respectively, illustrating the good agreement between data and Monte Carlo for the R variable.

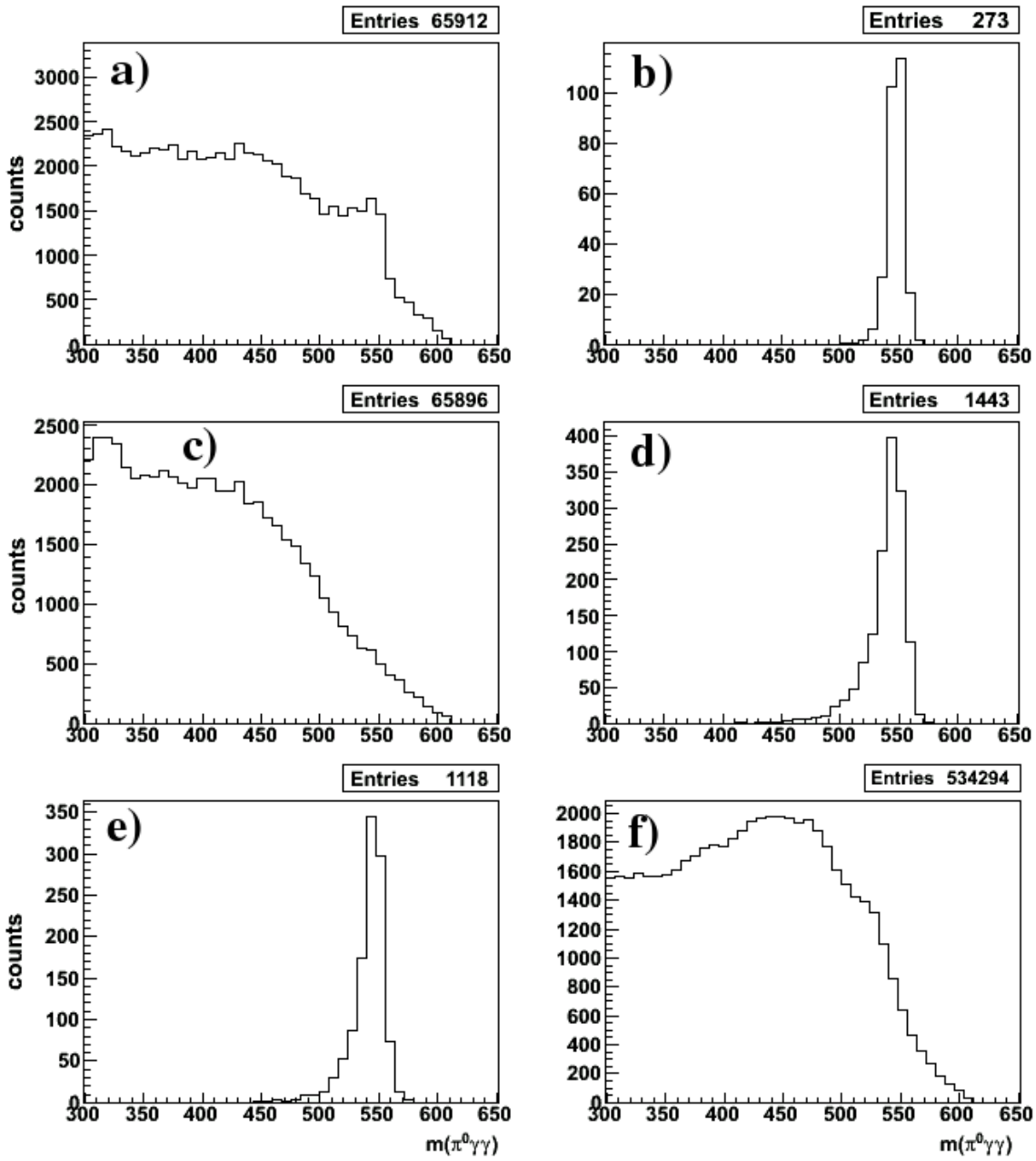

Figure 4.7: The invariant mass spectrum of $\pi^0\gamma\gamma$ candidates prior to any cuts on $m\,(\pi^0\gamma\gamma)$ versus $m_{max}\,(\pi^0\gamma)$ or the R value for a) raw data (the random contributions subtracted from the prompt contributions) and Monte Carlo simulations of contributions from b) $\eta \rightarrow \pi^0\gamma\gamma$, c) $2\pi^0$production, d) $\eta \rightarrow 3\pi^0$ and e) $\eta \rightarrow \gamma\gamma$. Figure f) shows the random events that were subtracted from the prompt, resulting in what is seen in Figure a). The number of random entries is the actual number of events, but the histogram has pictured has been scaled by the ratio of the width of prompt to random time window widths.

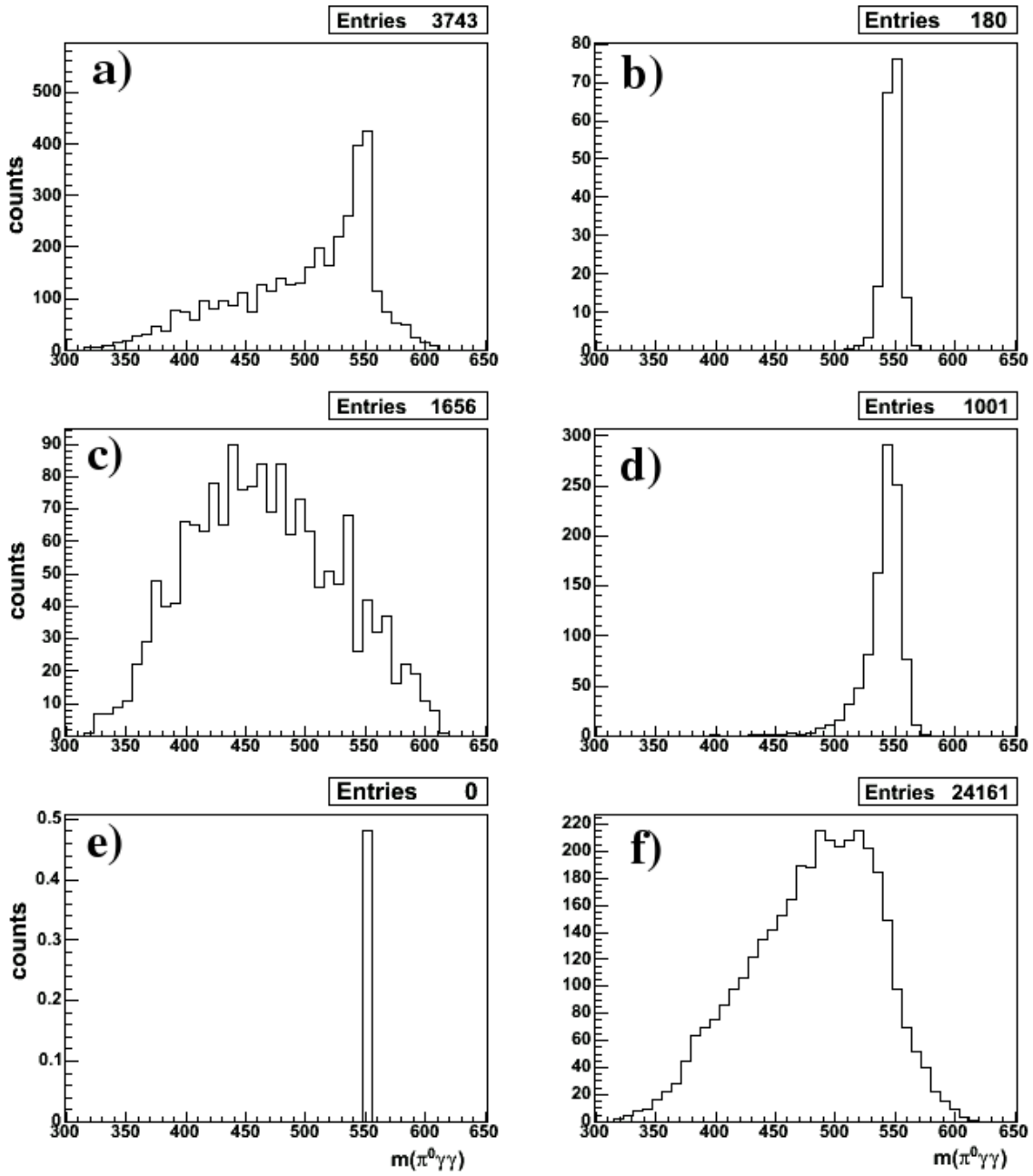

Figure 4.8: The same invariant mass distributions as in Figure 4.7, after applying the rejection of events above the $m_{max}\,(\pi^0\gamma)$ cut #2 line depicted in Figure 4.5, as well as some low energy cuts on photons in the CB.

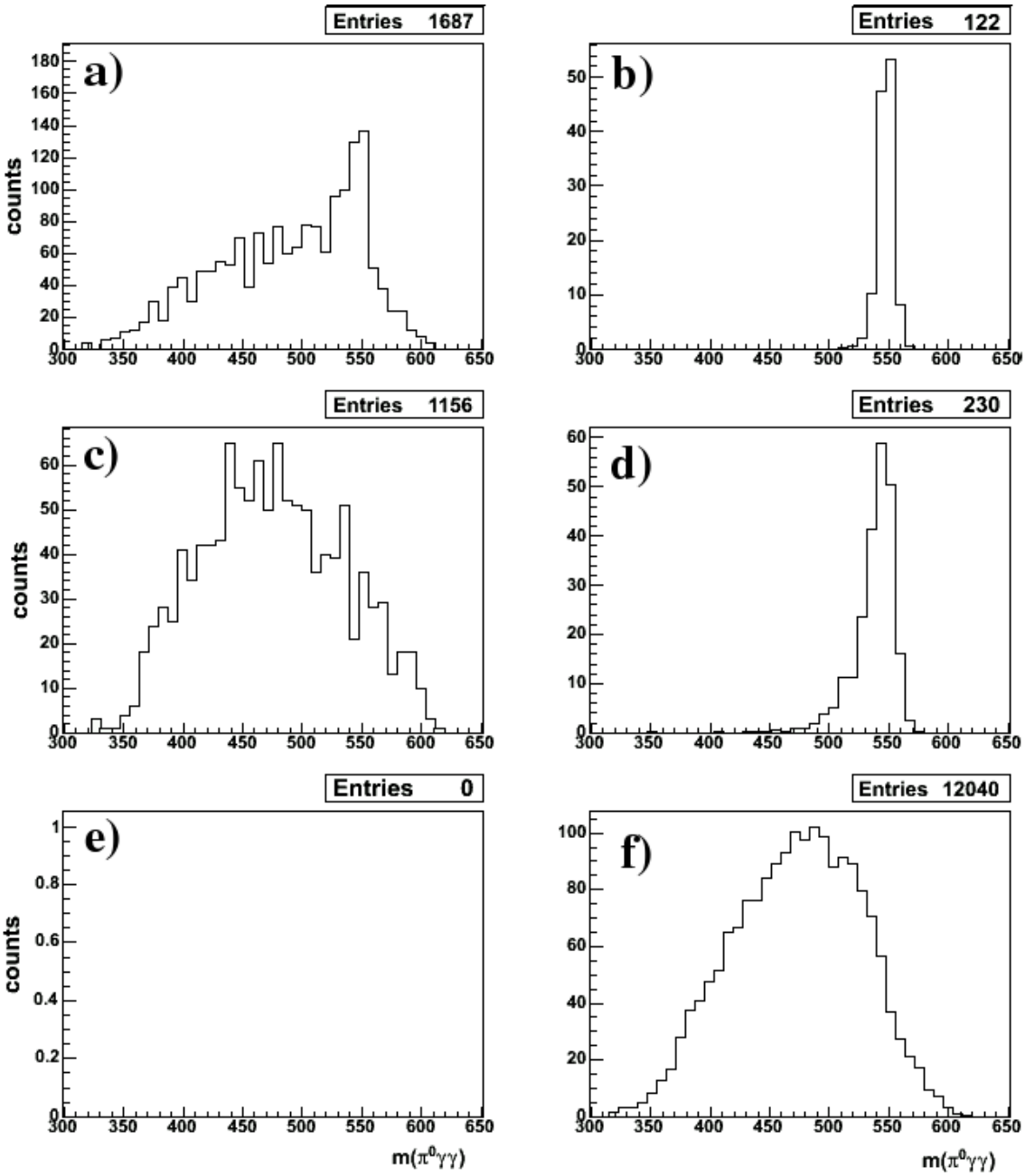

Figure 4.9: Same as in Figure 4.7, after applying the rejection of events above the $m_{max}\,(\pi^0\gamma)$ cut #2 line depicted in Figure 4.5 and events with values of R above the cut #2 line depicted in Figure 4.6.

contribution was based on the number of $\eta \to 3\pi^0$ events detected in the data to that found in the Monte Carlo simulations. The weight factor for the corresponding contribution from $\eta \to \gamma\gamma$ was based on the total number of η's produced as calculated from the number of $\eta \to 3\pi^0$ data and Monte Carlo events. The expected contribution from $\eta \to \gamma\gamma$ was quite small after $m_{max}\,(\pi^0\gamma)$ cut #2 and R cut #2, less than 1 event, compared to the 230 from $\eta \to 3\pi^0$. The result of the subtraction of these contributions can be seen in Figure 4.10, where a large portion of the peak in the η region was already reduced due to the earlier cut on R, and is reduced further by the $3\pi^0$ subtraction.

Ideally, what is left of the simulated $2\pi^0$ background could then be subtracted from the data, however this cannot be done as this background is not fully understood, and therefore the exact amount which is expected to contribute is not known. To deal with this, assuming that what is left in the invariant mass spectrum is the $2\pi^0$ background and $\eta \to \pi^0\gamma\gamma$ peak, take a sum of the simulation of these two processes and fit them to the invariant mass distribution. Unfortunately, again due to the lack of precise enough knowledge of the $2\pi^0$ background, this was not possible to do as the simulated background did not match the experimentally observed background well enough (see Figure 4.11).

Even though the simulated $2\pi^0$ background did match the observed background, by fitting the peak with one function along with another function to the background, one can make an estimate of the number in the $\eta \to \pi^0\gamma\gamma$ peak, thereby estimating the branching ratio. A fifth order polynomial was used to fit the background. The simulated $\eta \to \pi^0\gamma\gamma$ peak was fit with a Gaussian. The peak center and width

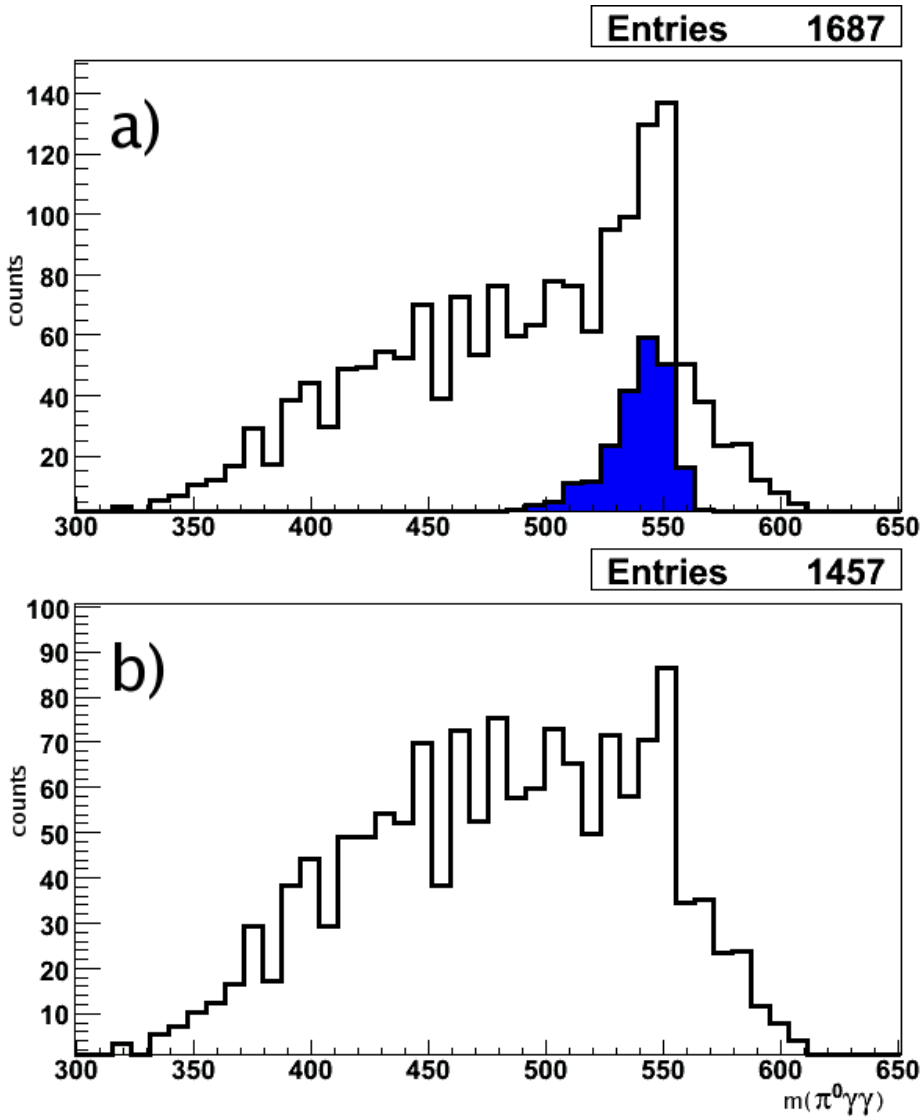

Figure 4.10: The a) invariant mass of 4 photons from event candidates after the suppression of the $2\pi^0$, $\eta \to \gamma\gamma$, and $\eta \to 3\pi^0$ backgrounds, $m_{max}\,(\pi^0\gamma)$ cut #2 and R cut #2, along with the expected $3\pi^0$ background (shaded peak). b) The invariant mass after the subtraction of the $3\pi^0$ background.

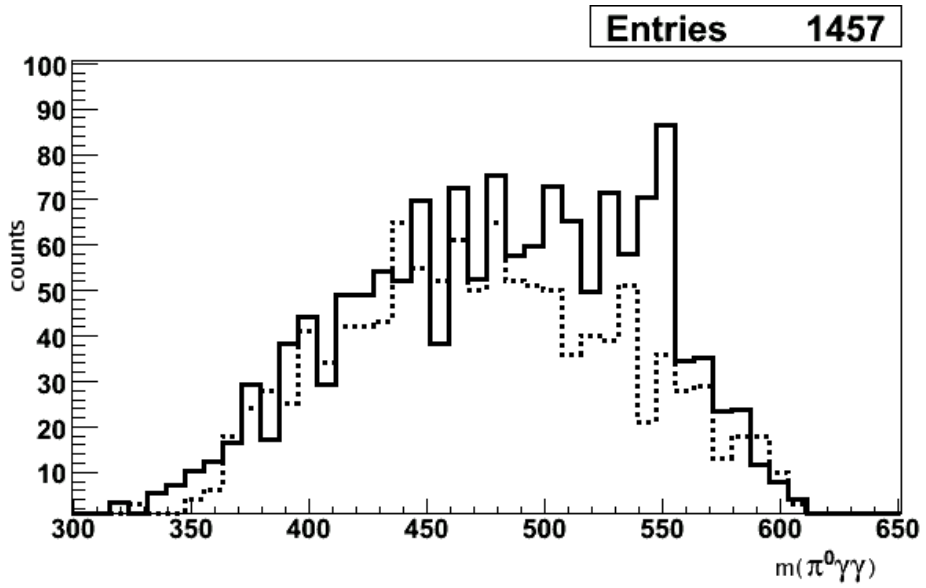

Figure 4.11: The solid line is the invariant mass of the actual data, the dashed line is the simulated $2\pi^0$ background, scaled here to match the background in the data. It can be seen that the data simulation does not match the background seen in the data very well in the region of the η mass.

obtained from this fit were then used as fixed parameters in the fit of the data peak, where the free parameters were the amplitude of the Gaussian, as well as the six components of the fifth order polynomial. An example of this fit to the data can be seen in Figure 4.12. The errors in the number of events as found from the fit of the peak were obtained from the MINUIT package of the CERN program library.

The branching ratio is then calculated from the number of events found in the fit peak, $N_{\eta\to\pi^0\gamma\gamma,peak}$, by

$$BR\left(\eta\to\pi^0\gamma\gamma\right)=\frac{N_{\eta\to\pi^0\gamma\gamma,peak}}{N_{\eta,total}\epsilon_{\eta\to\pi^0\gamma\gamma}} \tag{4.14}$$

where $N_{\eta,total}$ is the total number of η's produced and $\epsilon_{\eta\to\pi^0\gamma\gamma}$ is the efficiency of the detection of $\eta\to\pi^0\gamma\gamma$ Monte Carlo. The error in the branching ratio is then the

quadrature sum of the errors of $N_{\eta,total}$, $N_{\eta\to\pi^0\gamma\gamma,peak}$, and $\epsilon_{\eta\to\pi^0\gamma\gamma}$.

Table 4.1 shows different values of BR($\eta \to \pi^0\gamma\gamma$) as calculated with different combinations of cuts on the confidence level (CL), the effective radius (R cut), and the value of $m_{max}\,(\pi^0\gamma)$ versus $m\,(\pi^0\gamma\gamma)$ ($m_{max}\,(\pi^0\gamma)$ cut). The invariant mass distribution corresponding to the entry for $m_{max}\,(\pi^0\gamma)$ cut #2 and R cut #2 in Table 4.1 is plotted in 4.12.a, along with the fits of the background and peak functions. Also shown in 4.12.b is the same data, but events where the invariant mass of the two "bachelor" photons, $m_{bach}(\gamma\gamma)$, was below that of the π^0 mass were rejected. This cut results in around 30% reduction in the $2\pi^0$ background, but may reject some actual events, as different theoretical models predict different contributions to the number of $\pi^0\gamma\gamma$ events from $m_{bach}(\gamma\gamma)$ below the π^0 mass. Some values of BR($\eta \to \pi^0\gamma\gamma$) using this cut appear in the last three entries of Table 4.1. Searches for events corresponding to $m_{bach}(\gamma\gamma)$ below $m(\pi^0)$ did not yield any events.

A final evaluation of the branching ratio was made from an average of the values presented in 4.1, except for the last three entries, of

$$BR(\eta \to \pi^0\gamma\gamma) = (2.0 \pm 0.7_{sta} \pm 0.2_{sys}) \times 10^{-4} \tag{4.15}$$

where the error includes both the statistical and systematic uncertainties. The statistical error comes from the fitting of the $\eta \to \pi^0\gamma\gamma$ peak, which also includes the uncertainty in the overall number of η's, and the weights used for the $3\pi^0$ and $\gamma\gamma$ backgrounds. The systematic error is the standard deviation of determinations of the

CL	R cut	$m_{max}\,(\pi^0\gamma)$ cut	# of $\eta \to \pi^0\gamma\gamma$ events	$BR\,(\eta \to \pi^0\gamma\gamma)[\times 10^{-4}]$
10%	#1	#1	81 ± 33	1.69 ± 0.71
10%	#1	#2	86 ± 31	1.95 ± 0.69
10%	#1	#3	78 ± 26	1.96 ± 0.67
10%	#2	#1	93 ± 26	2.43 ± 0.67
10%	#2	#2	83 ± 24	2.33 ± 0.67
10%	#2	#3	75 ± 22	2.35 ± 0.68
10%	#3	#1	71 ± 23	2.03 ± 0.66
10%	#3	#2	68 ± 21	2.11 ± 0.65
10%	#3	#3	63 ± 21	2.18 ± 0.72
15%	#1	#1	72 ± 27	1.63 ± 0.61
15%	#1	#2	76 ± 25	1.85 ± 0.62
15%	#1	#3	70 ± 23	1.90 ± 0.62
15%	#2	#1	70 ± 24	1.95 ± 0.66
15%	#2	#2	71 ± 22	2.14 ± 0.67
15%	#2	#3	62 ± 21	2.08 ± 0.72
15%	#3	#1	59 ± 21	1.79 ± 0.64
15%	#3	#2	57 ± 20	1.90 ± 0.64
15%	#3	#3	60 ± 19	2.19 ± 0.70
* 10%	#1	#2	79 ± 21	2.35 ± 0.63
* 10%	#2	#2	82 ± 23	2.30 ± 0.64
* 10%	#3	#2	63 ± 19	2.05 ± 0.61

Table 4.1: Evaluations of $BR\,(\eta \to \pi^0\gamma\gamma)$ for different cuts on the confidence level (CL), the effective radius (R cut), and the cut based on $m_{max}\,(\pi^0\gamma)$ versus $m\,(\pi^0\gamma\gamma)$ ($m_{max}\,(\pi^0\gamma)$ cut) for 5 cluster events. The number of the cuts refers to the labels in Figures 4.5 and 4.6. The last three entries in the table are for events where $m_{bach}(\gamma\gamma)$ was above $m(\pi^0)$, as described in the text. Also shown are the number of $\eta \to \pi^0\gamma\gamma$ events as obtained from a fit of the data.

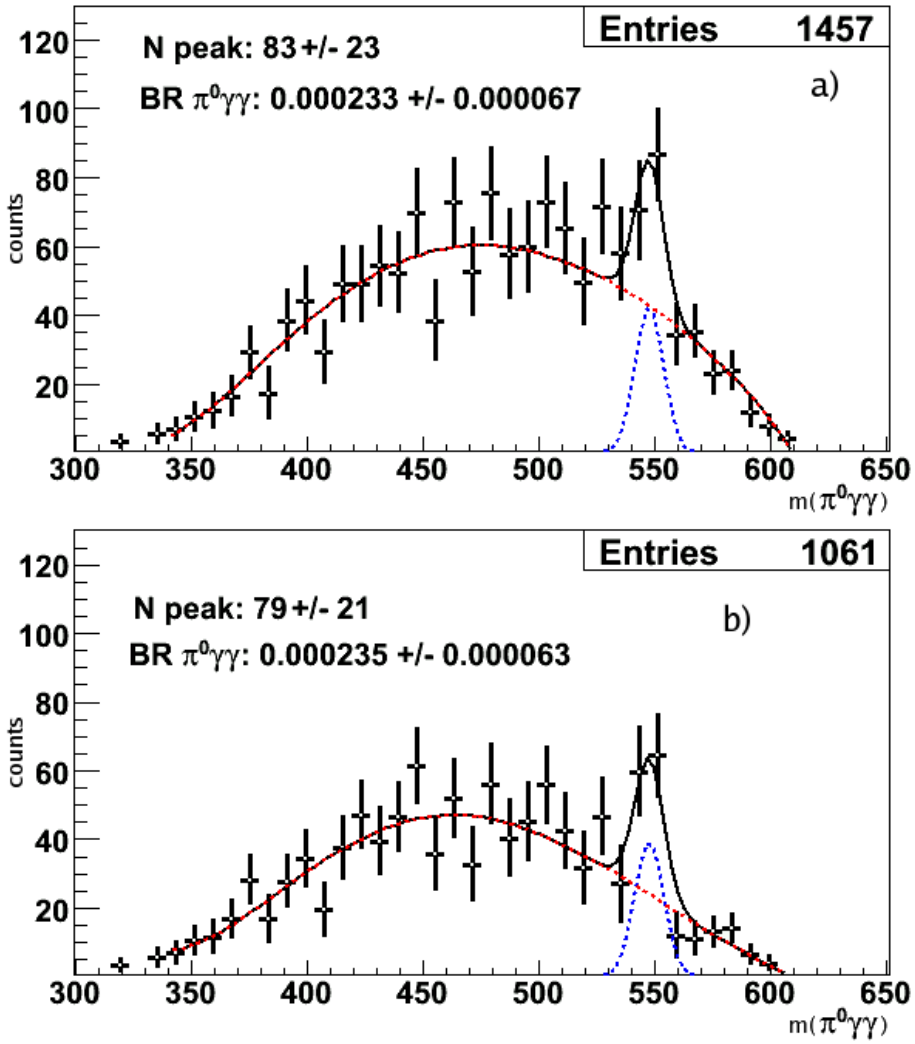

Figure 4.12: Fit of the background with a fifth order polynomial and the peak for all events in a) with a Gaussian results in a total of 83 $\eta \to \pi^0\gamma\gamma$ events and BR($\eta \to \pi^0\gamma\gamma$) = $(2.33 \pm 0.67) \times 10^{-4}$. The solid line is the total function, the upper dashed line is the background, the lower dashed line is the Gaussian fit of the peak. Figure b) shows the same data, but with the cut on the "bachelor" photon invariant mass, as described in the text.

branching ratio due to different selection choices.

In order to compare this result with theoretical calculations, the decay rate needs to be calculated. Using the PDG [18] value of $\Gamma(\eta \to all) = 1.30 \pm 0.07$ keV, the decay width, with errors summed in quadrature is

$$\Gamma\left(\eta \to \pi^0\gamma\gamma\right) = 0.26 \pm 0.10 \text{ eV}. \tag{4.16}$$

This value is lower than several of the theoretical predictions presented in Table 1.1, though consistent within 2 standard deviations of most, and is close to the chiral perturbation calculations based on VMD models. However, the statistics here are not precise enough to choose among the different predictions. Comparing to other experimental results, the BR($\eta \to \pi^0\gamma\gamma$) found here is 1.6 ± 0.8 times smaller than the most recent result in Table 1.2 from the CB @ AGS experiment [17]; they are within one standard deviation of each other. Our result is 3.2 ± 1.4 times smaller that found by the GAMS-2000 group [6], with the two differing by 2.7 standard deviations. The combination of the result of this thesis and the CB @ AGS result places strong doubt on the validity of the GAMS-2000 result. The statistics here are lower than those in the determination of the branching ratio from the CB @ AGS experiment [17], but has better handling of the background.

Appendix A

Gain matching of crystals in the CB

If each crystal of the Crystal Ball were to detect monochromatic particles, the light output of each PMT would be slightly different. The goal of gain matching was to measure the output of each crystal with its PMT and PMT base for the same energy photon, then adjust the high voltage potentiometer on each PMT so that the gains of all the crystals were closely matched. This task was done by Marc Unverzagt[1], Jason Brudvik[2] and Aleksandr Starostin[3].

A.1 The $^{60}_{27}$Co source

Our fist attempt at making this gain matching was with a $^{60}_{27}$Co source. $^{60}_{27}$Co decays to $^{60}_{28}$Ni, 99.85% of the time under release of an electron with an energy of 0.314 MeV and two photons with energies that are quite close, 1.173 MeV and 1.333 MeV (see

[1] Johannes Gutenberg-Universität Mainz, Germany
[2] UCLA
[3] UCLA

Figure A.1). The time between the emission of each photon is very short, so short that it appears that they arrive at the same time. The remaining 0.15% of the time, $^{60}_{27}$Co decays into one electron with an energy of 1.480 MeV and one photon with an energy of 1.333 MeV.

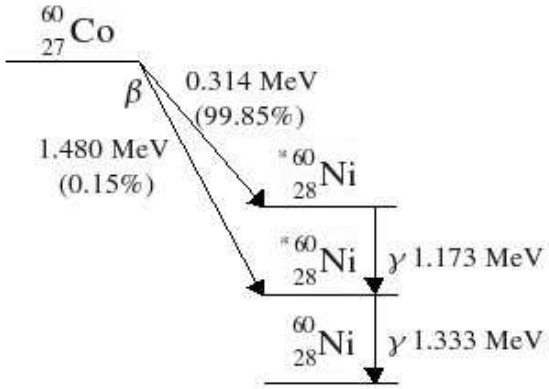

Figure A.1: $^{60}_{27}$Co decay into $^{60}_{28}$Ni

The ADC energy resolution available with the CB at typical experimental settings is approximately 0.6 MeV, so the two peaks that are actually made by the two photons will be seen as one, with a peak somewhere between the two energies. There is also a third peak that is present when both of the photons happen to enter the the same crystal, then the sum of their energy would be detected (see Figure A.2). This is unlikely with the CB, as each crystal covers about 0.14% of 4π steradians, the chance for both photons to go into one crystal is approximately 1.4×10^{-3}.

We placed the source in the center of the CB, made a trigger that consisted of groups of 16 crystals, and set the threshold at approximately 0.6 MeV. If one of the

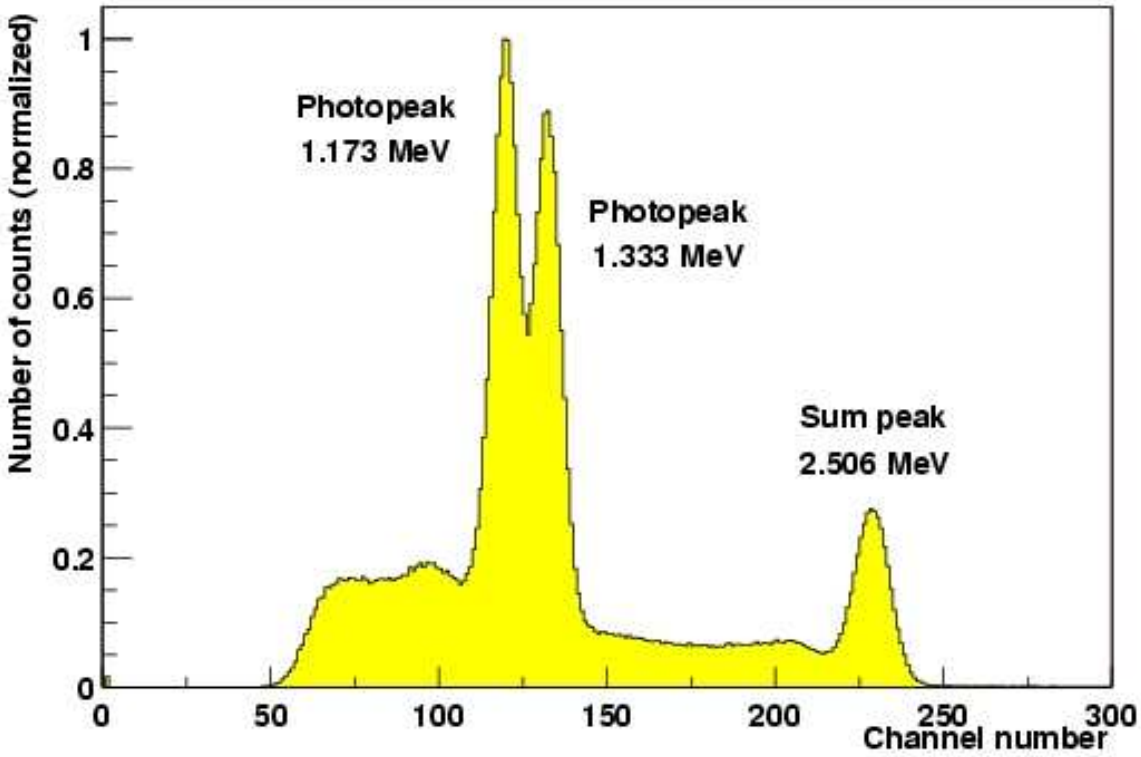

Figure A.2: $^{60}_{27}$Co decay spectrum recorded with a high resolution NaI detector [25].

16 crystals received a signal above the threshold, then all readings of each crystal in the group of 16 were recorded. Of course, doing this results in a lot of unwanted noise also being recorded, and a cleaner result could be obtained by using just one crystal in the trigger at a time. However, we decided that using 16 crystals at a time was reasonable, both in terms of the signals seen and the amount of time that it took to take all the necessary data. We took some data runs with and without the source present, and were satisfied that we really were seeing the photons from the $^{60}_{27}$Co decay (see Figure A.3).

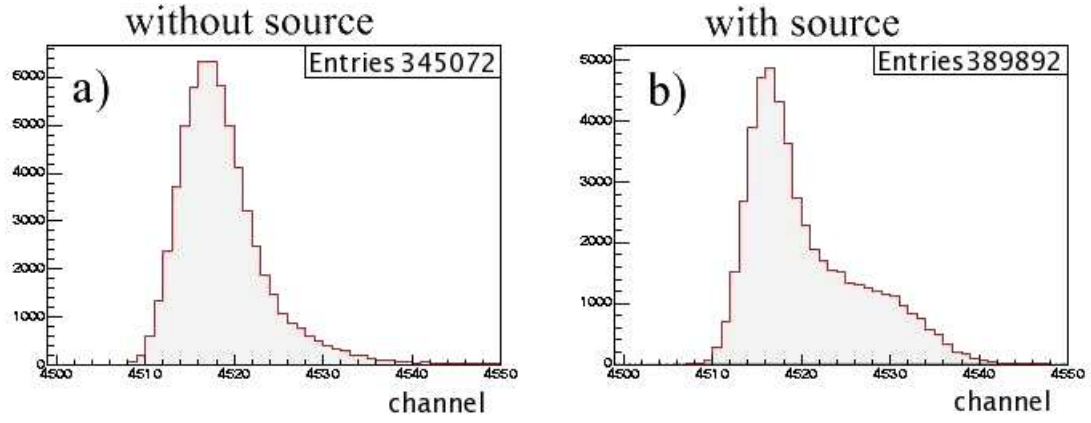

Figure A.3: Spectra seen a) without and b) with the $^{60}_{27}$Co source, over the same lengths of time.

Once we had histograms similar to those in figure A.3 for each crystal, we used ROOT[4] to fit the sum of a Gaussian and an exponential to the portion of the signal where we believed the cobalt signal to be, and thereby locate the signal produced by the photons from the cobalt decay (see Figure A.4).

We then measured the distance between the pedestal peak location and the cobalt signal location for each crystal. The overall distribution of this can be seen in Figure A.5.

One major problem with this calibration was that though it was possible to distinguish the $^{60}_{27}$Co peak from the background for the majority of the crystals, for a large number of them, around 96, this could not be done, therefore the PMTs for these crystals could not be adjusted. The reason for this is that the photons released in the $^{60}_{27}$Co decay have energy just above the background noise, and some crystals

[4]The CERN produced C++ based suite of software tools and libraries.

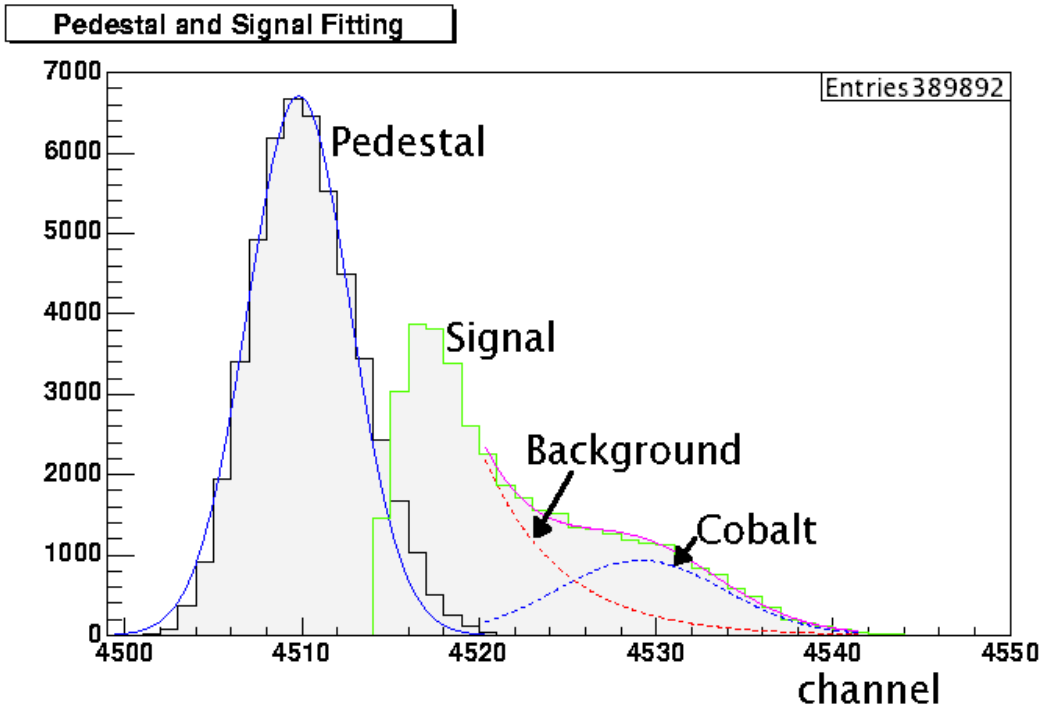

Figure A.4: Example of fitting with a sum of a Gaussian and an exponential to the signal peak.

had a poorer energy resolution than others, so poor that the signal and background could not be separated. So it was decided to try a source with higher energy decay products, namely ^{241}Am/^{9}Be.

A.2 The ^{241}Am/^{9}Be source

Americium beryllium produces neutrons ranging in energy from zero to 10 MeV, and photons, one of which is at 4.438 MeV (see Figure A.7) that was the photon we used for this gain matching work. The process of the production of this particular photon begins with ^{241}Am, which has a half life of 430 years, decaying into ^{237}Np and an α

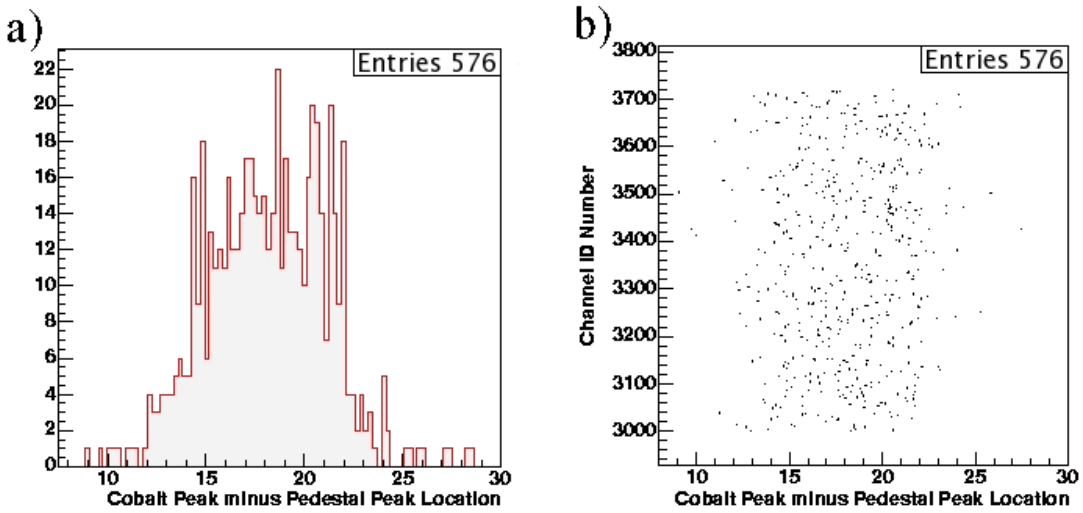

Figure A.5: Overall distribution of the difference between the cobalt peak and pedestal peak using the $^{60}_{27}$Co source (as illustrated in Figure A.4), for a) all channels and b) channel number versus cobalt peak minus pedestal peak.

particle,

$$^{241}_{95}\mathrm{Am} \rightarrow {}^{237}\mathrm{Np} + \alpha \tag{A.1}$$

which is captured by the beryllium. Upon capturing the α, the beryllium becomes an excited isotope of carbon, ^{*13}C, which decays in three possible ways,

$$\alpha + {}^{9}\mathrm{Be} \rightarrow {}^{*13}\mathrm{C} \rightarrow \left\{ \begin{array}{r} {}^{*12}\mathrm{C} + n \\ {}^{8}\mathrm{Be} + \alpha + n \\ 3\alpha + n \end{array} \right\} \tag{A.2}$$

the one which we were interested in is an excited carbon state plus a neutron, which then decays to its ground state, in doing so releases the 4.438 MeV photon.

$$^{*12}\mathrm{C} \rightarrow {}^{12}\mathrm{C} + \gamma \tag{A.3}$$

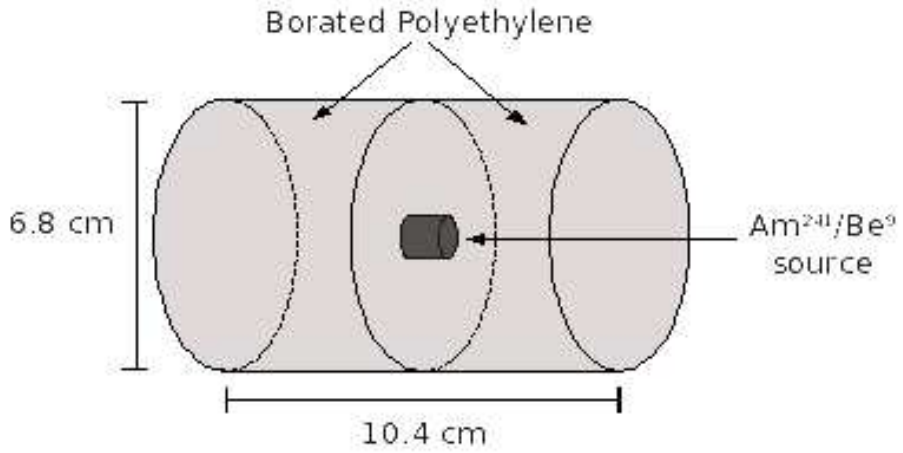

Figure A.6: Two pieces of Borated Polyethylene were used to surround the ^{241}Am/^{9}Be source.

The procedure for locating the photon peak for each crystal was the same as that when $^{60}_{27}$Co was used as the source, with a few modifications.

One modification that we had to do was to place the ^{241}Am/^{9}Be source in a container made of borated polyethylene (see Figure A.6) in order to capture the neutrons that were emitted and thereby cut down on unwanted contributions from other background processes, as depicted in Figure A.7. Another modification that was made was to set the threshold for accepted events to approximately 2.3 MeV. During the time when these measurements were made, we were also able to make TDC cuts (something we were not ready to do previously during the tests with Cobalt), which cuts down on noise and makes the photon peak that we are interested in much easier to detect (see Figure A.8).

Like the case of the $^{60}_{27}$Co source, the sum of a Gaussian plus an exponential were fit to the region of the spectra believed to contain the photon peak. Due to time constraints, we were not able to look at the entire CB during this time, so we

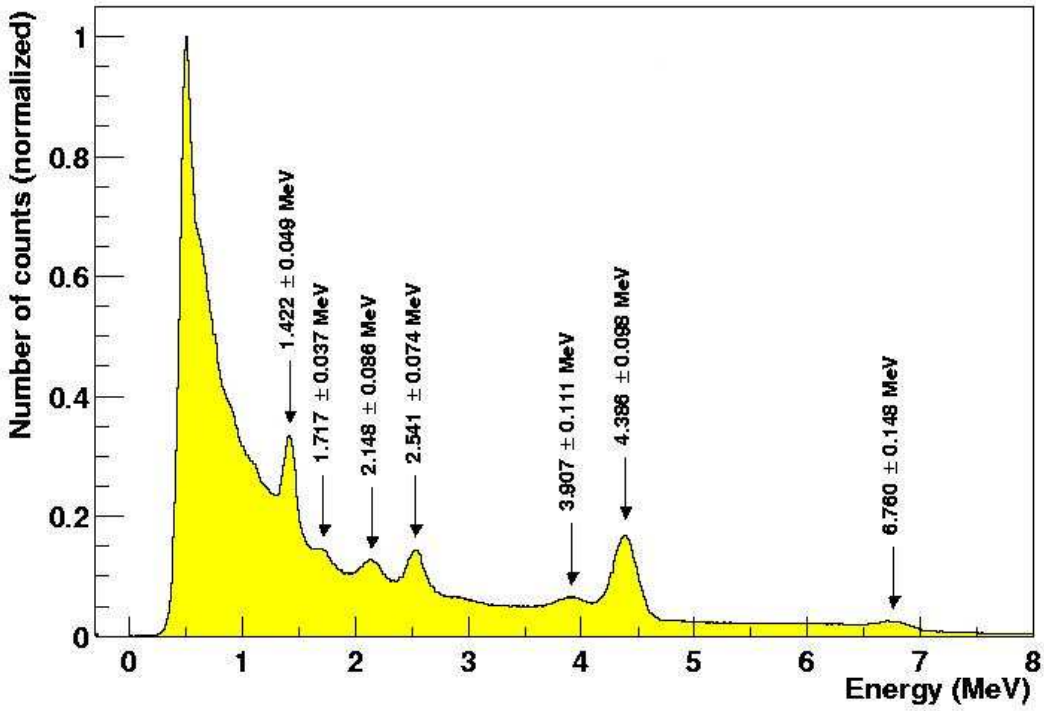

Figure A.7: Photon spectrum of ^{241}Am/^{9}Be decay as measured with a special NaI detector [25].

recorded data for approximately 3/4 of the CB (see Figure A.9).

We then adjusted 105 PMTs which were judged to give readings more than 20% away from the average value. This was done by placing the source in the center of the CB again, then making small adjustments of the potentiometer and seeing the effect on the spectra (see Figure A.10).

After this was done, we took data for the entire CB once again, in the same manner as before, and found that the overall distribution of photon peak locations was narrower (see Figure A.9). Also, the overall fitting process was much better, as there were only 12 crystals for which the peak could not be distinguished from the background noise, 4 that gave no signal due to some unknown problem, likely the

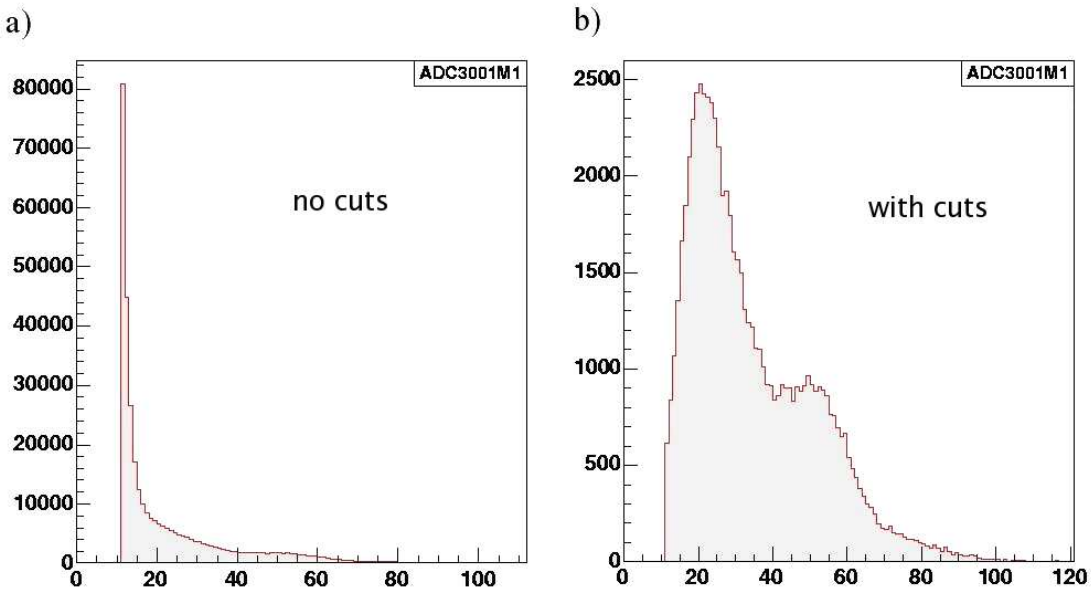

Figure A.8: Photon spectrum of ^{241}Am/^{9}Be source measured by the CB with a) no TDC cut and b) with TDC cut.

PMT, and 3 that were not included because of a ringing discriminator channel.

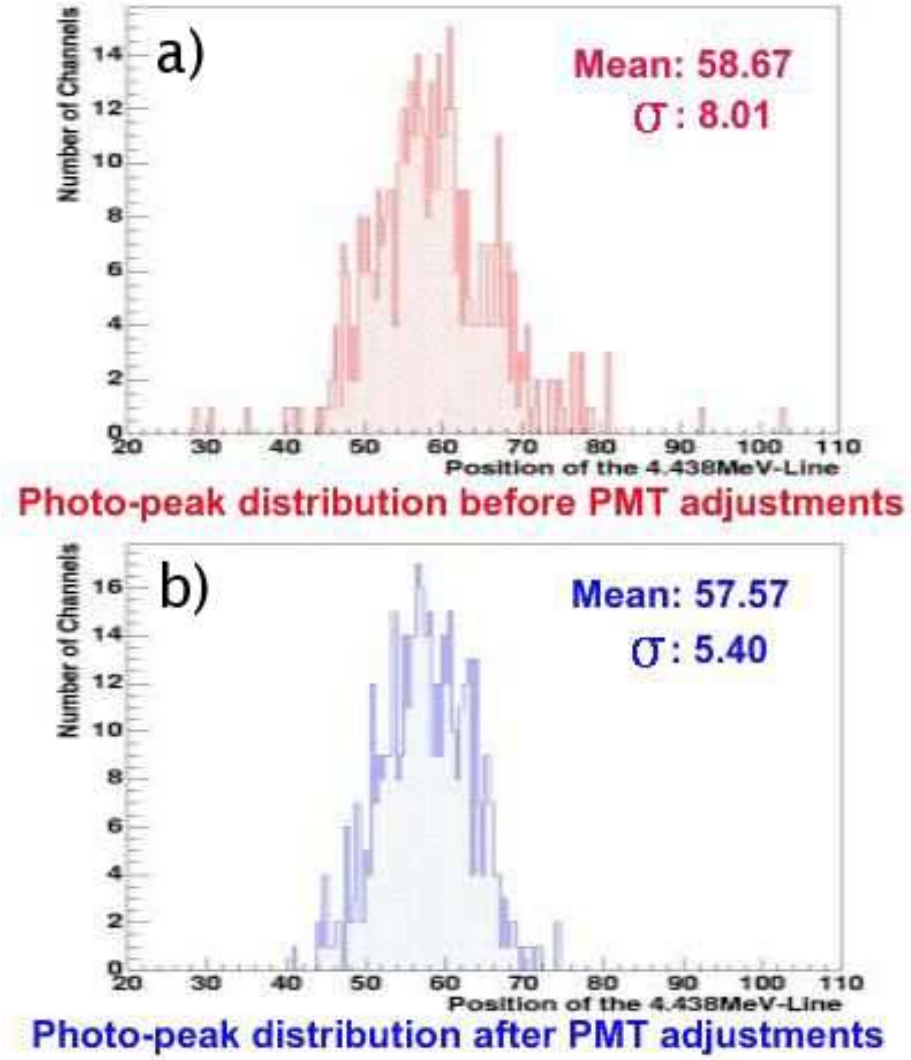

Figure A.9: Distribution of the difference between the signal location and pedestal location using the ^{241}Am/^{9}Be source, a) before and b) after adjustments. These figures contain information on only 437 crystals, as only 3/4 of the CB was looked at before adjustments were made, and for some crystals the 4.438 MeV photon peak could not be found.

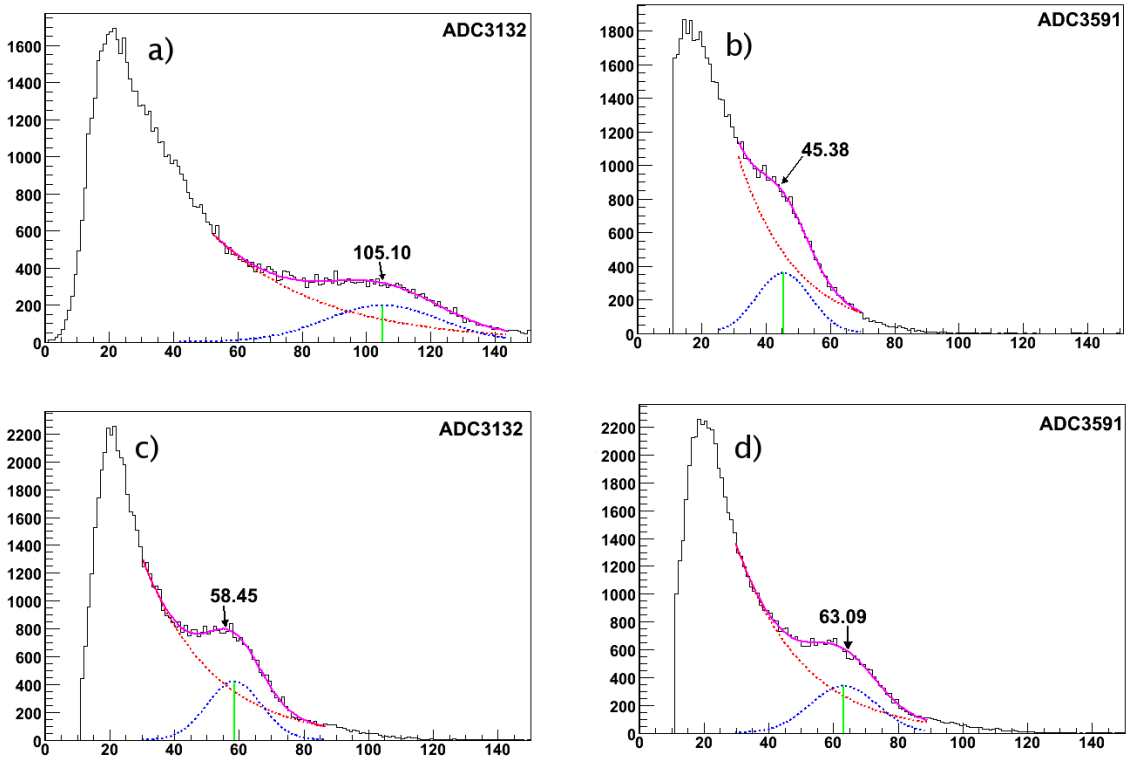

Figure A.10: Photon spectra for two CB crystals. a) and b) before PMT adjustments. c) and d) after PMT adjustments.

Appendix B

Calibration of the CB with $\gamma p \rightarrow \pi^0 p$

The technique of matching the response (see Appendix A) of the PMT's viewing each crystal in the CB is inherently imprecise. After the process of gain matching is completed, a calibration of each element in the Crystal Ball must be done so that the gains may be fine-tuned via software for use during analysis of the data.

B.1 Process Overview

The calibration of the CB was done using the reaction $\gamma p \rightarrow \pi^0 p$, comparing the measured values of the energies of the two photons into which the π^0 decays, with a branching ratio of BR($\pi^0 \rightarrow \gamma\gamma$) = 98.8%, with their expected energies. Usually, the measured and expected values were quite similar, so that only relatively small adjustments of the gains were necessary.

When a photon strikes the CB, not all of it's energy is deposited in one crystal, it is spread over 5 to 13 crystal typically, with the central crystal usually absorbing

more than 50% of the energy. When doing this calibration work, I used events in which 70% of the photon energy was deposited in the central crystal of a cluster. Because of the spreading of a photon's energy among several crystals, when the gain of a channel is altered that is not the central hit in a cluster, it affects the calculated gain of the central crystal, therefore many iterations of the calibration procedure must be preformed in order to reach a steady state where the gain values do not change noticeably from one iteration to the next. For this calibration work, it was found that four iterations sufficed.

The stability of the calibration within and between runs was examined. It was found that calibrations for each of the different experimental runs done with the CB at MAMI was needed, as it was found that gain values could differ by more than 10% between different runs, while they differed by less than 3% within runs.

B.2 Calculation of expected π^0 energy

The expected value of the energy of a π^0 that is detected in the CB can be calculated when one knows the energy of the beam photon incident on the target, the angles of the photon in the CB relative to the target position, and the assumptions that the target has a proton mass and that the particle which decayed into two photons was in fact a π^0. As noted in Chapter 4, the incoming electron energy is very well known, the resulting Bremsstrahlung photon energy is given by equation 2.1. The angular resolution is around 2 to 3 degrees for the CB, as noted in table 2.1. Relativistic

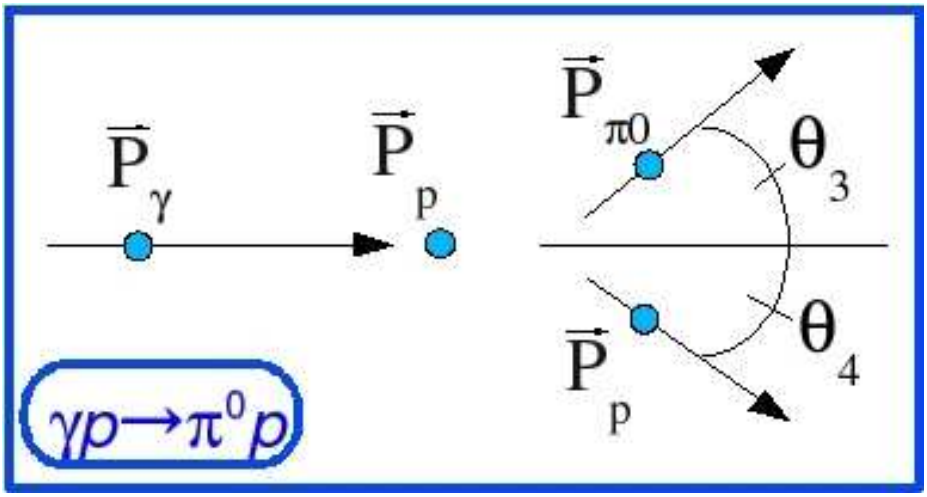

Figure B.1: Kinematics of the $\gamma p \rightarrow \pi^0 p$ interaction.

kinematics relates the π^0 energy to the aforementioned quantities via the equation:

$$2E_\gamma p_{\pi^0} \cos\theta_{\pi^0} = 2E_{\pi^0}(E_\gamma + m_p) - 2E_\gamma m_p - m_{\pi^0}^2 \tag{B.1}$$

where the the subscripts γ, π^0, and p, refer to the incident photon, the π^0 detected, and the proton target, respectively. Solving this equation for E_{π^0} results in two possible solutions, of which the one closest to the measured value was chosen for this calibration process. A diagram of the $\gamma p \rightarrow \pi^0 p$ interaction can be seen in figure B.1. Figure B.2 shows an example of the expected and measured π^0 energies for a run during the September 2004 delta magnetic moment experiment.

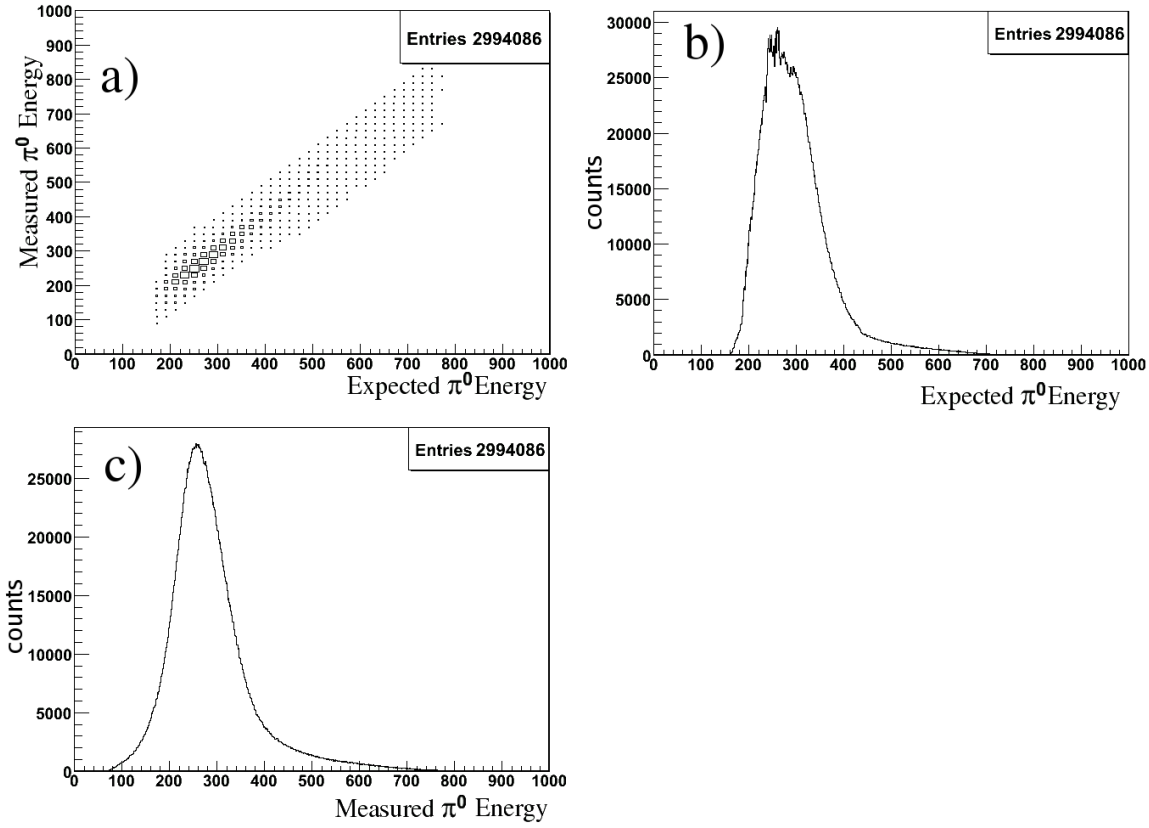

Figure B.2: a) Correlation plot of expected and measured π^0 energies. The b) predicted π^0 energy and c) measured π^0 energy. When the central sections of the histograms in b) and c) are fit with Gaussians, the widths are almost identical, while the centers of the peaks differ by approximately 10 MeV, with the expected distribution being the higher one.

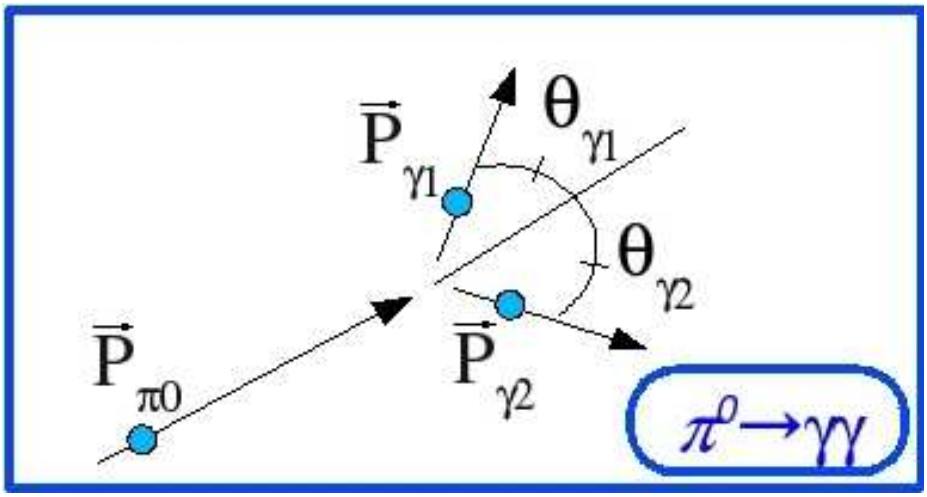

Figure B.3: Kinematics of the π^0 decay into two photons.

B.3 Calculation of expected photon energies

Once the π^0 energy has been obtained, the calculation of the expected value of one of the photon energies, E_γ, can easily be done by transforming from the π^0 center of mass, where both photons have energies equal to half of the π^0 mass, to the laboratory frame of reference:

$$E_\gamma = \frac{E_{\gamma,CM}}{\gamma\left(1 - \beta cos\alpha_\gamma\right)} \tag{B.2}$$

where $E_{\gamma,CM}$ is a photon energy in the π^0 center of mass frame, α_γ is the angle between the π^0 direction and the photon direction, and γ and β are the usual relativistic variables that are associated with the π^0. A diagram of the π^0 decay can be seen in figure B.3, an example of the expected and measured photon energies can be seen in figure B.4.

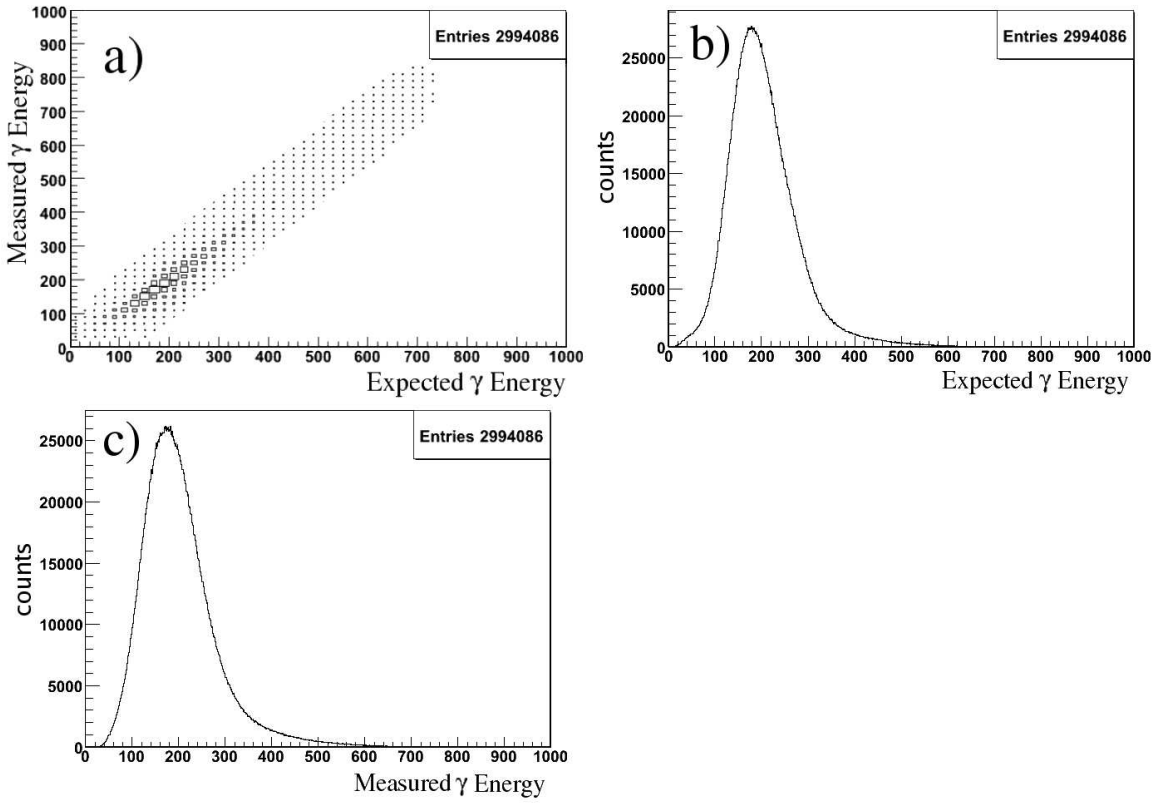

Figure B.4: a) Correlation plot of expected and measured photon energies. The b) measured photon energy and c) predicted predicted energy. When the central sections of the histograms in b) and c) are fit with Gaussians, the widths are almost identical, while the centers of the peaks differ by approximately 2 MeV, with the expected distribution being the higher one.

B.4 Calibration procedure

For doing the actual calibration work, there were several steps which I outline here. The first step was the selection of types of events. They were chosen to be either just two neutral hits in the CB, or two neutral hits plus one charged hit in the CB. The second step was determining whether the particle detected was charged, that determination was made by the PID. For events with three total hits, a cut was also used to minimize the number of cosmic ray events (see Appendix C).

Once events were chosen, cuts were made on the π^0 invariant mass and associated missing mass of 135±50 MeV and 938±100 MeV, respectively (see figure B.5). Then, for clusters that had more than 70% of their energy deposited in the central crystal, a ratio of the expected and measured energies was made for each crystal and, after many events were recorded, Gaussian fits of the distributions were made (see figure B.6). The mean value of the fit for each crystal could then be used to calculate a new gain for the crystal, simply:

$$NewGain = OldGain \cdot Mean \tag{B.3}$$

As previously mentioned, this process was repeated five times, starting with all gains set to an average value, and ending at a point where the variations between iterations of the gains was quite minimal.

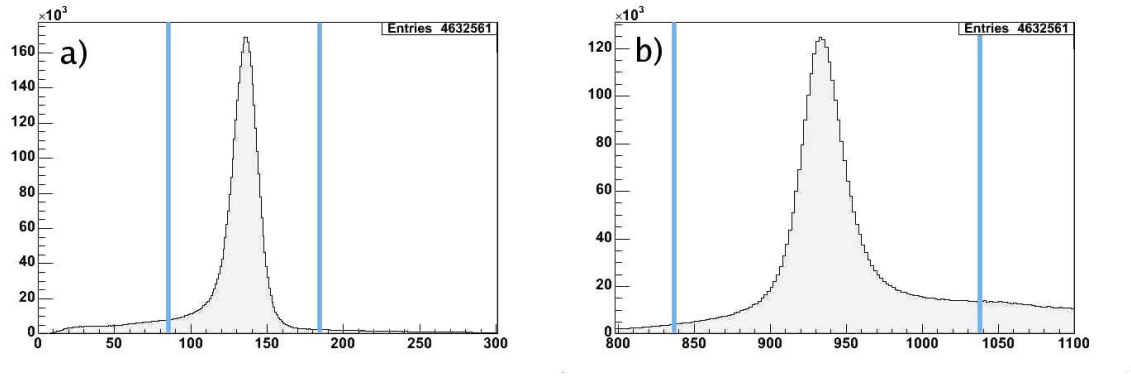

Figure B.5: Cuts made on a) the invariant mass and b) the missing mass of the π^0.

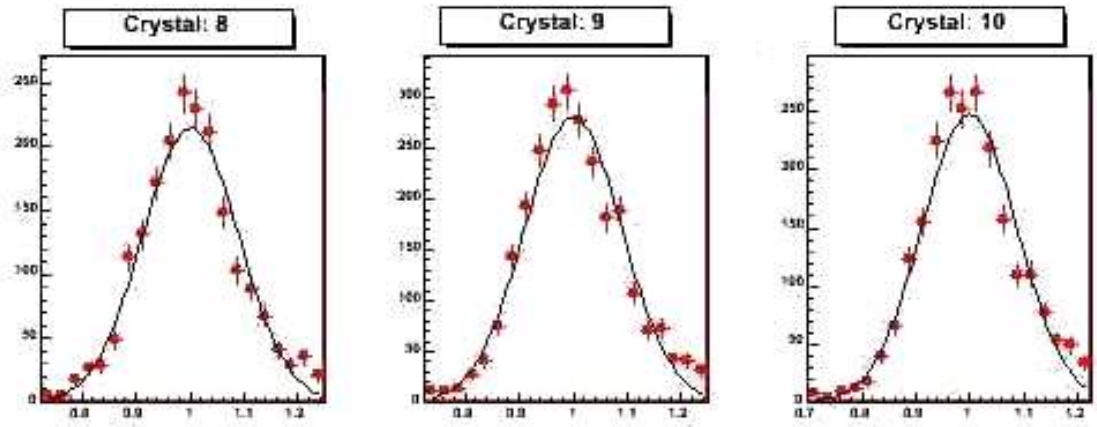

Figure B.6: Three examples of Gaussian fits of the ratio of expected to measured energies in the central crystals of clusters.

Experimental Run	π^0 IM σ(MeV), before	π^0 IM σ(MeV), after
DMM July 2004	8.88	8.29
DMM Sept. 2004	9.02	8.33
Eta Nov. 2004	9.85	8.93
Eta Dec. 2004	9.91	8.87
DMM LP Jan. 2005	9.18	8.39
DMM CP Jan. 2005	9.04	8.20

Table B.1: The width of the π^0 invariant mass using the gains calculated in the summer of 2004, denoted as before, the width using the newly calculated gains, denoted as after.

B.5 Calibration results

One new calibration file was made for each run period that had liquid hydrogen as the target. This included four runs that examined the delta magnetic moment, done in July and September of 2004, two done in January of 2005, and two that looked at rare eta decays done in November and December of 2004. As mentioned earlier, the gains were very stable for different times within one experimental run period, but were noticeably different from one run period to another. Figure B.7 shows an example of the variation for three channels.

A useful test of the calibration procedure was to see if the resolution of the invariant mass of the π^0 improved, where events were chosen as described in the previous section. After completing this process, it was found that the invariant mass width did in fact decrease for each calibration file produced, as expected. Table B.1 contains the width of the π^0 invariant mass using the original gains and the newly calculated gains. Figure B.8 is an example of how the width of the π^0 invariant mass is altered after each iteration in the calibration procedure. The pictures are from data from the delta magnetic moment run in September of 2004. Figure B.9 shows an example of

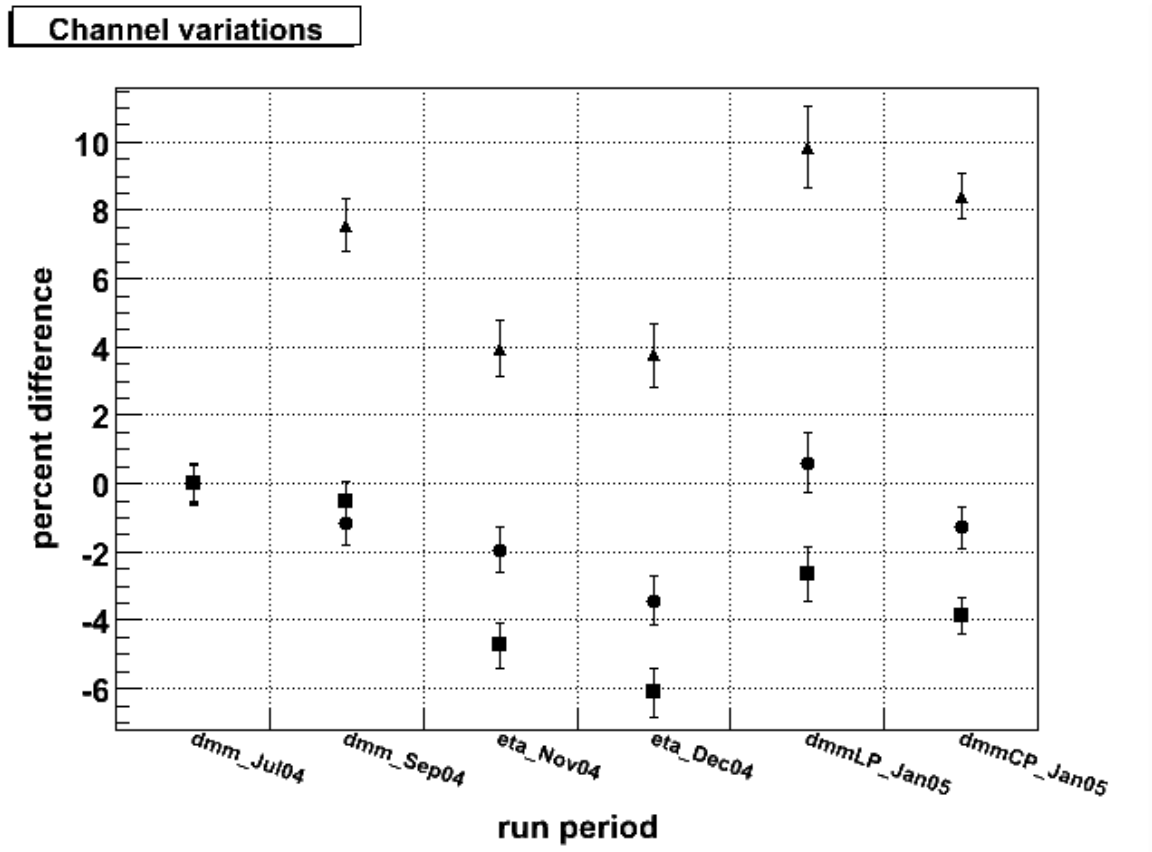

Figure B.7: The percentage difference in the gains calculated for three crystals during different experimental run periods. The errors bars are the accumulation of the errors in the calculation of the gains over each iteration and ultimately depend on the error in fitting a Gaussian to the distribution of calculated to measured energy ratios for each crystal.

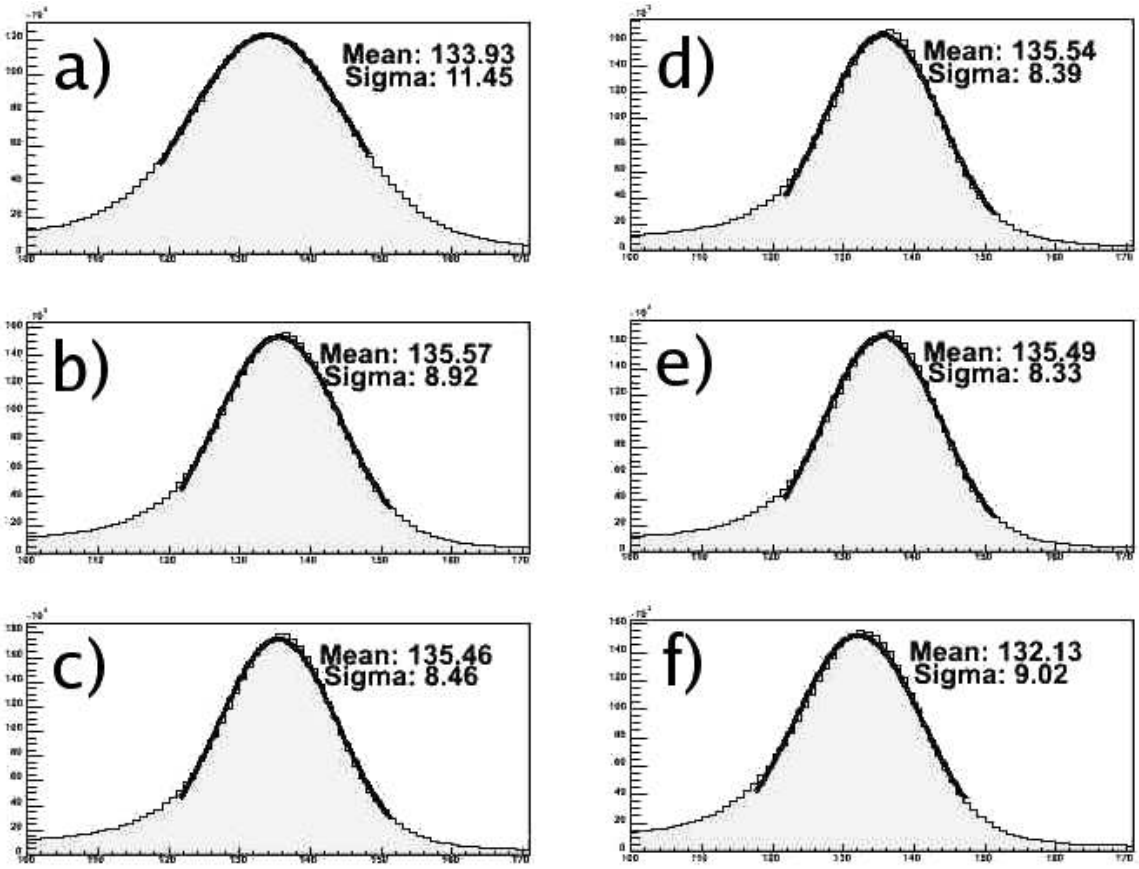

Figure B.8: Example of the change of the invariant mass of the detected π^0 with each iteration. Plot a) is the invariant mass that is produced when the gains for each crystal are set to the same, average value. Plots b) through e) show the invariant mass after successive iterations, with e) being the final iteration. Plot f) is the invariant mass of the π^0 as measured using gains calculated in the summer of 2004. Note the improvement in the sigma of the invariant mass after each iteration and the improvement over using the values that were calculated in 2004.

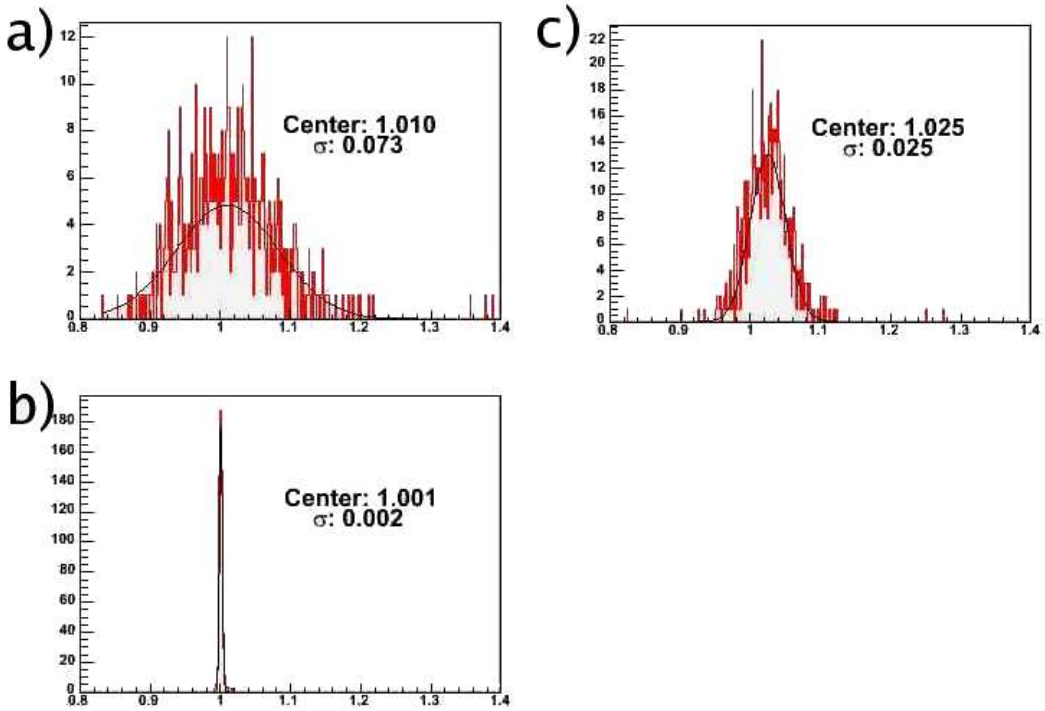

Figure B.9: Histograms containing the value of the mean value of Gaussian fits of the ratio of expected to measured energies for all crystals. Plot a) has all gains set to the same, average value at the beginning of the calibration procedure, plot b) using the gains obtained after the final calibration iteration, and c) using the summer 2004 values.

how the ratio of expected to measured energies changed during the calibration procedures for the same run period. Improvements in the ratio of expected to measured energies and the π^0 invariant mass were quite similar for calibrations done for the other experimental run periods.

Appendix C

Removal of cosmic ray events in the Crystal Ball

A major event type in this experiment were cosmic rays, however when applying the methods of kinematic fitting, cosmic ray events do not contribute at all, but it is still of some interest to recognize such events and discard them if necessary. For events with 4 and 5 clusters in the CB, of primary interest to this experiment, cosmic events made up approximately 15% and 30% of recorded events. Cosmic rays that pass through the CB should follow a straight line, so my first idea for weeding out cosmic ray events was to fit a straight line to the trajectory formed by the hits. The problem is that when a crystal triggers, it is not known where in the crystal the cosmic ray passed when mapping out the hits for an event in three dimensions, all one can do is assign each hit the same distance from the center of the CB. Doing this then results in events that are in reality straight lines being seen as segments of a circle (see Figure C.1).

A circle can be described as the intersection of a plane and a sphere. In this case, the sphere is centered on the CB's center, with a radius equal to the distance from the center to the assigned interaction point of hits in the crystals. For a cosmic ray event in which the hit points form a segment of a circle, this circle has a radius that is the same as the sphere, therefore the plane which intersects the sphere and describes the circle must include the center of the CB. The best segment of a circle that can be used to describe the hits in the CB can be found by determining the plane that best fits the points and includes the CB's center. After the best fit plane is found, then the sum of the shortest distance that each point is from the plane can be determined. For cosmic events this sum should be much smaller than for normal events, which would have a low probability of producing hits that mimic a straight line.

In general, the perpendicular distance , d_j, that a point, $\vec{x_j}$, is from a plane, which is defined by a unit vector normal to it, $\hat{n}$, and a single point, $\vec{x_0}$, is given by:

$$d_j = \hat{n} \cdot (\vec{x_j} - \vec{x_0}) \tag{C.1}$$

The best fit plane to a set of points will be the plane which minimizes the sum of the distances of each point. Since $\vec{d_j}$ can assume negative or positive values, a better quantity to minimize is the sum of the squares of the perpendicular distances that points are from the plane, the process of which is commonly referred to as orthogonal distance regression. In this case the plane must go through the center of the sphere, so $\vec{x_0}$ can be set to zero. Writing out $\hat{n}$ in terms of Cartesian components,

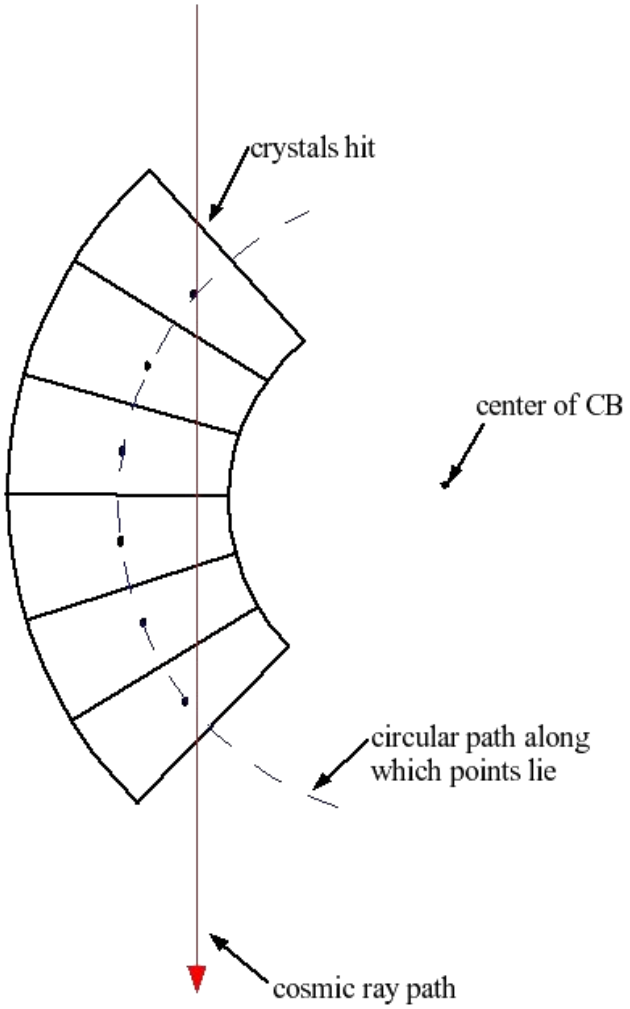

Figure C.1: Hypothetical example of a cosmic ray event

$$\hat{n} = a\hat{i} + b\hat{j} + c\hat{k} \tag{C.2}$$

$$a^2 + b^2 + c^2 = 1 \tag{C.3}$$

allows the sum of the squares of the distances, D^2, for M points to be written as:

$$D^2 = \sum_{j=1}^{M} d_j^2 = \sum_{j=1}^{M} (ax_{1j} + bx_{2j} + cx_{3j})^2 \tag{C.4}$$

To minimize this with respect to the components of $\hat{n}$, the partial derivative of D^2 is taken with respect to a, b, and c, the results are set equal to zero. This results in three equations with three unknowns that can be written in matrix form:

$$Av = 0 \tag{C.5}$$

where the components of A and v are given by;

$$A_{ik} = \sum_{j=1}^{M} x_{ij} x_{kj} \tag{C.6}$$

$$v = \begin{bmatrix} a \\ b \\ c \end{bmatrix} \tag{C.7}$$

The eigenvector associated with the minimum eigenvalue of A is the normal vector of the plane which minimizes D^2. The value of D^2 divided by the number of photons for different numbers of photons striking the CB can be seen in Figure C.2. These

plots look slightly different for different experimental run periods. A large portion of the cosmic events can be removed by cutting out events that occur in the large peak on the left side the plots in Figure C.2.

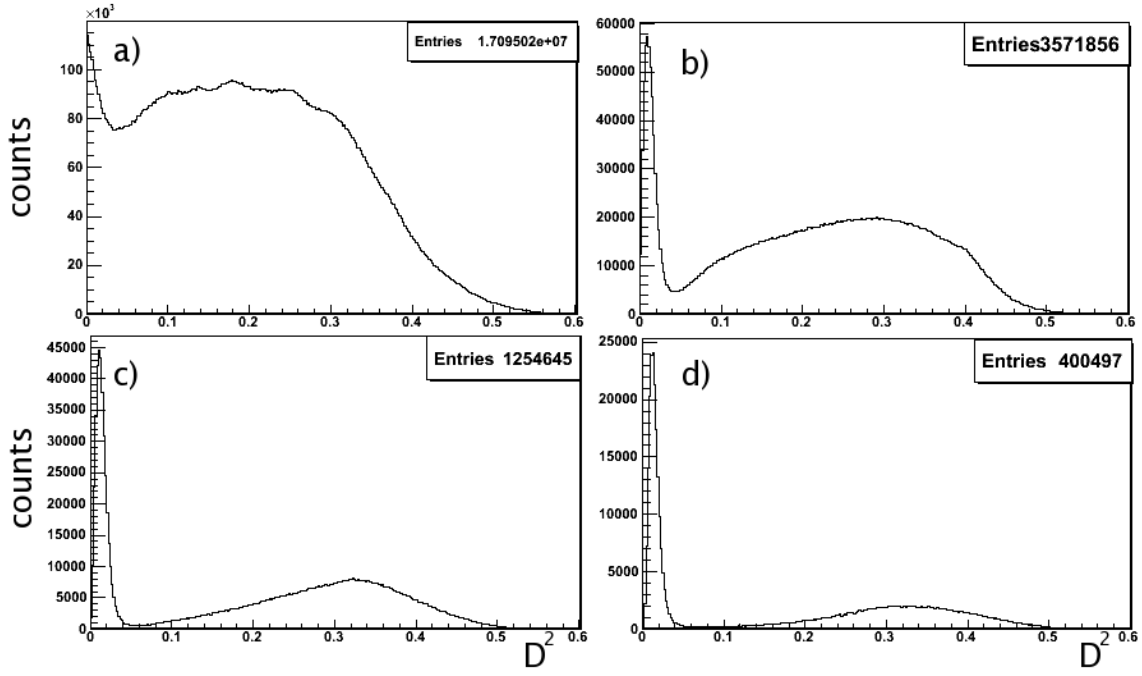

Figure C.2: The value of the D^2 parameter for a November 2004 eta run. a) 3 particles in the CB, b) 4 particles in the CB, c) 5 particles in the CB, d) 6 particles in the CB.

Appendix D

$\eta \rightarrow 3\pi^0$ Monte Carlo

Monte Carlo simulations of $\gamma p \rightarrow \eta p \rightarrow 3\pi^0 p$ were constructed using beam information from the data, and the angular distribution of the η was also taken from the data. Simulation of $\eta \rightarrow 3\pi^0$ was then made according to phase space.

Of the 10 Million simulated $\eta p \rightarrow 3\pi^0 p$ events, 1.6 Million, or 16%, passed the kinematic fit test of $\gamma p \rightarrow \eta p \rightarrow 3\pi^0 p$ at the 2% confidence level (CL). Correcting the 248 thousand detected $\eta p \rightarrow 3\pi^0 p$ events for empty target and acceptance, the original number of $\eta \rightarrow 3\pi^0$ events was 1.5 Million for the November 2004 data set. Using the PDG value for the branching ratio, 0.3251 ± 0.0029 [18], the overall number of η mesons was 4.7 Million. This number was then used in calculating expected numbers of $\eta \rightarrow 3\pi^0$ and $\eta \rightarrow \gamma\gamma$ events in Chapter 4.

Figure D.1.a illustrates the agreement between data and Monte Carlo for the $3\pi^0$ invariant mass, for events which passed the $\gamma p \rightarrow \eta p \rightarrow 3\pi^0 p$ kinematic fit test at the 2% CL, but with the η mass restriction omitted to make this plot. For the same process, Figures D.1.b-e. show the χ^2 probability distribution, the z vertex of the

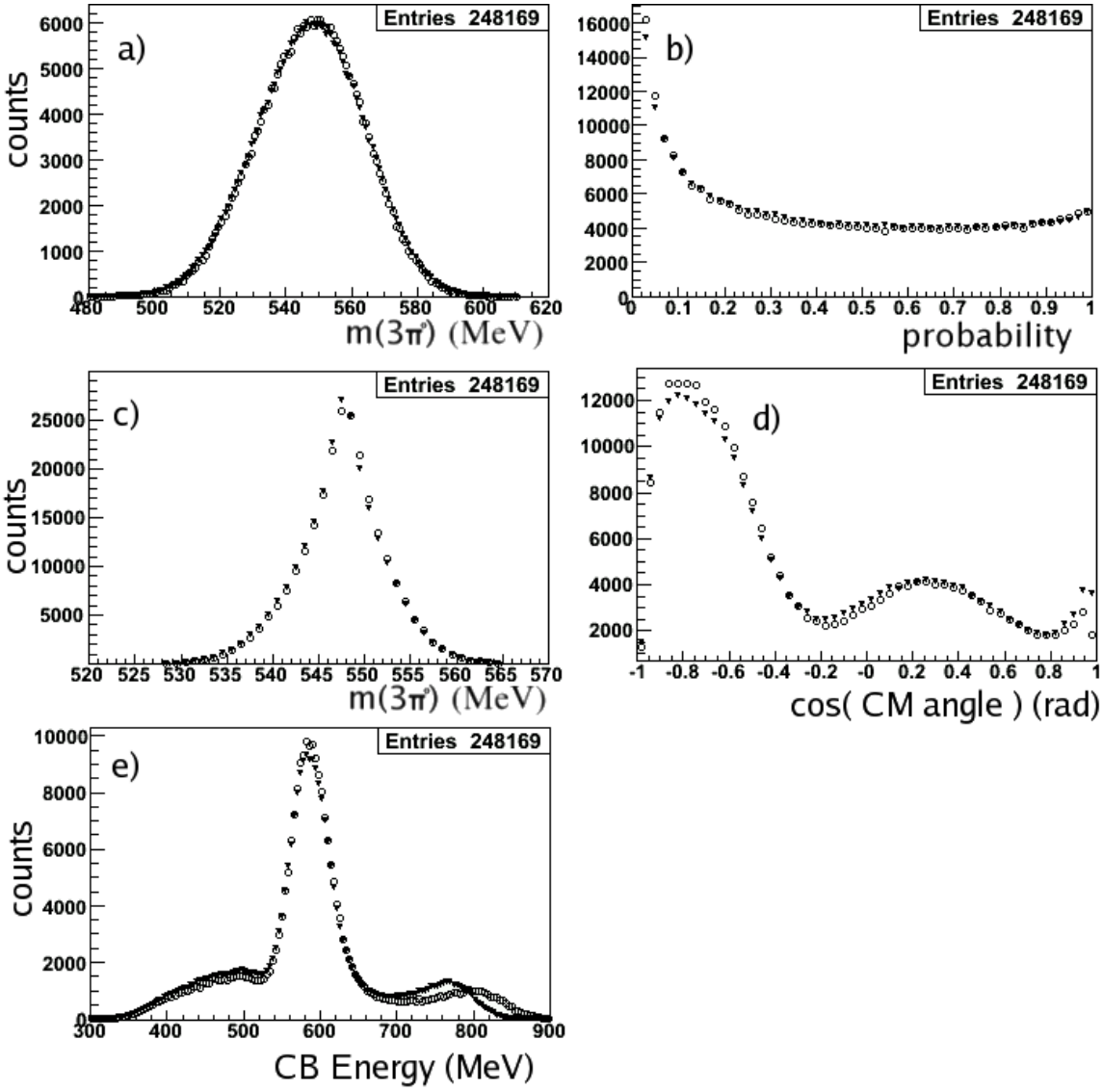

Figure D.1: Comparisons of data (circles) and Monte Carlo Simulations (triangles) for seven cluster events passing the $\gamma p \rightarrow \eta p \rightarrow 3\pi^0 p$ kinematic fit test at the 2% CL. a) The $3\pi^0$ invariant mass (without the η or π^0 mass restrictions); b) the χ^2 probability; c) The $3\pi^0$ invariant mass (without the η mass restriction, but with the π^0 mass restrictions); d) the center of mass angular distribution of the η meson, and e) the CB energy threshold.

interaction point, the polar angle distribution, and the CB energy threshold.

Figure D.2 shows different types of Dalitz plots for both data and Monte Carlo for the same 7 cluster events. Figures D.2.a-b are Dalitz plots that are constructed by plotting the square of the invariant mass of different possible pairs of pions versus one another, for example $m^2(\pi_1^0 + \pi_2^0)$ vs. $m^2(\pi_1^0 + \pi_3^0)$), and all such combinations. Figure D.3.a-b show, in the rest frame of the η meson, the difference in kinetic energy between two of the pions versus the difference between average kinetic energy and the kinetic energy of the third pion, for example $(T(\pi_1^0) - T(\pi_2^0))$ vs. $(T_{avg}(\pi^0) - T(\pi_3^0))$, and all such combinations.

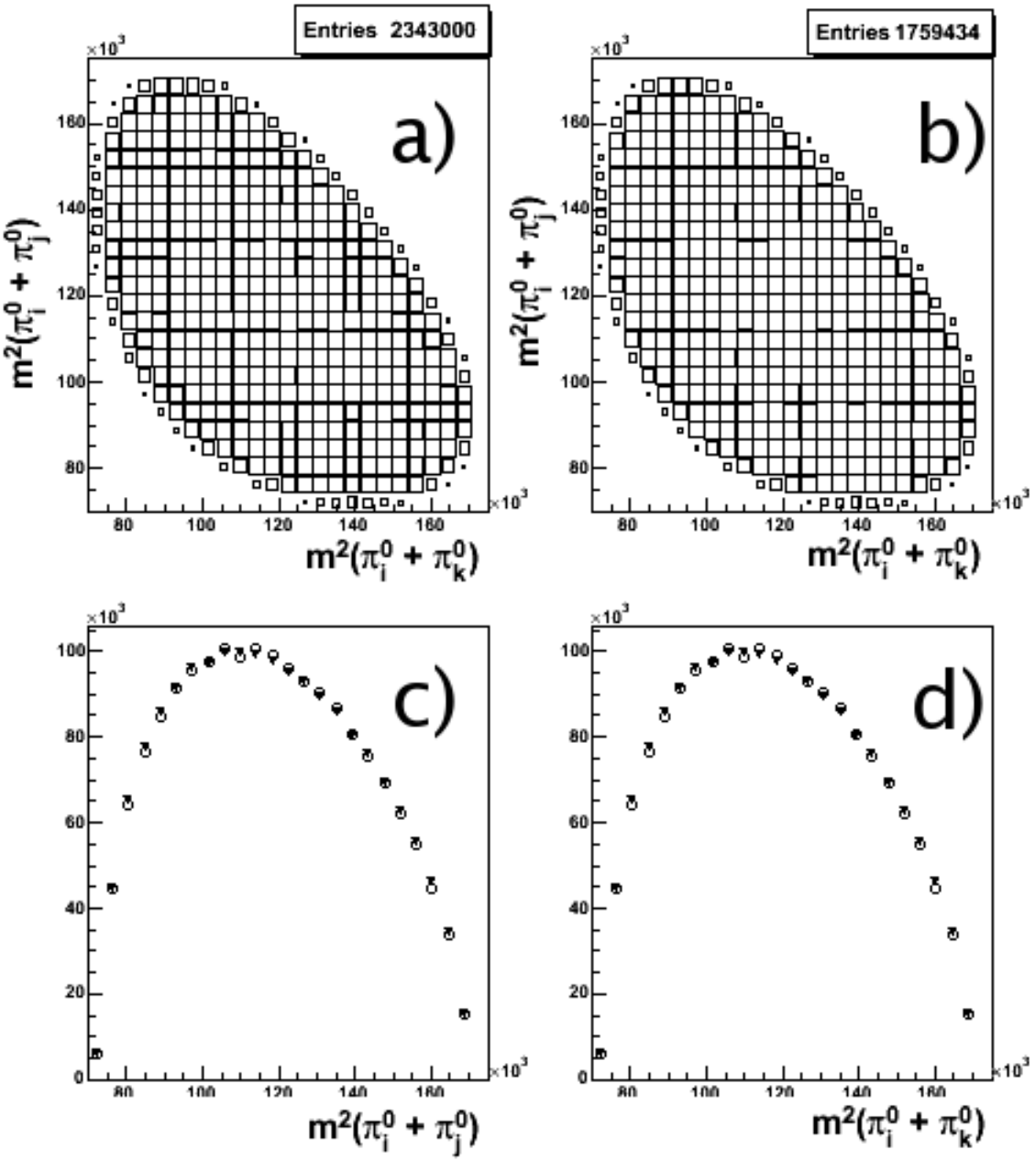

Figure D.2: Standard Dalitz density plots of events which passed the $\gamma p \to \eta p \to 3\pi^0 p$ kinematic fit test at the 2% CL relating to the squares of pairs of pions are shown for a) data and b) Monte Carlo. Projections along the c) x-axis and d) y-axis, with Monte Carlo designated by triangles and raw data by open circles.

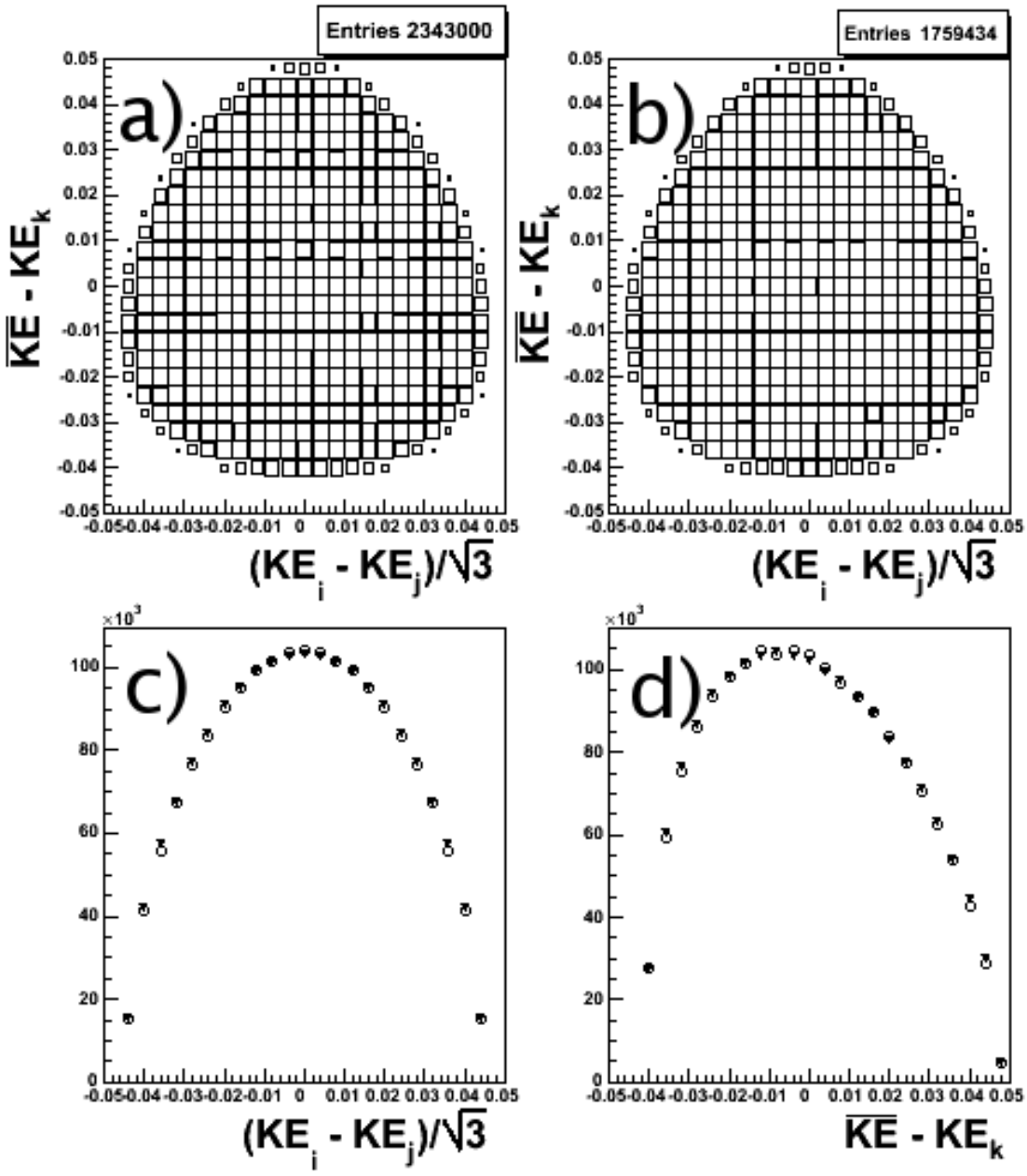

Figure D.3: Symmetrized Dalitz density plots of events which passed the $\gamma p \to \eta p \to 3\pi^0 p$ kinematic fit test at the 2% CL relating to the kinetic energies of pions are shown for c) data and d) Monte Carlo. Projections along the c) x-axis and d) y-axis, with Monte Carlo designated by triangles and raw data by open circles.

Appendix E

Slope Parameter α of $\eta \rightarrow 3\pi^0$

The α parameter of the $\eta \rightarrow 3\pi^0$ decay describes the difference between the the actual decay and that expected from pure phase space. This difference is due to the energy dependence of the $\pi\pi$ interaction. The most recent experimental determinations is -0.031 ± 0.004 by [26].

The α parameter is related to the square of the transition amplitude, M, which may be parametrized as

$$|M|^2 \propto 1 + 2\alpha Z \tag{E.1}$$

where

$$Z = \frac{6}{(m_\eta - 3m_{\pi^0})^2} \Sigma_{i=1}^{3} \left(E_{\pi^0}^i - m_\eta/3\right)^2 \tag{E.2}$$

and E_i is the energy of pion i in the η rest frame.

Figure D.3(a) shows a Dalitz plot of $3\pi^0$ events recorded. Figure E.1(b) displays the ratio of the Z determined from the November 2004 data and one which was determined from Monte Carlo simulations. From this plot, a determination of α has

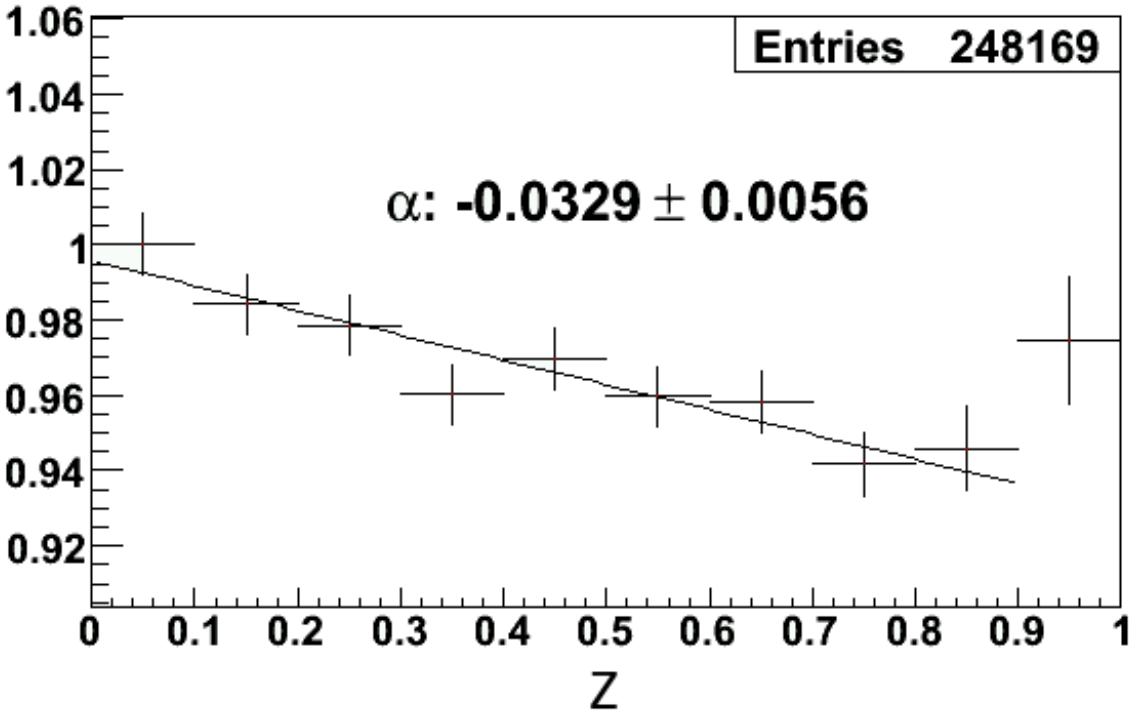

Figure E.1: The ratio of the MC and data values of Z, from which α is determined.

been made of

$$\alpha = -0.033 \pm 0.006 \tag{E.3}$$

The number of data events used was approximately 248 thousand, all from 7 cluster events with the proton detected, which passed kinematic fit tests of $\gamma p \to \eta p \to 3\pi^0 p$ with a probability greater than 2%. The number of Monte Carlo events used was 10 million, they were detected with an efficiency of 16%.

Appendix F

Multiwire Proportional Chambers (MPC)

Two Multiwire Proportional Chambers (MPC), based on a design used with the DAPHNE [1] detector, surround the PID. They were used for measuring the trajectories of charged particles. The azimuthal angle ϕ is measured with 480 radially arranged anode wires, and the polar angle θ is measured using the intersection points of 320 helically wound cathode strips. The angular resolution in ϕ is $\sigma_\phi \sim 2\ ^\circ$, and for θ it is $\sigma_\theta \sim 1^\circ$.

[1] DAPHNE: Détecteur à grande Acceptance pour la PHysique Nucléaire Expérimentale

Appendix G

Electromagnetic Cascades

When a high energy photon is incident upon a thick absorber, the main means of energy loss is through electron-positron pair production. Energy loss due to the photoelectric effect and Compton scattering is also present, but negligible for energies above a few 10 MeV. The electrons and positrons then go on to generate more photons through Bremsstrahlung, and the process repeats, creating an electromagnetic cascade (EMC), or shower. Electron energies eventually fall to the level where the dominant form of energy loss is through ionization and excitation and the shower dissipates.

The longitudinal development of an EMC can be reasonably well described for an incident photon of energy E_0 by an energy loss per unit length [18]

$$\frac{dE}{dt} = E_o b \frac{(bt)^{a-1} e^{-bt}}{\Gamma(a)}. \tag{G.1}$$

The unit of length here, t, the unit of the radiation length, X_0, of the material. The point at which the maximum energy deposit occurs is related to the coefficients a and

b in G.1 by

$$t_{max} = (a-1)/b = 1.0 \times \left(\ln \frac{E}{E_c} + 0.5 \right) \tag{G.2}$$

where E_c is defined as the energy loss per X_0 for a high energy electron. For the CB, an equivalent equation to G.2 is used as the point of interaction in a crystal when calculating photon angles with respect to the target. For a typical photon energy around 200 MeV, t_{max} is approximately 3 radiation lengths, 90% of an EMC's distribution is deposited within approximately 11 radiation lengths, well within the 15.7 radiation lengths of a CB crystal. For TAPS, the situation is quite similar, with t_{max} and the 90 % containment of the ECM energy almost the same as the CB.

The lateral development of a shower is often parametrized by the Moliere radius, R_M, which is related to X_o

$$R_M = X_0 \frac{E_s}{E_c} \tag{G.3}$$

where E_s is the scale energy, which has a value of 21 MeV. R_M signifies the radius of a cylindrical volume of infinite length in which ~90% of the incident energy is contained. For NaI, $R_M = 4.13$ cm, so the choice of 13 crystals used in the CB clusters is adequate to contain the majority of the energy (see section 2.4). For the BaF2 crystals in TAPS, $R_M = 3.10$ cm, so the 7 crystal cluster also adequately contains the photon ECMs. See sections 2.4 and 2.5 for crystal dimensions.

Bibliography

[1] Ll. Ametller, J. Bijnens, A. Bramon and F. Cornet, Phys. Lett. B 276, 185 (1992).

[2] M.N. Achasov et al., Nucl. Phys. B 600, 3 (2001).

[3] G. Di Giugno et al., Phys. Rev. Lett. 16, 767 (1966).

[4] M.A. Wahlig, E. Shibata and I. Mannelli, Phys. Rev. Lett. 17, 221 (1966).

[5] F. Binon et al., Yad. Fiz. 33, 1543 (1982) also Lett. Nuovo Cim. A 71, 497 (1982).

[6] D. Alde et al. (GAMS-2000 Collaboration), Yad. Fiz. 40, 1447 (1984) also Z. Phys. C 25, 225 (1984).

[7] S. Okubo and B. Sakita, Phys. Rev. Lett. 11, 50 (1963).

[8] G. Oppo and S. Oneda, Phys. Rev. 160, 1397 (1967).

[9] G.J. Gounaris, Phys. Rev. D 2, 2734 (1970).

[10] P. Ko, Phys. Rev. D 47, 3993 (1993).

[11] S. Bellucci and C. Bruno, Nucl. Phys. B 452, 626 (1995).

[12] J. Bijnens, A. Fayyazuddin and J. Prades, Phys. Lett. B 379, 209 (1996).

[13] J.N. Ng and D.J. Peters, Phys. Rev. D 46, 5034 (1992).

[14] J.N. Ng and D.J. Peters, Phys. Rev. D 47, 4939 (1993).

[15] M. Jetter, Nucl. Phys. B 459, 283 (1996).

[16] E. Oset, J.R. Pelaez and L. Roca, Phys. Rev. D 67, 073013 (2003).

[17] S. Prakhov et al. Phys. Rev. C 72, 025201 (2005)

[18] W.-M.Yao et al., (Particle Data Group), J. Phys. G 33, 1 (2006).

[19] S.J. Hall et al., Nucl. Instr. and Meth. in Phys. Res. A 368, 698 (1996)

[20] B. Boillat, University of Basel, Switzerland, private communication.

[21] R. Codling, University of Glasgow, Scotland, private communication.

[22] V. Kashevarov, Johannes Gutenberg Universität Mainz, private communication.

[23] P. Drexler et al., IEEE Trans. Nucl. Sci. 50-4, 969 (2003)

[24] Documents and source code available at http://www.desy.de/~blobel

[25] J. Alber i Fort, *Test Measurements for the Crystal Ball Detector at MAMI*, Diploma Thesis, Institute für Kernphysik, Johannes Gutenberg Universität Mainz, 2003.

[26] W. B. Tippens et al., Phys. Rev. Lett. 87, 192001 (2001)